AN INVESTIGATION OF RADIATION DOSE TO PATIENT'S EYE LENS AND SKIN DURING NEURO- INTERVENTIONAL RADIOLOGY PROCEDURES

MOHAMMAD JAVAD SAFARI

THESIS SUBMITTED IN FULFILMENT OF THE REQUIREMENTS FOR THE DEGREE OF DOCTOR OF PHILOSOPHY

FACULTY OF MEDICINE
UNIVERSITY OF MALAYA
KUALA LUMPUR

2016

UNIVERSITY OF MALAYA

ORIGINAL LITERARY WORK DECLARATION

Name of Candidate: Mohammad Javad Safari

Registration/Matric No: MHA120058

Name of Degree: Doctor of Philosophy

Title of Thesis ("An Investigation of Radiation Dose to Patient's Eye Lens and Skin During Neuro- Interventional Radiology Procedures"):

Field of Study: Medical Physics

I do solemnly and sincerely declare that:

(1) I am the sole author/writer of this Work;
(2) This Work is original;
(3) Any use of any work in which copyright exists was done by way of fair dealing and for permitted purposes and any excerpt or extract from, or reference to or reproduction of any copyright work has been disclosed expressly and sufficiently and the title of the Work and its authorship have been acknowledged in this Work;
(4) I do not have any actual knowledge nor do I ought reasonably to know that the making of this work constitutes an infringement of any copyright work;
(5) I hereby assign all and every rights in the copyright to this Work to the University of Malaya ("UM"), who henceforth shall be owner of the copyright in this Work and that any reproduction or use in any form or by any means whatsoever is prohibited without the written consent of UM having been first had and obtained;
(6) I am fully aware that if in the course of making this Work I have infringed any copyright whether intentionally or otherwise, I may be subject to legal action or any other action as may be determined by UM.

Candidate's Signature Date:

Subscribed and solemnly declared before,

Witness's Signature Date:

Name:
Designation:

ABSTRACT

X-ray guided interventional procedure is a common diagnostic and/or treatment modality for various vascular and cardiac diseases. Advanced technology has enabled interventional radiologists in performing more complex neuro-radiology procedures, resulting in concomitant increase in radiation dose to the patients.

The main contributions of this thesis were firstly, characterisation of the MO*Skin* detector in kilovoltage photon beams and testing its suitability for *in-vivo* patient's dose measurements during interventional radiology procedures. Secondly, a comprehensive evaluation of the exposure parameters contributions on patient's dose during neuro-interventional procedures was performed. It was found that the lateral x-ray tube contributed considerably high radiation dose to patient's eye lens. This led to the design and fabrication of a novel type of eye lens protector for those procedures that patient's eye is repeatedly positioned within the lateral tube exposure field, where the applying of collimation on lateral beam is not possible. The eye lens protector was designed to be placed within the x-ray field of view, attenuating the direct beam from the lateral x-ray tube while being sufficiently radiolucent not to perturb the radiological image and the interventional procedure.

Finally, a new type of an anthropomorphic head phantom was fabricated with more options for dosimeter placement and more similar tissue substitute materials to actual human eye, in order to evaluate the dose delivered to the patient's eye lens during a clinical neuro-interventional procedure.

The MO*Skin* detector has been proven to be a reliable and suitable dosimetry system for the measurement of the radiation dose in kilovoltage photon beams and has been successfully utilised during 35 clinical neuro-interventional procedures to evaluate the radiation dose received by the patients' eye lenses. This study revealed that among the 35 patients, the left outer canthus regions of 8 patients and left eyelid region of one

patient were found to receive higher dose than the recommended threshold dose for cataract formation (500 mGy).

Based on the study of the contribution of exposure parameters on patient's dose, it is recommended that the judicial use of acquisition imaging techniques and the use of the lateral x-ray tube particularly in the anterior-oblique orientation, in order to reduce the patient's eye lens dose during neuro-interventional procedures. In the situation where the application of physical collimation on lateral tube beam is not possible, the novel eye protector layer may be used to attenuate the direct radiation beam to the patient's eye lens.

This work showed that for a simulated aneurysm procedure this protector reduced the maximum radiation dose received by the eye lens and eyelid up to 62.1% and 23.3%, respectively. The eye protector also had negligible effects on the exposure parameters (by a maximum of 8% for the tube current-time product of the DSA (2 frame per second) imaging mode) and image quality (increases the fluoroscopy image pixel value up to 4.7% ± 0.6%). Lastly, the fabricated anthropomorphic phantom has been proved to be a suitable tissue-mimicking medium for the evaluation of the radiation dose received by the patient's eye lens during clinical diagnostic procedures.

ABSTRAK

Prosedur intervensi berpandukan sinar-x merupakan salah satu modaliti diagnostik dan/atau rawatan yang lazimnya digunakan untuk merawat penyakit vascular dan jantung. Kecanggihan teknologi telah membolehkan pakar radiologi intervensi menjalankan prosedur neuro-radiologi yang lebih kompleks, justeru menyebabkan peningkatan dalam dos sinaran kepada pesakit.

Sumbangan utama tesis ini adalah, yang pertama, pencirian pengesan MO*Skin* dalam alur foton kilovotage dan menguji kesesuaiannaya dalam pengukuran dos *in-vivo* pesakit semasa prosedur intervensi radiologi. Kedua, penilaian komprehensif mengenai sumbangan parameter dedahan terhadap dosimetri pesakit. Penyelidikan ini mendapati bahawa tiub x-ray lateral memberikan dos sinaran yang cukup tinggi kepada kanta mata pesakit. Pemerhatian ini membawa kepada reka bentuk dan fabrikasi sejenis model pelindung kanta mata bagi prosedur-prosedur yang melibatkan mata pesakit yang sentiasa berada pada kedudukan ruang pendedahan tiub lateral, dimana kolimasi tidak boleh dilakukan. Pelindung kanta mata telah direka bentuk/cipta untuk diletak dalam pandangan ruangan sinar-x, lantaran mengurangkan pancaran terus daripada tiub sinaran-x lateral dan dalam masa yang sama tidak mengubah imej radiologikal dan prosedur intervensi. Akhir sekali, sejenis fantom kepala telah dihasilkan dengan lebih banyak pilihan untuk meletakkan dosimeter dan dengan menggunakan bahan penggantian tisu yang lebih hampir sama dengan mata manusia yang sebenar, bagi menilai penerimaan dos radiasi kepada kanta mata pesakit semasa prosedur intervensi-neuro klinikal. Pengesan MO*Skin* telah terbukti dipercayai dan merupakan sistem dosimeter yang sesuai untuk pengukuran dos radiasi dalam alur foton kilovoltage dan system ini telah berjaya digunakan untuk 35 prosedur intervensi-neuro klinikal untuk menilai dos radiasi yang diterima oleh kanta mata pesakit.

Kajian ini membuktikan bahawa, di antara 35 pesakit, bahagian luar kiri canthus untuk 8 pesakit dan bahagian kiri kelopak mata seorang pesakit didapati menerima dos yang tinggi berbanding dos yang disyorkan untuk penghasilan katarak (500 mGy). Berdasarkan kajian sumbanagan parameter dedahan terhadap pesakit, adalah disarankan penggunaan teknik pengimejan yang betul dan tiub sinar-x lateral terutamanya pada orientasi anterior-oblique digunakan untuk mengurangkan dos kanta mata pesakit semasa prosedur intervensi-neuro. Dalam situasi dimana aplikasi kolimasi fizikal tidak dapat dilaksanakan, lapisan pelindung mata mungkin boleh mengurangkan sinaran terus kepada kanta mata pesakit.

Kajian ini menunjukkan untuk prosedur aneurysm, pelindung ini berjaya mengurangkan dos radiasi maksimum yang diterima oleh kanta dan kelopak mata sebanyak 58.2% dan 23.3% masing-masing. Pelindung mata tersebut juga mempunyai kesan yang minima terhadap parameter dedahan (maksimum 8% untuk produk arus-masa mod pengimejan DSA (2 frame per saat)) dan kualiti imej (penigkatan pixel imej fluoroskopi sebanyak 4.7% ± 0.6%). Akhir sekali, penghasilan fantom antropormofik telah terbukti menjadi medium untuk penilaian dos radiologi yang diterima oleh kanta mata pesakit semasa prosedur klinikal diagnostik.

ACKNOWLEDGMENTS

First and foremost, I would like to express my sincere gratitude to my supervisor Prof. Dr. Ng Kwan Hoong for his dedication and his invaluable experience. I greatly appreciate for his guidance and contributions over the course of my research and his passion to teach younger researcher how to be creative and self-disciplined. It has been an honour and a privilege to be his Ph.D. student.

I would like to thank my supervisor Dr. Jeannie Hsiu Ding Wong for her kindness, patience, as well as her research experience. During the course of this study, she have always supported and encouraged me and I greatly appreciate all her advice and guidance from the initial to the final stages of my study. She was always willing to discuss about my research when I needed. She allocated her time to discuss with me when I faced any difficulties in my research and sometimes our discussion dragged on several hours, but she had same enthusiasm as me to continue and find a solution.

I am thankful to Prof. Anatoly Rosenfeld for his constructive comments and suggestions about MO*Skin* dosimtery system, which lead this project to be in a right direction and I appreciate his help for his valuable evaluation and proofreading of my publications.

I would also like to thank Associate Professor Khairul Azmi Bin Abd Kadir, who supported me in the clinical aspect and allowed me to collect patients' radiation doses during his interventional neuro-radiology procedures.

I am thankful to all my friends in the Medical Physics group, Susie Lau, Jong Wei Loong, Sogol Givehchi, Fione Tan, Nurul Hashikin, and Norhasnah Zakariyah, whom

we shared a laboratory and they provided a pleasant and friendly environment. Their discussion and advices helped me to look at my research from different prospective. We spend so much time together and traveled to different places, which made up of wonderful memories for me.

I would like to thank the personnel at the following institutions for their support in this study: Muhammad Isa and Norhayati Abdullah at the Medical Physics group of Malaysian Nuclear Agency, Dr. Ung Ngie Min at the Clinical Oncology Unit, University of Malaya, Chin Chew Lee and Muhammad Mozaker, radiographers at the UMMC, and Lam Kim Hong at Philips Healthcare Malaysia and Medical Physics Unit (UMMC) for the loan of equipment for this research.

Finally, I thank my parents and my brother and sisters, for their love, support and encouragement through my life. Living in Malaysia has kept me away from them for many years, but they have always supported me. This thesis is dedicated to my lovely family.

TABLE OF CONTENTS

LIST OF FIGURES

LIST OF TABLES

LIST OF SYMBOLS AND ABBREVIATIONS

ADRC	:	Automatic dose rate control
AEC	:	Automatic exposure control
AK	:	Air-kerma
AK_F	:	Frontal tube air-kerma
AK_L	:	Lateral tube air-kerma
AVM	:	Arteriovenous malformation
CD	:	Computed tomography
DNA	:	Deoxyribonucleic acid
DICOM	:	Digital imaging and communication in medicine
DSA	:	Digital subtraction angiography
EDS	:	Energy dispersive x-ray spectroscopy
ESD	:	Entrance skin dose
FD	:	Field dimension
FT	:	Fluoroscopic time
HVL	:	Half value layer
ICRU	:	International Commission on Radiation Units & Measurements
ICRP	:	International Commission on Radiological Protection
IOD	:	Image to object distance
IRP	:	Interventional reference point
KAP	:	Kerma-area-product
LAO	:	Left anterior oblique
LE	:	Left eyelid
LET	:	Linear energy transfer
LOC	:	Left outer canthus
MOSFET	:	Metal oxide semiconductor field effect transistor

MSD	:	Maximum skin dose
PDD	:	Percentage-depth-dose
PTCA	:	Percutaneous transluminal coronary angioplasty
RAO	:	Right anterior oblique
RNA	:	Ribonucleic acid
RPLD	:	Radiophotoluminescence glass dosimeter
SEM	:	Scanning electron microscope
SID	:	Source image distance
SSD	:	Source skin distance
TLD	:	Thermoluminescence dosimeter
WED	:	Water equivalent depth

LIST OF APPENDICES

CHAPTER 1: GENERAL INTRODUCTION

1.1. Introduction

In recent years, x-ray guided interventional radiological (IR) procedures have become an integral part of vascular and cardiac treatments and the number of these examinations is increasing every year (Valentin, 2000; UNSCEAR, 2010). Advancement in imaging technology and new catheters and guide wire designs has enabled interventional radiologists in performing more complex neuro-radiological procedures, which inadvertently results in longer exposure time and higher radiation dose to patients. Notwithstanding the fact that neuro-interventional procedures have a high rate of success in vascular treatments, long radiation exposure during complicated interventional radiology procedures still remains a concern.

The variability in patient's irradiation dose is the result of different factors, such as the complexity of the procedure, the experience of the interventional radiologists, and their awareness about patient's radiation safety. Complex and repeated interventional procedures may increase the risk of tissue reaction effects like radiation-induced skin injuries (Wagner *et al*., 1999; Mooney *et al*., 2000; Wolff, *et al*., 2001) and cataract formation (Berthelsen & Cederblad, 1991; Meriçı *et al*., 1998; Wagner & Archer, 1998). The threshold dose for cataract formation during acute radiation exposure has recently been reduced based on recent epidemiology findings (Worgul *et al*., 2007; Chodick *et al*., 2008; Vano *et al*., 2010; Mrena *et al*., 2011) to 0.5 Gy, recommended by the International Commission on Radiological Protection (ICRP) in 2011 (Stewart *et al*., 2012). This threshold dose is about four-times smaller than the threshold dose of early skin reactions (skin erythema) of 2 Gy (Wagner, 1998).

So far different indirect dose metric parameters have been established to evaluate patient's skin dose during interventional procedures (IEC, 2000; Balter *et al*., 2002;

FDA, 2009). While these parameters are mostly recorded after each interventional radiology procedure and can be presented as an estimate of the radiation dose received by patient, they do not provide any information about the location of the skin dose and radiation dose received by other organs. These parameters may sometimes provide unrealistic estimation of patient's skin dose during an individual procedure (Vano *et al*., 2001; Fletcher *et al*., 2002; Miller *et al*., 2003; Balter, 2006; Jaco & Miller, 2010). During interventional radiology procedures, the patient's body is irradiated with a non-uniform exposure, causing non-homogeneous dose distribution throughout the patient's body. This indicates the importance of *in-vivo* radiation dose measurement of the radiosensitive organs like eye lens during a clinical procedure.

1.2. Statement of Research Problems

The literature on previously research indicates that although the importance of the patient's radiation safety during prolonged interventional procedures have been stressed, only limited studies have directly measured the radiation dose received by the patients' eyes during neuro-interventional procedures. So far, these evaluations have been conducted only for research purposes without any direct impact on patient's radiation dose safety during clinical neuro-interventional procedures. Currently, there is no real-time *in-vivo* dosimetry system that has been used for patient's dose monitoring during interventional radiology procedures. A real-time dose-monitoring system can provide real-time information for each particular exposure, which can be used to optimise patient's radiation safety during interventional radiology procedures.

In addition, while the impact of the exposure parameters, such as exposure direction, exposure type (fluoroscopy, acquisition, etc.), field dimension, frame rate, distance between image receptor to patient's body, and beam-on duration, on patient's dose have been repetitively highlighted by the various organisations (Valentin, 2000; IAEA,

2010), their contribution to the radiation dose received by patients have not been quantitatively evaluated, much less with respect to patient's eye lens dose.

These concerns emphasize the problems of patient's eye dose during complex neuro-interventional procedures and the lack of knowledge about the contribution of exposure parameters on patient's dose is outlined as follows:

I. Although a large number of radiation safety studies can be found regarding to the concern of occupational eye lens dose during interventional radiology procedures in the current literature, there is little data published concerning on level of the radiation dose received by the patient's eye lens.

II. The current *in-vivo* dose monitoring systems are used as post-processing dose evaluation methods and do not provide any real-time feedback for interventional radiologists and consequently do not have any direct impact on patient's radiation dose safety during a clinical interventional procedure.

III. As it is well known, operators play an important role in controlling the patient's dose level during interventional radiology procedures. Operators' knowledge of the effects of exposure parameters on patient's dose is a key factor for improving patient's radiation safety. While there are several studies evaluating the effect of the exposure parameters on patient's skin dose, the contributions of exposure parameters on patient's eye lens dose have not been quantitatively evaluated yet.

IV. Patient's eye lens dose is highly subjected to the radiation collimation. With proper collimation of the lateral radiation field, the patient's eye lens dose is dramatically reduced. To date, where collimation of the radiation field is not possible, there is no alternative method or technique to reduce the patient's eye lens dose during a clinical procedure.

V. Anthropomorphic phantoms can be used to evaluate the actual radiation dose received by the patient's eye lens. Commercial anthropomorphic phantoms that

are available currently mainly mimic the human eyeball as a homogenous organ with the same tissue substitute of soft tissues, which cannot precisely represent the actual human eye. This may cause inaccuracies in the radiation dose measured in order to determine the dose to the patient's eye lens.

1.3. Research Objectives

The aim of this research is to investigate the radiation dose received by the patient's eye lens and skin during neuro-interventional radiology procedures. The primary focus is the eye lens. This work considers the characterisation and application of a relatively new real-time dose monitoring system in order to evaluate the patient's dose during clinical procedures. This thesis does not address the radiation dose received by other radiosensitive organs of the patient during clinical neuro-intervention procedures, nor the patient's dose received during other intervention procedures.

The series of research objectives of this thesis are listed as follows:

1. To investigate the radiation properties and characteristics of the MO*Skin* detector under kilovoltage (kV) photon beams
2. To examine the application of the MO*Skin* dosimetry system in order to monitor the patient's eye lens dose during clinical neuro-interventional procedures
3. To investigate the correlation of patient's eye lens dose with dose metric parameters (like fluoroscopy time, kerma-area product (KAP), and air-kerma (AK)) during neuro-interventional procedures
4. To explore the contribution of the exposure parameters on radiation dose received by the patient's skin and eye lens
    4.1. To survey on frequently used exposure parameters during neuro-interventional procedures
    4.2. To analyse the exposure parameters contribution on patient's eye lens and skin dose based on a phantom study

5. To design and fabricate a radiation protector layer in order to reduce the radiation dose received by patient's eye lens during neuro-interventional procedures
6. To design and fabricate a new anthropomorphic head phantom to facilitate better measurement of eye lens dose

1.4. Thesis Organisation

Chapter 2 describes briefly about the skin and eye lens radiation reactions and some necessary radiobiological background. This followed by general information on fluoroscopy guided interventional procedure, and various dose metric methods (direct and indirect dose metrics). Various dosimetry systems used during interventional procedures such as the radiochromic film, thermoluminescent dosimeter (TLD), radiophotoluminescence glass dosimeter (PLD), metal-oxide semiconductor field effect transistor (MOSFET) are also outlined in this chapter. The last section of this chapter explains about the MOSFET dosimeter design and provides an overview of this detector and its principal of operation.

Chapter 3 outlines the different equipment and systems, which are used in this research, such as the MO*Skin* detector, Gafchromic® XR-RV3 film, anthropomorphic and Solid Water® phantoms, Philips Allura Xper FD20/20® biplane and its automatic dose rate control system (ADRC), energy dispersive x-ray spectroscopy (EDS), XCOM software, and 3-dimensional (3D) printing.

Chapter 4 discusses research objective 1 to present the radiation properties and characterisation of MO*Skin* dosimeter when irradiated with kV photon beams. The MO*Skin* detector responses in terms of changing radiation energy, field size, exposure angle, source to surface distance (SSD), dose rate, and percent depth dose (PDD) are investigated individually.

Chapter 5 presents the application of the MO*Skin* dosimeter in the measurement of

patient's eye lens dose during neuro-interventional radiology procedures. This chapter elaborates research objectives 2 and 3. The radiation doses received at patients' left eyelids and left outer canthus are measured for 35 neuro-interventional procedures. The correlations of the measured doses with exposure parameters, such as fluoroscopy time (FT), total kerma-area product (KAP), and air-kerma (AK) of the frontal (AK_F) and the lateral tubes (AK_L) are made.

Chapter 6 includes two aspects: the first, a survey of the exposure parameters commonly used during clinical neuro-interventional procedures (58 randomly selected procedures) and the second, an analysis of the effects of these parameters on patient's entrance skin dose during neuro-interventional procedures. The contribution of various exposure parameters to patient's entrance skin dose is investigated using an adult female anthropomorphic phantom. The radiation dose is measured using the MO*Skin* dosimetry system. The effects of each controllable exposure parameters (exposure time, angle, field dimension, image receptor to patient distance, and frame rate) on the patient's entrance skin dose and eye lens dose are considered individually. The chapter findings attempt to address objective 4 (objectives 4.1 and 4.2).

In Chapter 7 a radiation protector layer is designed and fabricated in order to reduce the patient's eye lens dose during neuro-interventional procedures, specifically when the use of collimation is limited. This chapter considers research objective 5, in order to study the feasibility of using the fabricated eye protector during a clinical procedure in terms of its radiation attenuation properties and its effects on image quality and exposure parameters.

Chapter 8 presents the design and fabrication of an anthropomorphic head phantom, which provides greater options for dosimeter placement with more similar tissue substitute materials to actual organs. The fabricated phantom containing different parts of the human eyeball, which is made by suitable tissue-mimicking mediums providing

greater opportunity to study the radiation dose received by the patient's eye lens during a clinical procedure in compared with commercially available anthropomorphic phantoms. This chapter findings address research objective 6.

Chapter 9 summarises the overall findings from this thesis and future researches on MO*Skin* applications, optimisation of the eye protector design and elemental composition, and extension of the 3-dimensional (3D) printer applications in construction of custom-made anthropomorphic phantoms are proposed in this chapter.

CHAPTER 2: LITERATURE REVIEW

2.1. Structure and Function of the Skin

The human skin comprises of three layers, called epidermis, dermis, and subcutaneous tissue (Figure 2.1). The epidermis contains of three cell types: squamous cells, melanocytes, and basal cells. The Squamous cell layer is the thickest layer of the epidermis makes the outermost epidermis and protects the skin from environmental stresses such as viruses, bacteria, and other foreign substances and protects the internal organs, like nerves, blood vessels, and muscles against trauma. The epidermis is mainly built by the keratinocytes cells originate from cells in the basal layer (Harle-Bachor & Boukamp, 1996). The basal layer is the innermost of the epidermis (depth between 20 μm to 100 μm) where the most cell division takes place and contains cells called melanocytes. The melanocytes cells scatter through the basal layer create the pigment melanin. This layer protects the skin from UV radiation and gives the colour to the skin (D'Orazio *et al*., 2013). Dermis layer is thicker (1.5 to 4 mm thick) in comparing to epidermis (50 μm to 1.5 mm thick with an average thickness of 70 μm), contains the nerve endings, hair follicles, sweat glands, sebaceous glands, lymph vessels, and blood vessels. The dermis gives the skin its strength and flexibility and supplies the nutrients for the epidermis layer. Third layer of the skin is subcutaneous tissue or adipose tissue. This layer serves as an insulator of heat and cold, storage the energy, and protective padding. The basal layer due to its fast proliferation has been considered as a target cell layer for carcinogenesis. The International Commission on Radiological Protection (ICRP) Report 59 stated the importance of evaluation of radiation dose at the level of the basal layer (assumed at a depth of 70 μm) and according to this statement, for precise skin dose measurements, detectors should be calibrated at a depth equal to 70 μm in order to accurately estimate the skin dose and eventually skin cancer risk (ICRP, 1991).

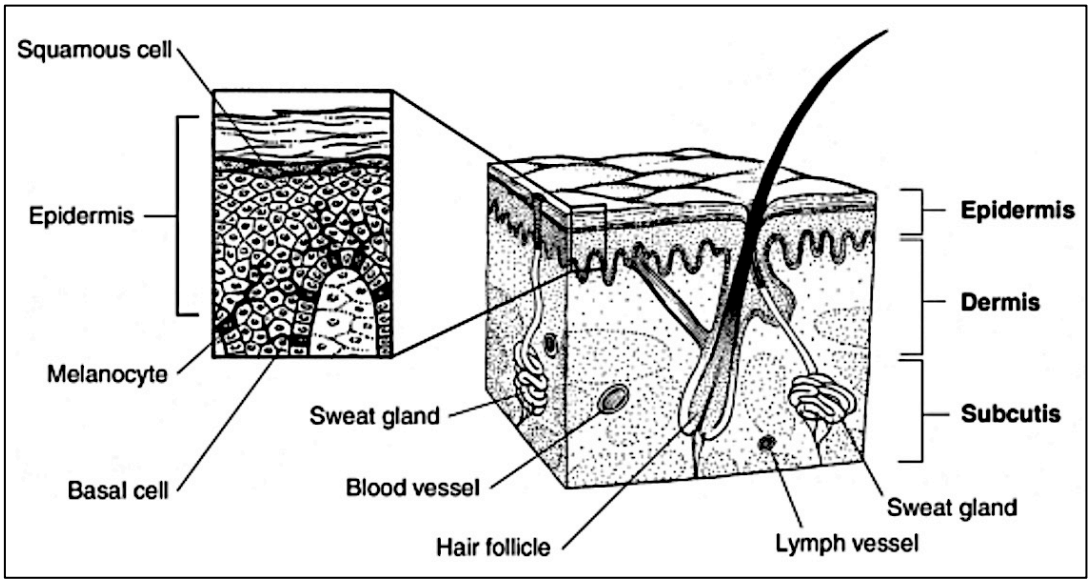

Figure 2.1. Schematic diagram of different layers of the human skin. The epidermis layer contains the squamous cells, melanocytes and basal cells, which can cause squamous cell cancers, melanoma, and basal cell cancer. The dermis layer comprises the sweat glands, blood vessels, hair follicles, and lymph vessels, which is placed between subcutaneous tissue and epidermis (reproduced from (American Cancer Society, 2014)).

2.2. Structure and Function of the Eye

The eye consists of different compartments, such as the cornea, iris, crystalline lens, vitreous humor, retina, and optic nerve (Figure 2.2a). The light enters the eye passes through the cornea (0.50 mm thick) with an index of refraction of 1.377 and then crosses the anterior chamber (3.04 mm thick) with a refractive index of 1.336 (Gross *et al*., 2008). Afterward the light passes through the crystalline lens (3.60 mm thick) with average refractive index of 1.408 (Uhlhorn *et al*., 2008). The lens is a biconvex structure surrounded with anterior chamber and vitreous humor. It can change its refractive power by changing its shape and altering the focal distance of the eye, which enables eye vision to accommodate to an object at a certain distance away. The iris is a circular disc located between the anterior chamber and the lens, which serves like a

diaphragm of a camera with a variable diameter to control the numerical aperture and light intensity received by the retina. After the lens, the light crosses the vitreous humor (containing a gel-like material) and is detected by the retina at the back of the eye.

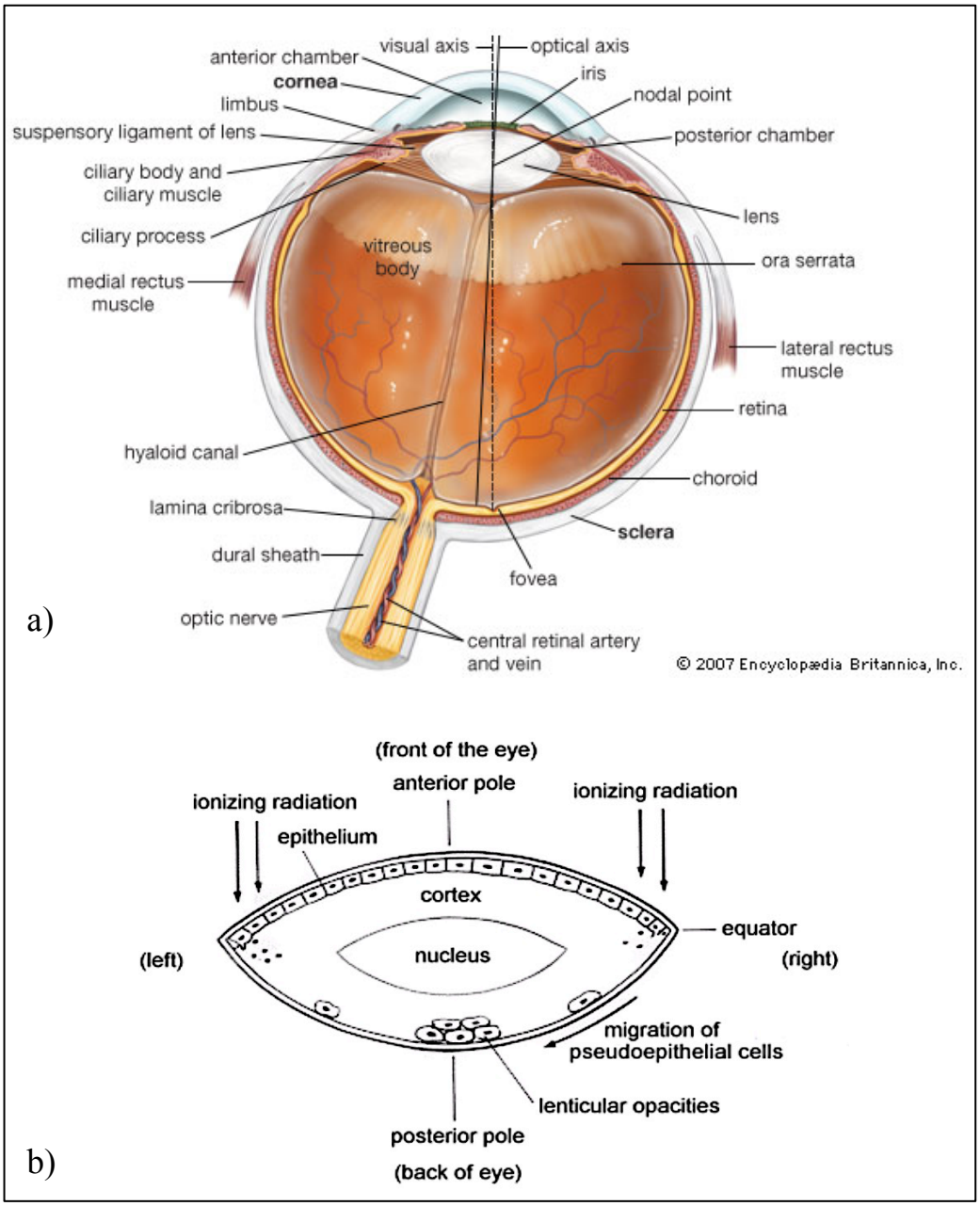

Figure 2.2. a) Schematic of the cross-section view of the eyeball (reproduced from (Davson, 2016)) and b) radiation cataract formation at the posterior sub-capsular region (reproduced from (Shigematsu *et al*., 1991)).

The retina is the visual sensory system, comprises of two types of neurons, named rods and cones. Rods contain a single visual photopigment rhodopsin with a peak absorbance spectrum (λ_{max}) of 497.6 $\pm$ 3.3 nm (sensitive to blue-green light) (Bowmaker & Dartnall, 1980), which are highly active during low light vision (scotopic vision). Cones are exclusively active during bright light vision (photopic vision) and it contains three visual photopigments sensitive to red (λ_{max} at 562.8 $\pm$ 4.7 nm), green (λ_{max} at 533.8 $\pm$ 3.7 nm), and the blue lights (λ_{max} at 420.3 $\pm$ 4.7 nm) (Bowmaker & Dartnall, 1980). They serve to detect the object's colour and detail. The density of the rods is considerably higher than cones, except in the fovea especially in the centre of fovea where it is even rod-free, which causes extreme visual perception.

Different areas of the lens show different sensitivity to radiation. The interior frontal side of the lens is covered by a transparent layer of epithelial cells, generated through cell division at the equator. Since the ionising radiation is tremendously damaging for dividing cells, the cells at the equator are the most prone to harm. Damaged cells and their products migrate to the posterior pole before converging at the centre and form a sub-capsular structure, which reduces the transparency of the eye lens (Figure 2.2b). Radiation cataract is a deterministic effect and inversely proportional to the delivered dose, which higher dose may cause cataract formation with shorter latency periods. Cataract formations are the late effects of radiation exposure. Unlike skin reactions, which are visible after about 2 weeks, they usually appear after 10-20 years.

The electron (beta radiation) and low energy photon radiation (diagnostic photon energy range) increase the risk of cataract formation (Behrens, 2011).

To date, different threshold dose has been proposed for cataract formation during acute radiation exposure (Table 2.1). The International Commission on Radiological Protection (ICRP) (Stewart *et al*., 2012) according to latest epidemiology studies (Worgul *et al*., 2007; Chodick *et al*., 2008; Vano *et al*., 2010; Mrena *et al*., 2011) issued

a new statement in 2011 on the threshold in absorbed dose to eye lens of 0.5 Gy, which was about four-times smaller than the threshold dose of 1-2 Gy suggested by the ICRP in 2007 (Valentin, 2007).

2.3. Radiation Effects

When ionsing radiation absorbed by the cells, deposit of the radiation energy to individual atoms, molecules, and biological cells causes cellular damage either indirectly or directly. Indirect cellular damage occurs when the ionising radiation creates reactive chemical compounds like free radical OH^* in the water medium (hydroxyl ion: OH^*) (Eq. 2.1). The free radical OH^* causes chemical changes in solute molecules, which initiate a whole series of follow detrimental reactions in tissue. The affected molecules include the nucleic acids (deoxyribonucleic and ribonucleic acids (DNA, RNA)) and proteins (like enzymes) produce gross subcellular changes, either desirable or deleterious, in the membranes, nuclei, and chromosomes, and eventually cause cell death (deterministic effects) or cellular transformation (stochastic effects) (Lomax *et al*., 2013),

$$H_2O + radiation \rightarrow H_2O^+ + e^- -> H_2O^+ \, decomposes \rightarrow H^+ + OH^*. \qquad \text{Eq. 2.1}$$

Direct cellular damage occurs when radiation causes breaking covalent bonds in the molecule, defecting lattice structure in crystalline materials, and causes various lesions in the bio-molecules of the cell (most importantly DNA strand). The radiation energy deposited in the DNA causes various lesions formed on single or double helical turns of the DNA, which can cause isolated DNA lesions, such as single-strand breaks (SSBs), damaged bases, abasic sites, and also closely spaced lesions, including cluster sites and double-strand breaks (DSBs) (Lomax *et al*., 2013) (Figure 2.3). Low linear energy transfer (LET) radiations during its travel through bio-molecules about 70% of its

energy deposited results in isolated lesions and about 30% in inducing clustered damage sites (Nikjoo *et al*., 1998). The complexity of DNA damage increases with LET. For high LET ionising radiations (like alpha radiation), about 90% of the energy deposited results in clustered damage sites (Goodhead, 1994) including about 70% complex DSB type (Nikjoo *et al*., 1998), which make them more critical than low LET radiations. The isolated lesions are normally repaired efficiently, since the unbroken strand provides the necessary information, but DSBs causes permanent damage to the cell, which induces the cancer risk.

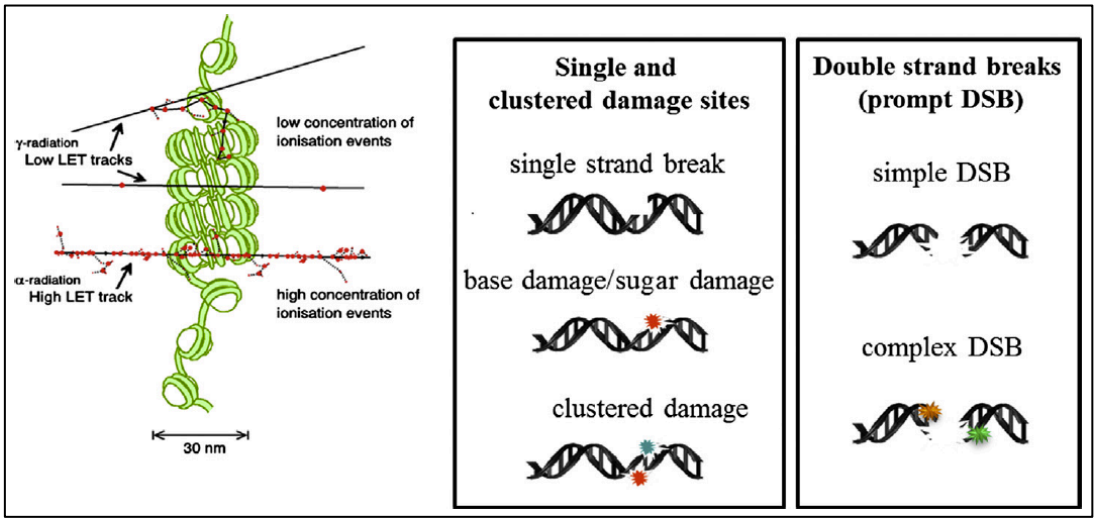

Figure 2.3 Schematic of various types of DNA damages caused by passage of a single radiation track. These DNA damages consist of single, clustered, and complex double-strand breaks (reproduced from (Lomax *et al*., 2013)).

2.4. Radiological Physics and Radiation Principles

Radiological physics is the science of ionising radiation and its energy deposition through the medium. This science initiated by the discovery of the x-ray by Wilhelm Roentgen, radioactivity by Henri Becquerel, and radium by the Pierre and Marie Curie in the 1890s. In a short time after these discoveries the x-rays and radium became a useful means in diagnostic and therapeutic applications in the medical. The interaction of the radiation with matter can either cause excitation, or ionisation. During the

excitation, the electron in electron orbit gains energy and upsurges to a higher energy level. When this electron de-excite, the difference between two energy levels is released in the form of radiation. Ionisation occurs when the radiation delivers enough energy to an electron to exit it from the medium. The ejected electron (also called "photo-electron") can interact with other electron orbits and cause damage to other atoms, breaking the adjacent molecule's chemical bonds. This radiation is called "ionising radiation", which must carries energy higher than 33.97 eV, the energy needed to cause an electron pair in dry air (Boutillon & Perroche, 1985). After releasing the photo-electron, the vacancy left in the atomic shell is filled with an electron from a higher atomic shell. The difference between two energy levels of atomic shells is released by an x-ray, which is called "characteristic x-ray".

International Commission on Radiation Units & Measurements (ICRU) in 1971 recommended a certain terminology in denoting to ionising radiations based on the interaction of charged and uncharged particles with matter and divided ionising radiation into two groups; directly and indirectly ionising radiation (Massey, 1974). The directly ionising radiation refers to ionisation of the medium by charge particles, which directly deliver their energies to medium. The indirectly ionising radiation denotes ionisation of the medium by uncharged particles like photons (x-ray and gamma (γ) ray) and neutrons. In this process the energy of uncharged particles is transferred to the charged particles and then charged particle energies deposited to the medium.

The x-ray is an electromagnetic wave emitted by charged particles in slowing down high energy electrons when pass next to the nuclei, which generate continues x-ray spectrum (called "bremsstrahlung x-ray") or in the interaction of the electron in electron orbits and changing their atomic energy level, thereby releases characteristic x-ray. The other type of the photon is γ-ray. The difference between these photon types is their mode of origin. The γ-ray is generated from an unstable nucleus or in annihilation

reactions among matter and antimatter. The energy of the x- and γ- rays (keV) can be calculated using Eq. 2.2 (Attix, 2008)

$$E = h\nu = \frac{hc}{\lambda}, \qquad \text{Eq. 2.2}$$

where E is energy of the electromagnetic photon (keV), h is the Plank's constant (equal to 6.626×10^{-34} J.s = 4.136×10^{-18} keV.s), c is speed of the light in vacuum (3×10^8 m.s^{-1}), and λ is photon wavelength.

2.5. Radiation dose quantities

Interaction of radiation field with matter can be described by three nonstochastic quantities, the kerma (K), the absorbed dose (D), and the exposure (X). Kerma (K) is the first step of indirectly ionising radiation interaction, which describes the energy transfer from uncharged particles to charged particles in the medium. The absorbed dose (D) defines the energy transfer to the medium, whether directly or indirectly ionising radiations, delivered by the charged particles. The exposure (X) shows the ability of x-ray and γ-ray to ionise air.

2.5.1. Kerma

The Kinetic energy released per unit mass (kerma) is a nonstochastic quantity applicable only for indirectly ionising radiation interaction (uncharged particles: photons or neutrons) (Eq. 2.3 & Eq. 2.4),

$$K = \frac{dE_{tr}}{dm} \qquad \text{Eq. 2.3}$$

$$E_{tr} = (R_{in})_{uncharged\ particles} - (R_{out})_{uncharged\ particles} + \sum Q. \qquad \text{Eq. 2.4}$$

Here dE_{tr} represents the total kinetic energies of all produced charged particles in the medium (mass: m). R_{in} is the total energy of uncharged particles entering the medium

volume (V), R_{out} is the net energy of uncharged particles leaving the V, and $\sum Q$ is the net energy originated from the rest mass in the medium (E → m is negative and m → E is positive).

Thus the kerma is kinetic energy transferred throughout a volume containing a mass m, which has been expressed in units of $J.kg^{-1}$ or Gy. The kerma is related to the photon spectral energy fluence ($\psi(E)$) and mass energy-transfer-coefficient ($(\frac{\mu_{tr}}{\rho})_{E,Z}$), which corresponds to the photon energy (E) and atomic number of the medium (Z) (Eq. 2.5):

$$K = \int_{E=0}^{E=max} \psi'(E) \,.\, (\frac{\mu_{tr}}{\rho})_{E,Z} \, dE \qquad \text{Eq. 2.5}$$

Where ψ'(E) is the differential distribution of photon spectral energy fluence. The kerma as mentioned earlier is the stage 1 of the indirectly ionising radiation interaction, which energy of the uncharged particles delivered to the charge particles (electrons and positrons). In the second stage, the kinetic energy of a fast electron released by one these two interactions, first, the collision interaction, expresses the interaction of the fast electrons with atomic electrons of the medium, which results ionisation and excitation (K_c), second, the radiative interaction, states deceleration of the fast electrons in the vicinity of the nuclei, resulting x-ray photon generation (bremsstrahlung radiation) (K_r). The net kerma is a summation of these two interactions (Eq. 2.6).

The collision kerma, which shows the expectation value of the energy transferred to charged particles relates to the photon spectral energy fluence ($\psi(E)$) and energy-absorption-coefficient ($(\frac{\mu_{en}}{\rho})_{E,Z}$) (Eq. 2.7)

$$K = K_c + K_r \qquad \text{Eq. 2.6}$$

$$K_c = \int_{E=0}^{E=max} \psi'(E) \,.\, (\frac{\mu_{en}}{\rho})_{E,Z} \, dE. \qquad \text{Eq. 2.7}$$

2.5.2. Absorbed Dose

The absorbed dose, D, is relevant to the expectation value of the energy imparted to matter through all types of ionising radiation fields (E), whether directly or indirectly ionising, per unit mass (m) of the absorbing medium (Eq. 2.8 & Eq. 2.9)

$$D = \frac{dE}{dm} \qquad \text{Eq. 2.8}$$

$$E = (R_{in})_{uncharged\ particles} - (R_{out})_{uncharged\ particles} + (R_{in})_{charged\ particles} - (R_{out})_{charged\ particles} + \sum Q. \qquad \text{Eq. 2.9}$$

The unit of absorbed dose is the same as the unit used for kerma, Gy. If the energy delivered to charged particles is deposited locally and radiative interactions (bremsstrahlung) are negligible, the absorbed dose, D, will be equal to the kerma, K.

The relative radiation hazard and its biological effects are defined by equivalent dose (H) and are product of absorbed dose (D) and quality factor (Q). Q is a weighting factor depends on both particle energy and type, which is equal to 1 for x-rays and gamma rays. The unit of equivalent dose is the Sievert (Sv) that has same physical dimensions (J. kg^{-1}) as absorbed dose, Gy.

2.5.3. Exposure

The International Commission on Radiation Units and Measurements (ICRU) in 1980 defined the exposure as "the quotient of dQ by dm, where the value of dQ is the absolute value of the total charge of the ions of one sign produced in air when all the electrons (negatrons and positrons) liberated by photons in air of mass dm are completely stopped in air. " (ICRU, 1980) (Eq. 2.10),

$$X = \frac{dQ}{dm}. \qquad \text{Eq. 2.10}$$

The dQ value does not comprise electrons generated by the secondary photons (bremsstrahlung radiation).

Exposure describes the only x-ray and γ-ray photons ability to ionise air and has been expressed in units of Rontgen (R) and C.kg^{-1} with a conversion factor of (Eq. 2.11) (Attix, 2008)

$$X\left(\frac{C}{kg}\right) = 2.58 \times 10^{-4} \times X(R). \qquad \text{Eq. 2.11}$$

The exposure, X, is equivalent to air-kerma (K_{air}). To generate an ion-pair in a gas we need to deposit energy, which is symbolised by $\overline{W}$ (Attix, 2008). The $\overline{W_{air}}$ shows the mean energy extended in dry air per ion-pair produced, which is equal to 33.97 eV per ion-pair ($\frac{\overline{W_{air}}}{e}$ = 33.97 J.C^{-1}) (Boutillon & Perroche, 1985). Referring to Eq. 2.12, the exposure can be defined due to the photon spectral energy fluence $(\psi(E))$

$$X = \int_{E=0}^{E=max} \left(\frac{e}{\overline{w}}\right)_{air} . \psi'(E) . \left(\frac{\mu_{en}}{\rho}\right)_{E,air} dE. \qquad \text{Eq. 2.12}$$

Exposure, X, is considered as a useful and valuable information about x-ray or γ-ray characteristics due to, it is proportional to the photon energy fluence $(\psi(E))$ and since the elements in the air is appropriately similar to biological soft tissue (muscle) in terms of its effective atomic number, thus the exposure can be used as a substituted reference to study the effects of such radiations in tissue ($\frac{(\frac{\mu en}{\rho})_{E,muscle}}{(\frac{\mu en}{\rho})_{E,air}} = 1.07 \pm 3$ % total spread) over the energy range of 4 keV to l0 MeV (Figure 2.4).

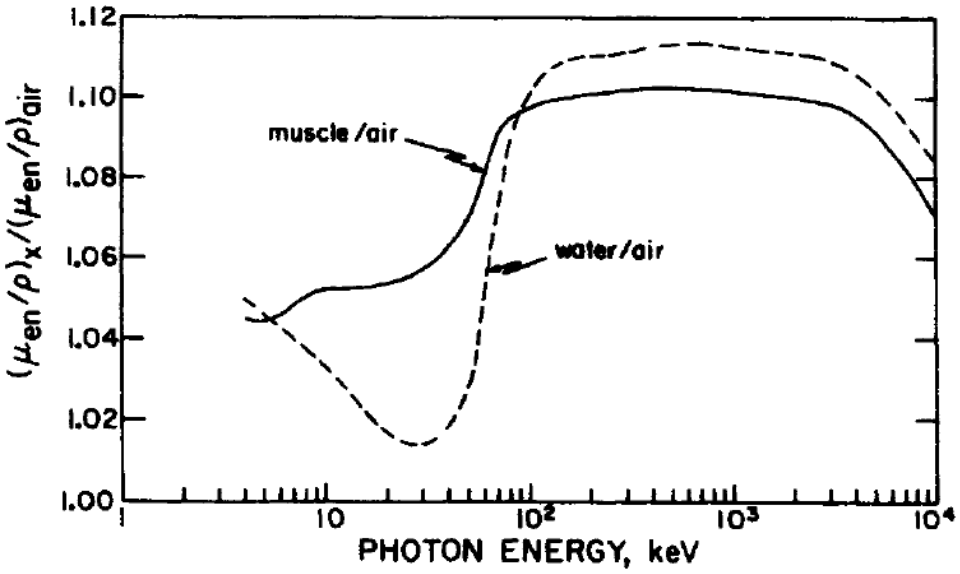

Figure 2.4. Ratio of mass energy absorption coefficient for muscle and water relative to air (reproduced from (Attix, 2008)).

2.6. Fluoroscopy Guided Interventional Radiology

Interventional radiology (IR) has become a common medical practice providing the opportunities to treat a wider range of pathologies as an effective method to diagnose and treat numerous vascular and cardiac diseases. This treatment technique represents tremendous advantages over invasive surgical procedures, like less trauma to the patient, lesser requirements for general anaesthesia, lower treatment costs, extremely small incision required, which resulted in lower infection risk and shorter hospitalisation time (UNSCEAR, 2010). During fluoroscopy guided interventional radiology procedures, ionising radiation is used to guide catheter, guide wire, and other small instruments through the blood vessels of the patient. Complex and repeated interventional procedures may increase the risk of tissue reaction effects like radiation-induced skin injuries and cataract formation. Skin injuries are the most frequently encountered tissue reaction effects from interventional procedures (Wagner *et al*., 1999; Mooney *et al*., 2000; Wolff, *et al*., 2001; J. Lee *et al*., 2003; Frazier *et al*., 2007; Balter *et al*., 2010; Spiker *et al*., 2012). The U.S. Food and Drug Administration (FDA) (FDA,

1994), the World Health Organization (WHO) (WHO, 2000), the International Commission on Radiological Protection (ICRP) (Valentin, 2000), and the International Atomic Energy Agency (IAEA) (IAEA, 2010a) have all expressed concerns regarding patient skin dose. They have also issued guidance on the prevention of skin injuries in high dose interventional procedures. In order to prevent severe radiation injuries, it is important to evaluate the entrance skin dose of patients during long irradiation periods.

Eye lens is another organ at risk during neuro-interventional procedures, since during these procedures patient's eye lenses are frequently placed within the radiation field and risk of lens opacity and cataract formation, especially among young patients, patients with visual impairment, and patients who required prolonged neuro-interventional procedures are higher. Table 2.1 shows threshold doses for different tissue reactions of skin and eye lens summarised from the literature. Early skin reactions (early erythema) can be observed after 2 Gy (Wagner, 1998), which can be encountered 2-24 hours after the irradiation. There is no definite threshold dose for skin cancer, but the skin cancer generally occurs after 15 years from the radiation.

Table 2.1 Threshold doses for inducing various tissue reactions in skin and eye.

Effect	Approximate threshold absorbed dose (Gy)	Time of onset of the effect	Fluoroscopy time (in min) to reach threshold at:	
			Usual dose rate of 20 mGy.min^{-1} (2 rad.min^{-1})	High-dose rate of 200 mGy.min^{-1} (20 rad.min^{-1})
Skin[a]				
Early transient erythema	2	2- 24 hours (hours [c])	100	10
Temporary epilation	3	≈ 3 weeks	150	15
Main erythema	6	≈ 1.5 weeks	300	30
Permanent erythema	7	≈ 3 weeks	350	35
Dry desquamation	14 (10 [b])	≈ 4 weeks	700 (500 [b])	70 (50 [b])
Invasive fibrosis	10 [b]	N/A	500 [b]	50 [b]
Dermal atrophy	11	> 52 weeks (14 weeks [b])	500 (552 [b])	50 (55.2 [b])
Telangiectasia	12	> 52 weeks	500 (600 [b])	50 (60 [b])
Late erythema	15	8-10 weeks (6-10 weeks [b])	750	75
Moist desquamation	18 (15 [b])	> 4 weeks	900 (750 [b])	90 (75 [b])
Dermal necrosis	> 12 (18 [b])	> 52 weeks (> 10 weeks [c])	750 (900 [b])	75 (90 [b])
Secondary ulceration	24 (20 [b])	> 6 weeks	1200(1002 [b])	120 (100.2 [b])
Skin cancer	N/A	> 15 years	N/A	N/A
Eye[a]				
Lens opacity (detectable)	> 1-2 (0.5-2 [d])(0.5 [e])	> 5 years	> 50 to eye	> 5 to eye
Lens/ cancer (debilitating)	> 5	> 250 years	> 250 to eye	> 25 to eye

a) (Valentin, 2000)
b) (Wagner *et al*., 1994)
c) (Mettler, *et al*., 2001; Lee *et al*., 2003)
d) (Valentin, 2007)
e) (Stewart *et al*., 2012)

2.7. Dose Metric Parameters

Different dose metric parameters have been established to evaluate patient's skin dose during interventional procedures. In general, they can be divided into the indirect and direct dose measurement methods (Geise & O'Dea, 1999; Balter *et al*., 2002). Under the umbrella of the indirect dose measurement method, dose metrics that are often used are, fluoroscopic time (FT), kerma-area-product (KAP), dose level at the interventional reference point (IRP), and peak skin dose (Balter *et al*., 2002; Jaco & Miller, 2010). As for the direct dose measurement methods, some type of radiation dosimeter would be required.

2.7.1 Indirect Dose Measurement Methods

2.7.1.1. Interventional Reference Point

Reference dose or originally called cumulative dose was first introduced by the International Electrotechnical Commission (IEC) in 2000 (IEC, 2000). In this dose measurement approach, cumulative air-kerma at a fixed point in space between the x-ray tube and the image receptor, which has a highest possibility of positioning the patient's skin during a clinical procedure, is presented as a patient's maximum skin dose. This point is called the Interventional Reference Point (IRP) and it is fixed relative to the x-ray tube and is independent to the patient variation. The IEC's definition of the IRP in C-arm fluoroscopy system is located 15 cm from the isocentre of the C-arm toward the x-ray tube (IEC, 2000). The U.S. Food and Drug Administration's (FDA) definition of the reference dose is to measure accumulated entrance air-kerma at the 30 cm in front of the image receptor C-arm for fluoroscopy systems (FDA, 2009).

Since 2006, the FDA has issued a criteria that every fluoroscopy unit sold in the USA should be able to calculate, display, and record reference dose (FDA, 2005). The

cumulative reference dose is displayed in real-time on system monitors during the clinical procedures and has been used as an indicator for the patient's total skin dose for the clinical procedure. The IRP is fixed relative to the x-ray tube as it is always at a constant distance from the isocentre, which may represent a position on the patient's skin or a point inside or outside of the patient's body (Figure 2.5). The IRP rarely represent the exact location of the patient's skin over clinical procedures. Using accumulated doses at IRP locations tends to be higher than actual peak skin doses and consequently overstates the radiation risk to the patient (Miller *et al*., 2003).

Calculating the patient's entrance skin dose (ESD) from reference dose demands to consider the actual x-ray source to skin distance (SSD), exposure field size at the patient's skin location (FS_p), attenuation of treatment couch and mattress, tissue backscatter factor (BSF) for the field area at the SSD, and considering of mass–energy absorption coefficient ratio of tissue to air (Eq. 2.13) (McParland, 1998)

$$ESD = K_{c,air}(SSD) \times BSF(FS_p) \times (\frac{\mu_{en}}{\rho})_{air}^{tissue}, \qquad \text{Eq. 2.13}$$

where $K_{c,\,air}$(SSD) indicates the collision kerma in the air at a defined distance from the x-ray source (SSD), BSF(FS_p) is the tissue backscatter factor for a specific exposure field size (FS_p), and $(\frac{\mu}{\rho})_{air}^{tissue}$ is mass–energy absorption coefficient ratio of tissue to air.

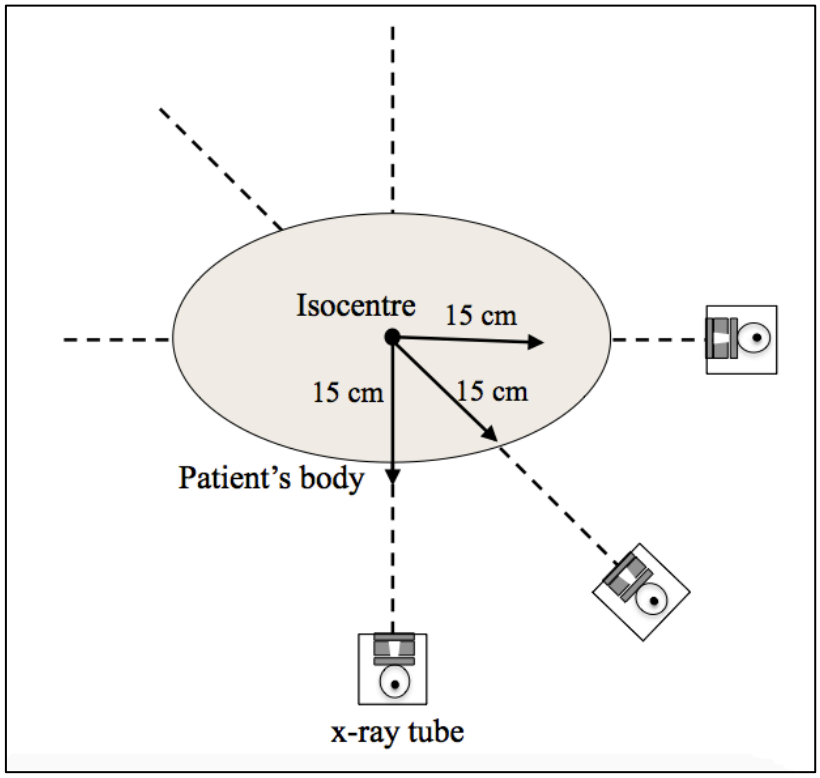

Figure 2.5 The IRP positions (IEC method) during a clinical procedure, which can be placed inside, outside, or on patient's skin.

2.7.1.2. Kerma Area Product

The kerma-area-product (KAP) is air-kerma at a point along the central axis of the x-ray beam, multiplied by the exposure field size at that point ($mGy.cm^2$). Exposure field size increases as the square of the distance and the radiation dose decreases as the square of the distance from the x-ray tube. Therefore, the two parameters cancel each other out resulting in independency of the KAP to distance between x-ray to the patient's skin. The KAP is used to measure the total energy absorbed by the patient; therefore, it is a good dose metric for approximating stochastic risk during a clinical procedure (Miller *et al*., 2010; Gupta *et al*., 2013).

KAP can be determined by calculation or using a transmission full-field ionisation chamber placed between the collimators and the patient's body. KAP provides no information regarding the radiation dose distribution over the patient's body. The same

KAP is observed with small field size and high radiation dose with large exposure field size and low radiation dose (Figure 2.6a). In order to reduce the uncertainty of patient's skin dose normally a nominal exposure field size is used for typical procedures. Calculating the patient's ESD from KAP requires taking into account the actual SSD and exposure field size on the patient's skin. The actual exposure field size can be calculated using the inverse square law to convert the exposure field size generated at the image receptor distance to the actual exposure field size on the patient's body.

However the KAP dose metric has shown to have reasonably high correlation with maximum skin dose for a large group of patients; other hand, it presented a poor correlation for patient's dose during an individual procedure (Fletcher *et al*., 2002; Miller *et al*., 2003).

2.7.1.3. Time

Fluoroscopy time is one of the common dose metric methods used to estimate patient's dose during fluoroscopy guided interventional procedures. The fluoroscopy time has been known to be a poor patient's dose indicator, since in this method, there is the total lack of information regarding the fluoroscopy dose rate (Figure 2.6b) and dose due to other fluorographic imaging (acquisition imaging techniques) are not taken into account. In addition fluoroscopy time does not provide any information about patient's skin dose distribution.

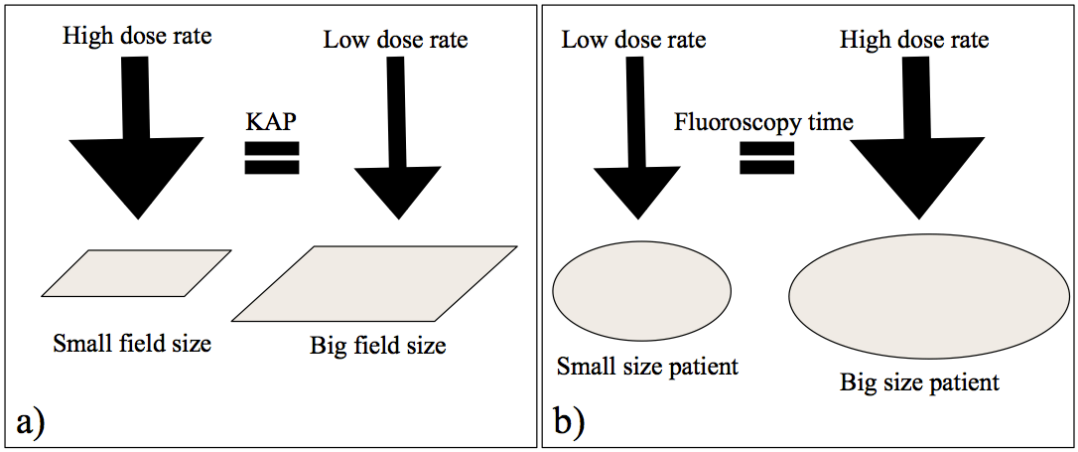

Figure 2.6 The uncertainties associated by estimation of the patient's skin dose using a) KAP and b) fluoroscopy time metrics (adapted from (Jaco & Miller, 2010)).

2.7.2. Direct Dose Measurement Methods

2.7.2.1. Radiochromic Film

Various types of film have been widely used to evaluate the patient's dose for diagnostic and interventional x-ray procedures. Dosimetry using film provides detailed indications of the location and amount of the patient's maximum skin dose and distribution of radiation dose over the patient's skin. Vano *et al*., (2001) investigated the patients' maximum skin doses (MSD) during 26 coronary angiography and 7 percutaneous transluminal coronary angioplasty (PTCA) procedures by using radiographic slow film and studied the correlation of MSD values with DAP and cumulative dose (total AK) measured by an ion-chamber (Vano *et al*., 2001). In this study the range of the maximum patients' skin dose was reported 107-711 mGy, which showed no correlation with DAP (27.3-370.6 $Gy.cm^2$) and estimate cumulative skin dose values (110-3706 mGy). This study found that the DAP and total AK at the estimated level of the patient's skin are not reliable indicator for actual radiation dose received by the patient's MSD.

As mentioned earlier one of the unique advantages the film dosimetry is its ability to provide high-resolution 2D dose distribution information. This advantage enabled Schueler and his colleagues to study the difference between patient's skin dose distribution during a 3D rotational angiography and digital subtraction angiography (DSA) (Schueler *et al*., 2005). This study also compared MSDs with AK values. This study revealed that the patient's MSD dose during a 3D rotational angiography (15 mGy) was significantly lower than a biplanar DSA (58 mGy). In addition the study of the patient's skin dose distribution showed that, for both imaging techniques the MSDs were generally located at the occipital region. The AK indicator overestimated the patient's MSD during the 3D rotational angiography by a factor of 2.2–2.5, because the total AK value cumulates entire entrance skin dose during rotation and considers it as a MSD value. AK slightly underestimated MSD during biplanar DSA, due to not considering the contribution of the backscatter radiation on patient's skin dose.

The patients' MSDs during interventional neuro-radiological procedures were also measured using Gafchromic® XR type R films (D'Ercole *et al*., 2007). In this study 21 patients undergoing embolization of aneurysms procedures were participated in order to study the correlations of MSD values with fluoroscopy time and DAP. The correlation (r^2) of MSD with fluoroscopy time and DAP were reported to be 0.61 and 0.77, respectively.

Having a wide operating range; for instance Gafchromic® XR-RV3 film with a sensitive range to x-ray energies of 30 keV to 30 MeV and dose range of 0.01 Gy to 30 Gy (Appendix A), represents this film as a sufficient method for quantitative mapping of patient's skin dose during various diagnostic and interventional procedures. The Gafchromic® film is a self-developing dosimeter, which can be used easily during a clinical procedure. The limitations of film as a dose monitoring system are, it is not able to provide real-time feedback and only can be used as a post-processing dose evaluation

methods, not reusable, and is energy dependent, which can be an important issue especially for fluoroscopy guided interventional radiology procedures that are always performed with various exposure energies.

2.7.2.2. Thermoluminescence Dosimeters

A dose measurement using TLD chip provided several advantages like, having a small physical size (1 × 1 mm^2 crystals) enables this detector to be used as a point dose measurement system, reusability, ability to store accumulated dose with negligible signal fading (< 10% per year (Kron, 1995)), practically tissue equivalent, and does not require electrical connection to collect the radiation dose. On the other hand, this dosimeter has some limitations like, this detector does not provide real-time dose information and can be read only once and all signals erased throughout readout procedure. TLDs have effectively been used as a point dosimeter to record the radiation dose received by radiosensitive organs during various interventional radiology procedures (Berthelsen & Cederblad, 1991; Meriçı *et al*., 1998; Ilgit *et al*., 2000; Sandborg *et al*., 2010). As a point dose measuring system, it may not be placed at the location of MSD on the patient's body, which consequently causes an underestimation of radiation dose for that particular procedure. Efstathopoulos *et al.* studied patients' MSDs during 307 percutaneous coronary interventional procedures by using TL dosimeters. This study recorded the MSD of 182 mGy (Efstathopoulos *et al*., 2004), which was considerably lower than previous reports (Hwang *et al*., 1998; Putte *et al*., 2000; Vano *et al*., 2001). One of the possible factors that might cause this discrepancy is high dependence of measured MSD to TLDs positions, since maximum measured dose by TLDs is not always the maximum radiation dose received by the patient's skin.

A technique for using arrays of TLDs has been proposed to reduce the uncertainty of miss-positioning the TLD chips. As the separation between the TLDs reduces, the

chance of recording the patient's MSD increases. Theodorakou & Horrocks in 2003 measured the dose received by 30 patients during coil, glue and stent embolisation procedures using a TLD-100 chips array in order to measure patients' MSDs and TLD-100H for measuring the patient's eye lens and thyroid gland doses. They reported a good linear correlation between the posterior-anterior DAP and the MSD measured by TLD (r^2=0.86) and slightly lower correlation factor (r^2=0.79) was measured for the lateral plane DAP and the patients' MSDs. The number of images of the posterior-anterior and lateral plane showed good correlation with DAP (r^2=0.73 and r^2=0.67, respectively). The average patient's eye lens thyroid gland doses were reported 60 mGy and 24 mGy, respectively and the maximum eye dose recorded for the 30 patients was found to be 50 cGy (Theodorakou & Horrocks, 2003).

2.7.2.3. Radiophotoluminescence Glass Dosimeters

Several papers have been published on using radiophotoluminescence glass dosimeters (RPLDs) for patient's dose measurement during interventional radiology procedures (Nishizawa *et al*., 2003; Moritake *et al*., 2008; Hayakawa *et al*., 2010; Takashi Moritake *et al*., 2011). The RPLDs provide several advantages over TLDs, such as this detector can be read repeatedly unlike TLDs, which are reset after each reading, and its radiolucency under fluoroscopy and acquisition imaging (Nishizawa *et al*., 2003). Another merit of a RPLD is its small physical size, which can be placed in many points of the patient's skin surface to provide a geometric distribution of the patient's ESD with higher resolution in comparison with other point dosimetry systems. There are some limitations for the RPLD to be used during clinical fluoroscopy procedures like, the sensitivity of this detector highly dependents on photon energy and these procedures are generally performed with a wide range of photon energies (controlled by Automatic Dose Rate Control (ADRC) system) and the RPLD is also not able to provide real-time dose information for operators during a clinical procedure.

2.7.2.4. Metal-Oxide Semiconductor Field Effect Transistor Dosimeters

Metal oxide semiconductor field effect transistors (MOSFETs) are transistor components, which have commonly been used in electronic devices and computer logic circuits since 1960s. Holmes-Siedle in 1974 first reported the capability of the MOSFET as a space-charge dosimeter (Holmes-Siedle, 1974) and later it was successfully used in space dosimetry in the satellite Geos-II (Holmes-Siedle, 1994) and other orbiting satellites (Ravotti *et al.*, 2007). The MOSFET dosimetry system has been widely used in medical application during radiotherapy (Consorti *et al*., 2005; Qi *et al*., 2007; Qi *et al*., 2009) and radiology procedures (Hurwitz *et al*., 2007; Yoshizumi *et al*., 2007; Einstein *et al*., 2010), due to its high sensitivity, immediate dose readout, storing the accumulated dose, reusability, and extremely small physical size. This detector also provides several disadvantages for radiation dose monitoring during a clinical procedure, such as its limited lifespan (200 and 70 Gy for low and high sensitive MOSFET, respectively (Peet & Pryor, 1999)), energy dependence (sensitivity changes by a factor of 3.2 for varying the tube potential from 50 kVp to 10 MV (Cheung *et al*., 2009)), temperature dependence (50 mV for temperature change over 20 to 40 °C (Cheung *et al*., 2004)), and changing the sensitivity with accumulated dose.

The MOSFET detectors have been used to measure the patient's skin dose during fluoroscopy guided interventional procedures (Peet & Pryor, 1999; Glennie *et al*., 2008; D'Alessio *et al*., 2013). The criteria of a detector used for monitoring ESD during interventional radiology procedure include: small physical size to preserve the image quality, the ability to provide real-time feedback, linear response to wide range of the radiation dose, simple to use, and exhibits a specific water equivalent depth (WED) for monitoring the skin dose (0.07 mm ICRP, 1991)).

2.8 MOSFET Design and Principle of Operation

MOSFET is a sandwich type device made up of a source (S), gate (G), drain (D), semiconductor substrate (SB), and insulating silicon dioxide layer (SiO_2) (Figure 2.7a). The SiO_2 layer is placed underneath the gate terminal and channel layer is a portion of the silicon substrate, which places below the oxide layer and connects the source and the drain terminals. Depending on the type of charge of the channel current the MOSFET can be categorised to an n-channel (electron transmission) or a p-channel (hole transmission). As Figure 2.7 depicts the p-channel MOSFET (p-MOSFET), which consists of a negative doped (n-type) silicon substrate, two positive doped (p-type) silicon regions are situated underneath the source and the drain terminals, and silicon dioxide layer is located underneath the gate terminal.

The minimum gate voltage (V_G) is required to initiate a noticeable and constant current flow (I_{DS}) through the channel layer is defined as the MOSFET threshold voltage (V_{TH}). When the gate voltage is set to zero ($V_G = 0$) the detector is in "off" state and the source-drain current only contains a negligible amount of electron-hole recombination ($V_{GS} < V_{TH}$ and $I_{DS} \sim 0$). When a small negative voltage is applied to the gate terminal, the SiO_2 layer's electrons will be depleted, but the source-drain current is still negligible. When a sufficiently large negative voltage is applied to the gate terminal, most of the holes carriers are attracted to the SiO_2-Si interface from the SB, source and drain regions.

The accumulated holes carriers at the SiO_2-Si interface generates the conduction channel, which allows electron current flow between the source and drain terminals (I_{DS}). The MOSFET detector is now in its "on" state. In this stage, $V_{GS} > V_{TH}$ and their difference is called "overdrive voltage" ($V_{OV} = V_{GS}-V_{TH}$).

When $V_{DS} < V_{OV}$, the transistor is in "Triode" state and the I_{DS} is calculated by following equation (Eq. 2.14):

$$I_{DS} = k_n \left(V_{OD} - \frac{V_{DS}}{2}\right) \times V_{DS}, \qquad \text{Eq. 2.14}$$

where k_n is the transistor's conductance coefficient.

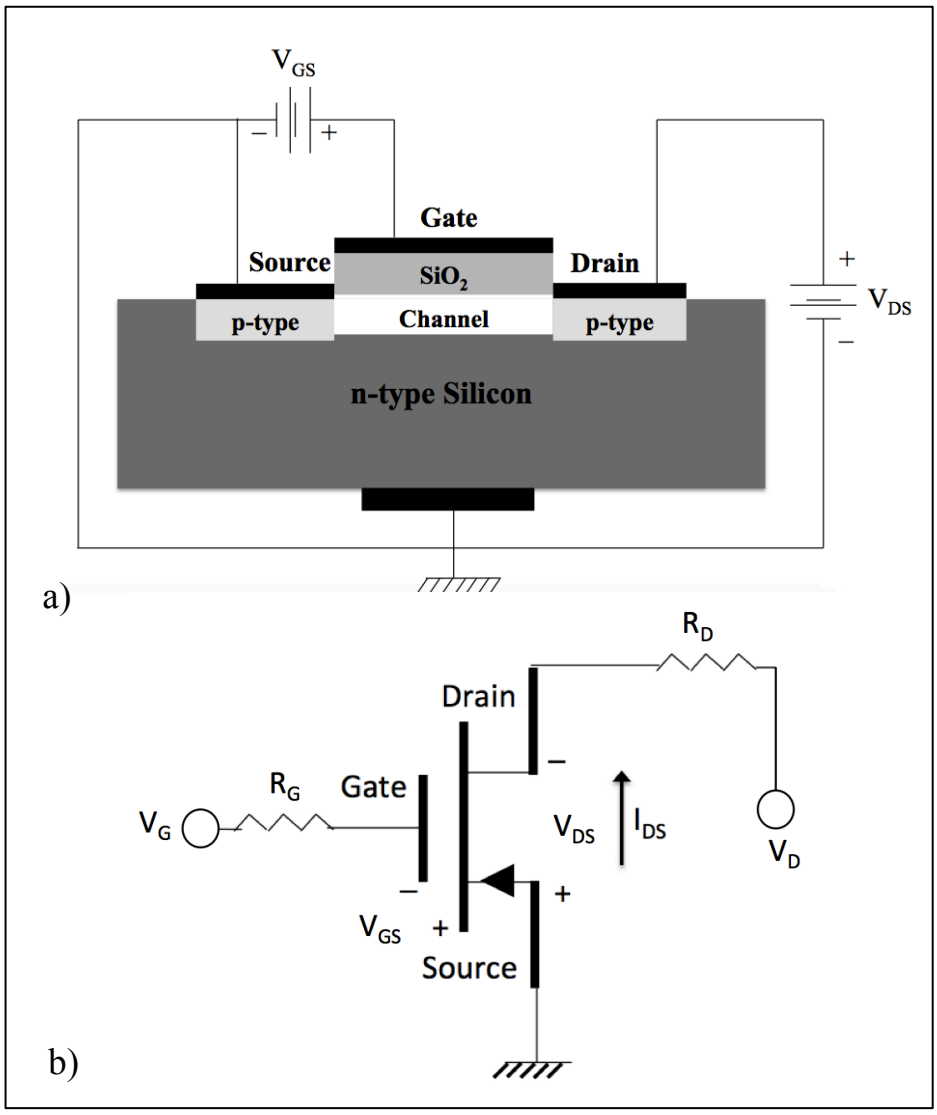

Figure 2.7 a) The structure of a p-type MOSFET detector, which consists of the gate, source, and drain terminals and Si, SiO_2, and channel layer. b) The electronic circle of a p-type MOSFET sensor.

The ionising radiation generates electron-hole pairs in SiO_2 layer. For generation of an electron hole pair in SiO_2 layer energy of 18 eV is required (Rosenfeld, 2006). The electrons move toward the gate terminal and holes undergo a stochastic hopping transport are trapped in the Si-SiO_2 interface, which causes a positive charge buildup. This positive charge buildup will considerably change the I_{DS} and for having a constant current flow (e.g. 50 μA) through the channel needs a corresponding negative shift in the V_{TH} at the gate.

In general, the MOSFET detector works on the principle of the shift in the threshold voltage of the gate terminal (ΔV_{TH}). The shift in V_{TH} corresponds to the absorbed dose in the SiO_2 layer (D), SiO_2 thickness (t_{OX}) ranging from 0.69 μm to 2.3 μm (Ensell *et al*., 1988)), and fraction of holes created that escaped recombination (f) (Eq. 2.15) (Ensell *et al*., 1988)

$$\Delta V_{TH} = 0.04 D t_{0X}^2 f. \qquad \text{Eq. 2.15}$$

By increasing the positive bias voltage to the gate, the *f* approaches to 1 (Rosenfeld, 2006) and extends the detector's sensitivity and dose linear region until the hole-traps at channel layer are saturated. After this stage the MOSFET threshold voltage doesn't change and the detector cannot be used any longer.

The MOSFET can be used as an active detector with a positive gate bias voltage or passive detector without using a bias voltage on the gate terminal. While the passive dosimetry system doesn't need bias supply during the measurement, the dosimetry procedure will be become more portable and easier in comparing to active detector, whereby the detectors need to be connected to bias supply when in use. However, the passive MOSFET detector can be utilised for a limited dose range and shows the sub-linear dose response (Rosenfeld, 2002). One of the example of a commercialised passive MOSFET detector is the OneDose™ MOSFET detector system (Sicel Technologies, Inc, USA), which is a single radiation dosimetry system and is recommended to be used

for radiation dose up to 5 Gy (Halvorsen, 2005). Having bias voltage on the gate reduces the electron-hole recombination, increases the hole trapping efficiency, and subsequently improves the MOSFET detector linearity over a wider dose range (Butson *et al*., 1996). Different gate bias causes different threshold voltage shifts for a constant radiation dose. As the bias voltage increases, the shift of the threshold voltage of the MOSFET sensor rises (Figure 2.8) (Litovchenko *et al*., 1990).

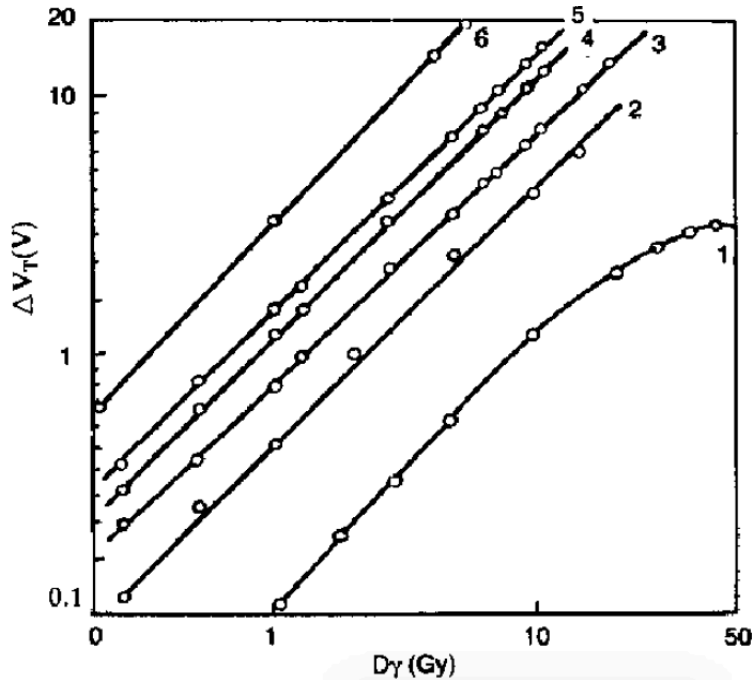

Figure 2.8 Shift of the n-MOSFET sensor's threshold voltage as a function of the bias voltage and irradiation dose, each curve represents the sensor response for each individual bias voltage (in V): 1 (0 V), 2 (4.5 V), 3 (8 V), 4 (16 V), 5 (24 V), and 6 (90 V) (reproduced from (Litovchenko *et al*., 1990)).

The mobility of the charge carriers in the channel layer is influenced by temperature. A study on temperature dependence of the MOSFET detector reported the threshold voltage variation of 50 mV for temperature change over 20 °C to 40 °C (Cheung *et al*., 2004). A research on temperature dependence of the p-MOSFETs revealed that the detector signal is altered about 0.3% per ºC in the temperature range between 22 °C and

40ºC (Ehringfeld *et al*., 2005). In research on micro-MOSFETs revealed that, increasing the temperature from 20 °C to 40 °C changes the detector response up to 0.5 % (Ramaseshan *et al*., 2004). Soubra *et al.* in their experiment on dual MOSFET revealed that this detector is almost independent of temperature. These detectors use different gate biases, which cause different threshold voltage shifts and subtracting of these signals is an independent reading to temperature (Soubra *et al*., 1994).

MOSFET detector has a finite lifetime due to the accumulation of radiation dose, which saturates the hole-traps near the Si-SiO_2 interface. The lifetime threshold voltage was reported to be approximately 24 V (Qi *et al*., 2007). After this threshold voltage the detector can be annealed by UV or thermal processes (Ristić, 2009) or by injection of charge carrier into the gate oxide (Alshaikh *et al*., 2014).

MOSFET post-irradiation readout accuracy depends on the MOSFET voltage fading and creep-up effect. MOSFET voltage fading attributes to mechanisms like, relaxation of charges residing in deep traps of the oxide layer, diffusion of positive ions, thermal and non-thermal annealing of trapped charges, and capacitance voltage hysteresis. MOSFET voltage fading depends on the readout interval. To avoid “signal fading”, it is recommended to read the detector’s signal during the first 15 minutes after irradiation (Ehringfeld *et al*., 2005). When the MOSFET threshold voltage increases with consecutive reading, is called “creep-up” effect, which depends on the time between successive read cycles. The MOSFET detector’s threshold voltage increases due to the residual of the injected charge of the previous measuring circuit and causing a temporary perturbation in the charge distribution. This effect is most pronounced for accumulated doses over 20Gy and this uncertainty can be reduced with a 1-minute wait time after initial reading (Ramani *et al*., 1997).

2.9. Chapter Summary

A review of existing literature about the measurement of the patient's radiation dose during interventional radiology procedures showed that much of the research in this area have a general tendency to only evaluate the radiation dose received by the patient's skin and radiation dose received by other radiosensitive organs have been rarely considered. No such studies of patient's eye lens dose correlation with dose metric parameters during neuro-interventional procedures have been performed. Moreover, the contribution of the exposure parameters on patient's eye lens dose is unclear.

During interventional procedures patient's dose may vary widely, which indicates the importance of *in-vivo* radiation dose measurement especially for radiosensitive organs like eye lens during complex neuro-interventional procedures. As pervious sections indicated, so far, various *in-vivo* dose monitoring system have been used to measure the patient's dose during clinical interventional procedure as post-processing dose evaluation methods, which have not had any impact on patient's radiation dose during each particular intervention. Currently, there is no real-time *in-vivo* dosimetry system that has been used for patient's dose monitoring during interventional radiology procedures. A real-time dose-monitoring system does not only provide real-time information about the total accumulated dose in the detector, but also enables us to study the contribution of each particular exposure on patient's dose.

The aim of the present thesis is to study the correlation between patient's eye lens doses with dose metric parameters and investigate the contribution of various exposure parameters on radiation dose received by the patient's eye lens during neuro-interventional procedures. Moreover, there is a need to consider the contribution of exposure parameters on patient's eye lens dose during neuro-interventional procedures.

To address these research gaps, the present thesis aims to introduce a new real-time dose monitoring system in order to evaluate the patient's eye lens dose during clinical

interventional procedures and also study the contribution of each exposure parameter on patient's dose, which could provide valuable guidance for interventional radiologists and radiographers in balancing the expected clinical benefits and radiation risks of performing an interventional radiology procedure.

In order to avoid repeating explanation of various research equipment, which were used through the present thesis, main equipment and their descriptions are presented in chapter 3.

CHAPTER 3: MATERIALS AND METHODS

3.1. MO*Skin* Detector

The MO*Skin* detector is a type of MOSFET detector prototyped and developed by the Centre for Medical Radiation Physics (CMRP), University of Wollongong, Australia. The MO*Skin* detector was designed especially for skin dose measurements (Kwan *et al*., 2008). This detector has previously been tested and found to be suitable for skin dose measurement in radiation therapy (Kwan *et al*., 2008; Qi *et al*., 2009; Alnawaf *et al*., 2012). The MO*Skin* detector was designed in a new packaging structure in which the p-MOSFET sensor with a gate oxide thickness of 0.6 μm is hermetically sealed into a Kapton pigtail strip using "drop-in" packaging technology (Figure 3.1). A thin polyamide film layer works as a moisture protector and build-up layer and gives a WED of approximately 0.07 mm in tissue (Kwan *et al*., 2008; Kwan *et al*., 2009), unlike the commercial MOSFET detector, which utilises wire-bonding and an epoxy bubble encapsulation above the sensitive region (Figure 3.1b).

The MO*Skin* detector response (ΔV_{TH}) can be recorded either manually from the reader (Figure 3.1a) or automatically via computer software MOSPLOT2 (version 1.0) and FETch (version 1.0), which are the control software programmed to record and display the detectors' responses automatically. Dose measurements can be performed at user-defined readout frequencies (minimum sampling rate of 1s). This feature allows for the near real-time visualisation and monitoring of radiation exposures during interventional radiology procedures. The MOSPLOT2 software presents a graph showing accumulated dose as a function of elapsed time (Figure 3.2a).

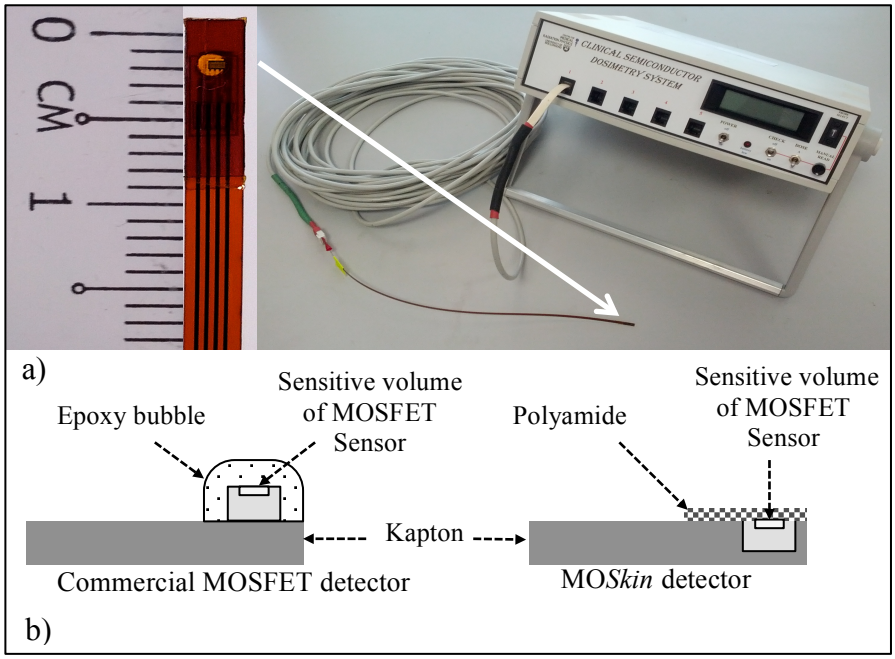

Figure 3.1 Photo of, a) the MO*Skin* dosimetry system and b) schematic diagram of the MOSFET detector with an epoxy bubble encapsulation and MO*Skin* detector with a layer of polyamide film.

A separate graphic user interface, FETch, was designed to present the dose values in a more visual form. This interface displays the accumulated dose in column bar charts and numeric form (Figure 3.2b). With this interface, the operators are able to monitor the radiation dose received by the patient in a more intuitive and direct manner, providing valuable information with minimal or no distraction to the interventional radiologist during a clinical procedure.

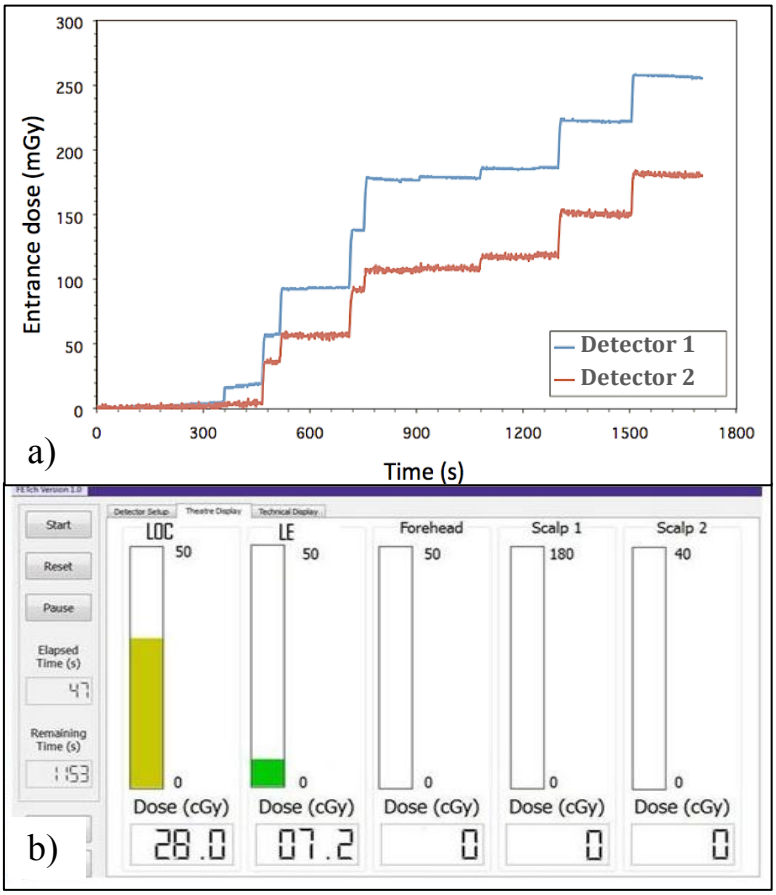

Figure 3.2 Schematic of the a) MOSPLOT2 and b) FETch software. These software display the accumulative dose trend in line and column bar charts, respectively.

3.2. Gafchromic® Film XR-RV3

Gafchromic® XR Type R (International Specialty Products, Wayne NJ) is a radiochromic film, particularly designed for radiation dosimetry in fluoroscopy guided interventional radiology procedures. This film comes in large sheets (35.6 cm x 43.2 cm), which can cover the patient's skin in order to study the radiation dose distribution during a clinical procedure. XR-RV3 film is one type of the XR-R films, which is sensitive to wide dose and energy ranges, 0.01 Gy to 30 Gy and 30 kVp to 30 MeV, respectively (Appendix A). The XR-RV3 is a reflective-type film (reflection densitometry) and consists of five layers, including a white opaque polyester layer, yellow transparent polyester layer, adhesive layer, active layer, and undercoat layer (Figure 3.3a). XR-RV3 composes mainly of carbon, oxygen, and hydrogen with an

effective atomic number of about 7.3 (McCabe *et al*., 2011). The active layer consists of a microcrystalline radiation sensitive monomer dispersed in a gelatin matrix. When this layer exposed to ionising radiation, the ionisation radiation causes the polymerisation and forms the polydiacetylene dye. The generation of the dye changes the film colour from orange to green without any chemical processing needed (Figure 3.3b).

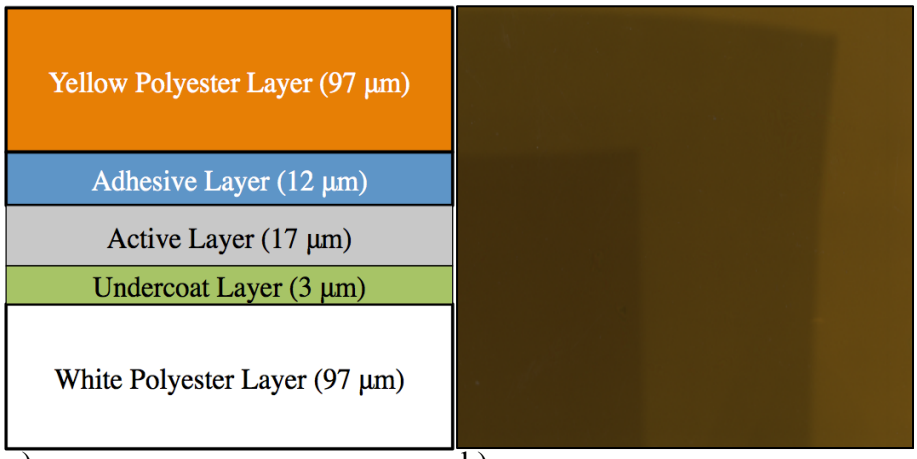

Figure 3.3 a) Schematic of construction of the XR-RV3 layers (Appendix A) and b) XR-RV3 film (yellow transparent polyester layer faced up) shows the ionisation radiation causes the generation of the dye in the active layer and changes the film colour from orange to green.

McCabe *et al.* in their study on characterisation of the XR-RV3 film showed that the response of this film depends on beam energy and film orientation (McCabe *et al*., 2011). Their energy dependence test revealed that for a 200 cGy and a 500 cGy air-kerma exposure when the orange side of the XR-RV3 is irradiated, change of the exposure energy from 60 to 120 kVp increased the film response by 20% and 12% respectively. The XR-RV3 sensitivity rises with white facing orientation 4.0% at 60 kVp to 9.9% at 120 kVp compared to the orange facing orientation. The XR-RV3 has been used widely for evaluation of radiation dose distribution and patient's maximum

skin dose during clinical interventional procedures (Bednarek *et al*., 2011; Tsai *et al*., 2014; Bordier *et al*., 2015).

3.3. Flatbed Scanner and Image Analyser Software

It is recommended to use a flatbed scanner to read the Gafchromic® XR-R films. In this study, the film scanning was performed using an Epson 10000XL flatbed scanner with 48-bit RGB capability. Exposed films were scanned after 24 hours post-exposure to allow for the optical density stabilising (Giles & Murphy, 2002). The exposed films were scanned using reflective mode with scanning resolution of 96 dpi. Scanned images were analysed using Imagej 1.47 software (National Institute of Health, USA).

The scanned image was split into red, green and blue colour channels. The pixel value of the red channel (16-bit: 2^{16}-1= 65535 pixel) was used for image analysis. The pixel value of the region of interest was recorded and converted to optical density (OD) using Eq. 3.1. The mean of red channel of the exposed film (OD_2) is subtracted from mean of red channel of that film before exposure (OD_1), in order to calculate the effect of radiation on optical density of the film (OD_{net}).

Based on calibration curve, the OD_{net} is used to find the amount of absorbed dose by the film (Figure 3.4)

$$OD = log_{10}(\frac{65535}{mean\ pixel\ value}). \quad \text{Eq. 3.1}$$

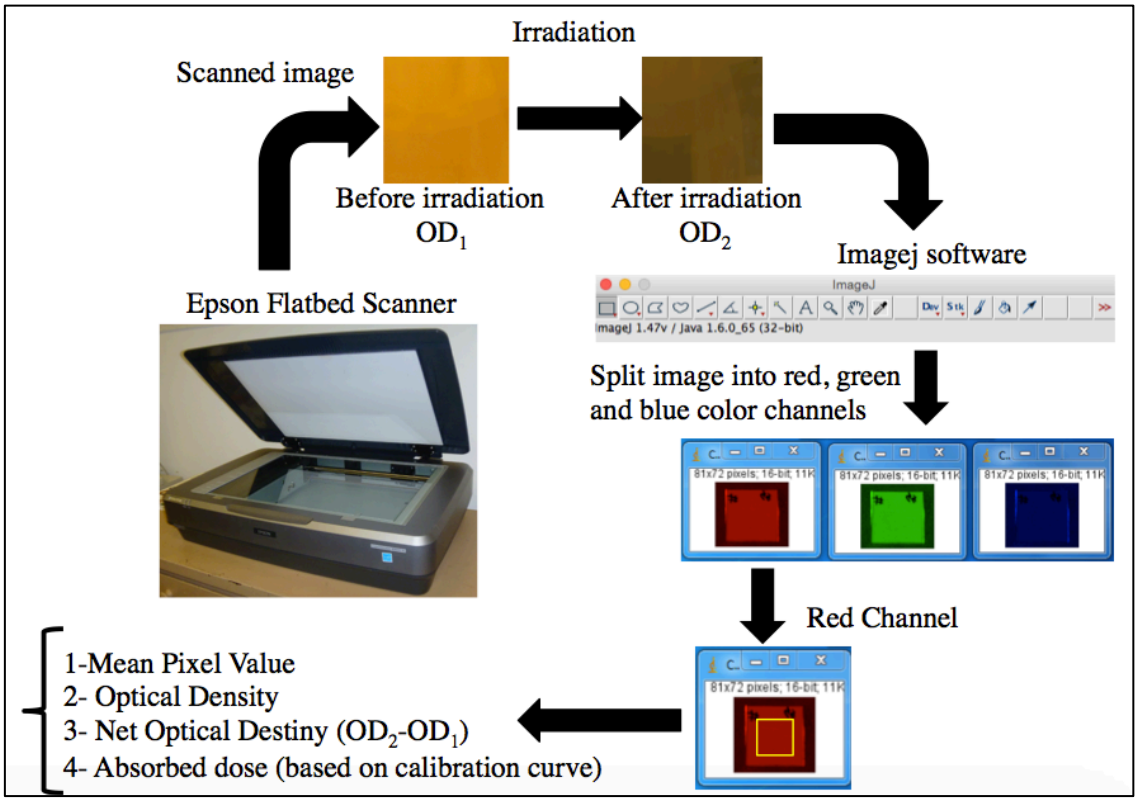

Figure 3.4 Block diagram showing the Gafchromic® XR-RV3 film scanning steps.

3.4. Philips Allura Xper FD20/20® Biplane System

The neuro-interventional procedures were performed using a Philips Allura Xper FD20/20® biplane system (Philips Healthcare, Best, The Netherlands) at the University of Malaya Medical Centre (UMMC). This suite consists of one ceiling mounted x-ray tube and one floor mounted x-ray tube equipped with a 30 x 38 cm^2 dynamic flat panel detector. This machine is equipped with different electronic rectangular field-of-views (FOVs), which change the sensitive image detector area from 15 cm to 48 cm and exposure tube potential varies between 40 and 125 kVp. This machine can generate five frame rate ranges for vascular procedures (0.5fps, 2fps, 3fps, 4fps, and 6fps) and two frame rate ranges for cardiac procedures (15fps and 30fps). The Philips Allura Xper FD20/20® machine can apply different filtrations, 0, 0.2, 0.5, and 1.0 mm copper equivalent, which are specified to different types of exposures. The tube voltage is controlled by an automatic dose rate control (ADRC) system.

The general concept of the ADRC system is to control the x-ray exposure parameters (Table 3.1: orange colour box) during a clinical procedure, within the limits of x-ray system. The control parameters are impacted by the interaction variables (violet colour box), within the clinical system geometry limitations. The outcomes of the exposure parameter changes must meet the regulations from governing societies and standard organisations (Table 3.1).

Table 3.1 Effects of the interaction variables on control parameters and clinical outcomes (adapted from (Gislason-Lee *et al*., 2011)).

Control parameters (units)	**Interaction parameters**	**Clinical/Technical outcomes**
Tube potential (kVp)	Patient thickness	Image quality
Filtration (mmAl)	Contrast medium	Patient dose
Tube current (mA)	Detail thickness	
X-ray pulse duration (ms)	Gantry angle	
Detector dose (kerma)	Grid/air gap	
Frame rate (fps)	Scatter/primary	
	x-ray field size	
	Source-image distance (SID)	
	Under limits of	
Tube/ generator	System geometry	IEC standards
[Power (W) and heat (ºC)]		FDA regulations
		Local philosophy [diagnostic reference levels (DRLs)]

The ADRC system seeks to attain optimal patient's dose and image quality for each EPX (Examination, Patient-type and X-ray operator) individually. Each user selectable patient type (weight and age) has its own predefined estimated patient thickness and the system also can calculate the patient thickness from the prior fluoroscopy run, based on its exposure parameters, added filtration, detector output (digital pixel intensity), and SID. According to the estimated patient thickness, the peak tube voltage and filtration were automatically selected. The peak tube current and x-ray pulse duration were selected based on tube voltage and acquisition or fluoroscopy exposure modes are started (Figure 3.5a).

Next, according to the measured detector output after each frame and based on each EPX require detector output, the ADRC calculates the difference between needed and measured detector outputs and updates the exposure parameters in the next x-ray pulse (Figure 3.5b). A detailed description of the ADRC system and its algorithm for optimising exposure energy, tube current and pulse duration can be found in (Gislason *et al*., 2011).

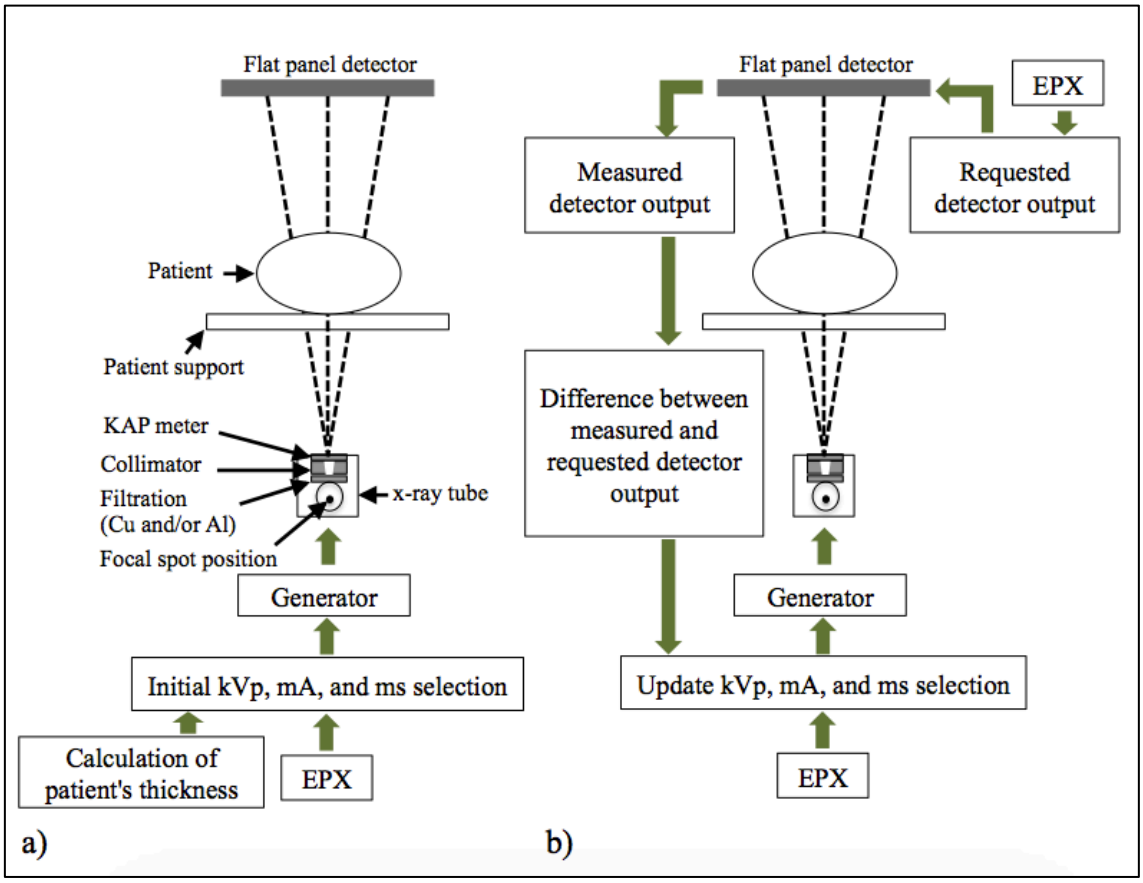

Figure 3.5 Mechanism of ADRC performance to achieve highest image quality with optimum patient's dose by adjusting the (a) initial exposure parameters, which were obtained based on estimated patient's thickness to (b) optimal exposure parameters based on comparing the requested and measured detector output (adapted from (Gislason-Lee *et al*., 2011)).

3.5. Phantoms

3.5.1. Gammex 457 Solid Water®

Gammex 457 Solid Water® is particularly designed to simulate the absorption characteristics of water very closely over a wide-ranging photon energies. Solid Water® is able to achieve calibration within 1% of the real water (Appendix B). Solid Water® phantoms have been used widely by medical physicists for depth dose measurements, relative ionisation calibration, and absolute calibrations for years. The density of the

Solid Water® is 1.04 g.cm^{-3} and comes in 20 × 20 cm^2, 30 × 30 cm^2, and 40 × 40 cm^2 slabs with various slab thicknesses of 0.2 to 6.0 cm.

In this study a set of Solid Water® phantom (30 × 30 cm^2) with various slab thickness (0.2 to 5.0 cm) was utilised.

3.5.2. ATOM® Dosimetry Phantom

An ATOM® female anthropomorphic dosimetry phantom (model 702; CIRS, Norfolk, Va) was used to simulate a patient's body during the experimental exposures. This phantom has a 160 cm tall and 55 kg weight and designed with traditional 2.5 cm thick sections.

The ATOM® anthropomorphic phantoms imitate the human organs with four tissue equivalent materials for bone, soft tissue, brain, and lung. These phantoms have age series from newborn to adult, since the human bone density changes considerably with age. Therefore, for more accurate dose measurement, the bone simulated material in ATOM® phantoms are formulated based on proper bone composition of each age. This phantom provides the possibility of radiation dose measurement using various dosimetry systems, like TLDs (chips, rods, bars, and cubes), MOSFETs, Landauer OSLDs (Micro Dot and nanoDot), and ion chambers and diodes as customised accessories. ATOM® phantoms are constructed of computerised imaging reference systems (CIRS) exclusive tissue equivalent materials made by various resins and polymer based materials. Based on manufacturer report on radiation property of the ATOM® phantom, the linear attenuations of the simulated soft tissue and bone are within 1% of actual attenuation and linear attenuations of the simulated lung is within 3% (Table 3.2) (Appendix C).

Table 3.2 Linear attenuation coefficients (cm^{-1}) for different tissue substitute materials used in the construction of the ATOM® phantom (retrieved from the ATOM® phantom manual, Appendix C).

	Average Soft Tissue		Average Bone Tissue		Average Lung Tissue		Average Brain Tissue	
keV	Reference*	ATOM®	Reference*	ATOM®	Reference*	ATOM®	Reference*	ATOM®
40	0.2679	0.2678	0.7884	0.7887	0.0537	0.0531	0.2791	0.2791
60	0.2087	0.2091	0.4244	0.4242	0.0410	0.0414	0.2135	0.2138
80	0.1871	0.1876	0.3251	03248	0.0365	0.0372	0.1902	0.1907
100	0.1742	0.1748	0.2822	0.2819	0.0339	0.0346	0.1767	0.1772

* Reference: (Snyder *et al*., 1974).

3.6. Energy Dispersive Spectroscopy on the Scanning Electron Microscope

Energy Dispersive x-ray Spectroscopy (EDS) is a chemical microanalysis system. In this system electron bombardment is performed on the predefined region of interest of the Scanning Electron Microscope (SEM) image, which generates characteristics and bremsstrahlung x-rays as a result of inelastic interaction of the electron beams with the sample atoms. More information on electron interaction with matter can be find in chapter 2, section 2.4. An EDS system comprises of several parts, including a radiation detector (made of lithium drifted silicon (Si(Li)) (Jorge, 1968), high purity germanium (HpGe) (Pehl *et al*., 1972), or silicon drift detectors (SDD) (Gatti & Rehak, 1984)), an amplifier, and a digital pulse processor connected to a computer . The EDS can separate emitted x-rays from the specimen based on their energy levels. The elemental composition of the medium is determined based on the fundamental principle that each element has unique peaks on its emitted x-ray spectrum. The EDS system detects and measures the relative abundance of x-rays emitted from a sample after bombarding with high-energy electron versus their energy beams (Ngo, 1999; Hafner, 2006). This information is used to identify the elemental composition of the sample and their relative

proportions (for instance atomic weight%). In this research, the elemental compositions of samples are examined using an electron microscope (Quanta FEG 650; FEI, Hillsboro, OR, USA) at 30 keV electron beam.

3.7. Photon Cross-Section Database, XCOM

Photon cross-sections for a component or mixture can be calculated by summing up the photon cross-sections for all their atomic constituents. This numerical work is complicated and it became problematic by the fact that photon absorption cross-sections and total attenuation coefficients are discontinues at absorption edges. This problem needs to be tackled by additional interpolations for the photon energies above and below all the absorption edges for all the atomic elements. A convenient alternative approach to manual calculation of photon cross-sections, is utilizing computer calculation. XCOM is a web database was developed by Berger & Hubbell in 1999, which provides photon cross-sections for photoelectric, scattering, photoelectric absorption, and pair production (NIST, 1999). This database can be used to calculate total attenuation coefficients of any elements, compounds, and mixture ($Z \leq 100$) for a wide range of photon energy range (1 keV to 100 GeV) with a personal computer (Berger & Hubbell, 1987). The photon cross-sections for various elemental (Henke *et al*., 1982; Plechaty *et al*., 1978) and some compounds and mixtures (Hubbell, 1969; Veigele, 1973) were tabulated in the XCOM database (NIST, 1999).

In this program, the partial and total mass interaction coefficients of components are calculated as a result of the corresponding quantity for constituents cross-sections times the number of target molecules per unit mass. The weighting factor is the fraction of constituents' weights, which for most of the compounds and all mixtures need to be defined by the user.

The XCOM program provides partial photon cross-sections for various photon energies, like incoherent and coherent scatterings, photoelectric absorption, and pair production and also reports total mass attenuation coefficients of the medium ($cm^2.g^{-1}$).

Different studies have studied the accuracy of XCOM software by comparing the linear attenuation coefficients derived from its calculation and those derived from measurement and Monte Carlo simulation. Hill *et al*. in their research reported the linear attenuation coefficients of the solid phantoms and Perspex based on XCOM calculations were 2% and 4% greater than those derived from Monte Carlo simulation. This study showed these disagreements are slightly larger between the XCOM data and measurement findings, up to 3% and 7% for solid phantoms and Perspex, respectively (Hill *et al*., 2008).

Reliability of the XCOM software has been studied for higher photon energies as well. Kaewkhao *et al*., (2010) in their research measured the mass attenuation coefficients of bismuth oxide (Bi_2O_3) and barium oxide (BaO) shielding materials at 662 keV, and compare with the theoretical values calculated by XCOM software. This study showed an average difference of about 5% between experiment and XCOM values (Kaewkhao *et al*., 2010). Tuscharoen *et al*., (2010) reported the total mass attenuation coefficients of various types of barium-borate-flyash ($BaO:B_2O_3$:Flyash) glass shields (with different ratios of BaO, 45-70% of the component weight) based on experimental and XCOM calculation findings at 662 keV. This study showed a good agreement between the experimental and the XCOM values, within relative deviation of 0.03 to 1.42 % (Suparat *et al*., 2011).

3.8. Mass Balance Technique

In this study the physical density of different samples (in chapter 7 and chapter 8) were measured based on the theory of the buoyant force using a mass balance technique (Sartorius Analytical Balance, BA110S, Gottingen, Germany) (Figure 3.6).

In this theory specific gravity (SG) of the fluid or substance is defined as the ratio of the density of the substance to the density of water (density and SG of the 4ºC water is equal to 1 g.cm^{-3}) (Eq. 3.2)

$$SG_{substance} = \frac{Substance\ weight\ in\ air - SG_{Water}}{Substance\ weight\ in\ air - Substance\ weight\ in\ water}. \qquad \text{Eq. 3.2}$$

In this method the substance's weight in the air and inside the water (4 ºC) are measured. The loss of substance's weight is equal to the weight of the water displaced, which based on the water density (1 g.cm^{-3}) is equal to sample's volume. Therefore, the Equation 3.2 shows the density of the substance as well ($\frac{Substance's\ weight\ in\ air}{Substance's\ volume} = \frac{g}{cm^3}$).

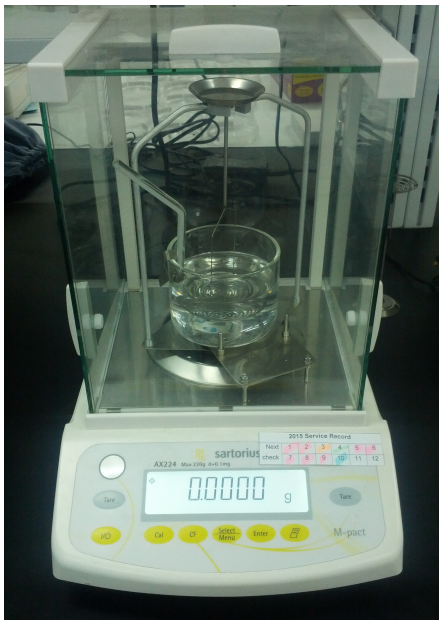

Figure 3.6 Photo of the analytical balance (Sartorius Analytical Balance, BA110S, Gottingen, Germany).

3.9. 3D Printer

The 3D printing system was invented by Charles Hullin in 1986 and has been used in automobile and aerospace industry (Hull, 1986). The 3D printing principle is based on creating a 3D objects through deposition of different types of materials (like powder or polymer based materials) in 2D layers, which offers many advantages, like ability of fabrication of objects with multifaceted internal and external structures, ability to modify the object design and material to meet the costumer's needs, and requires less space in compare to traditional manufacturing. The 3D printing technology has been utilised widely in manufacturing industries and its application in healthcare is progressively growing.

Currently the 3D printing technology plays a growing role in various industries, like jewelry, and fabrication of batteries. The 3D printers have been used widely in medical field as well, like in tissue engineering (Jung *et al*., 2015; Yuan *et al*., 2015; Zhang *et al*., 2015) and bioprinting stem cells (Datar *et al*., 2015; Faulkner-Jones *et al*., 2015; Ouyang *et al*., 2015). Using the patient's imaging data, like computer tomography (CT) and magnetic resonance (MR) images, to generate 3D models of the patient's organs enables physicians to fabricate custom implant and prosthesis (Liacouras *et al*., 2011), anatomical model for training purposes (Waran *et al*., 2012; Gur, 2014; Naftulin *et al*., 2015), anatomical model of the complicated pathologies for treatment or diagnostic purposes (Tam *et al*., 2012), and bioprinting.

Bioprinting is 3D printing based technique, which has been used to produce living organs for transplantations. This technique has been used to fabricate various tissues like bone (De Coppi *et al*., 2007; Comesana *et al*., 2011; Asadi-Eydivand *et al*., 2016), cartilage (Cui *et al*., 2012; Jung *et al*., 2015), and skin (Skardal *et al*., 2012) and production of some functional organs, like kidney, liver, and some other organs is currently being researched (Murphy & Atala, 2014).

In this study a 3D printer (ZPrinter 450®, Z Corporation, Burlington, MA, USA) was utilised to construct an anthropomorphic head phantom, in order to print the human skull based on the CT images of a male patient following a standard head and neck imaging protocol. Assembling of the printed skull and other fabricated head organs, like brain and eyeballs, resulted a full head anthropomorphic phantom, which will be comprehensively explained in chapter 8.

CHAPTER 4: CHARACTERISATION OF THE MO*SKIN* RADIATION DOSIMETER AT KILOVOLTAGE PHOTON ENERGIES

4.1. Introduction

The MO*Skin* detector has been characterised for various factors affecting its response for megavoltage photon beams and has been used for patient dose measurements during radiotherapy procedures. However, the characteristics of this detector in kilovoltage photon beams and low dose ranges have not comprehensively been studied. The purpose of this chapter therefore was to characterise the MO*Skin* detector in the kilovoltage photon energy range, in order to determine its suitability for *in-vivo* entrance skin dose measurements during interventional radiology procedures (research objective 1). In this chapter the MO*Skin* detector responses in terms of changing radiation energy, field size, exposure angle, source to surface distance (SSD), dose rate, and percent depth dose (PDD) under various diagnostic beam qualities were investigated.

4.2. Literature Review

MO*Skin* detector has been characterised in megavoltage photon beam. MO*Skin*'s angular dependency was studied under 6MV photon beam (Kwan *et al*., 2008), which showed a variation of ±2% in MO*Skin* sensitivity over 360º azimuth axis. Comparison of the MO*Skin*, Attic ion chamber, and RADFET detector responses at surface of Solid Water® phantom relative to dose at D_{max} using 10 × 10 cm^2 exposure field of 6 MV, when the exposure angle varied from 0–75º revealed that, MO*Skin* response has very good agreement with the Attic chamber (18.3±0.7% and 16% of the D_{max}, respectively) and RADFET detector showed higher response (35.8 ± 2%), due to RADFET's epoxy encapsulating layer on top of the its sensitive region. MO*Skin* characteristics were studied using ^{192}Ir radioactive source (Kwan *et al*., 2009). This study showed that

MO*Skin* detector has a small angular dependency (<2%), excellent dose linearity (r^2=1) for a dose range of 5 to 200 cGy, and a high reproducibility range (<3%).

Later on, the MO*Skin* detector sensitivity for megavoltage radiation (6MV) was reported, to be 2.63 ± 0.01 $mV.cGy^{-1}$ and this study revealed MO*Skin* sensitivity has very good reproducibility for low dose exposure up to 10 Gy (within 1%) and for higher doses reproducibility its sensitivity varies up to 2%. The MO*Skin* detector showed low dependency to exposure angle, within ±2.5% for the azimuth axis and between −2.5% and +4% for the polar axis (Hardcastle *et al*., 2010).

Qi *et al.* 2011 found that MO*Skin* sensitivity variation is almost independent to exposure SSD (<0.4%) in 6 MV photons. They found that MO*Skin* has considerably low dependency to exposure field size smaller than 20 × 20 cm^2, within 1.0% and its dependency to exposure angle is minimal to be within 2% over 360º. The PDD measurement showed that the MO*Skin* detector response is with a good agreement with ion chamber, within 2.5% for depths up to 15.5 cm and within 3.5% for depths of 16.5 to 19.5 cm (Kwan *et al*., 2008; Qi *et al*., 2011).

Characterisation of the MO*Skin* detector was also performed for diagnostic beam energy. Lian *et al*. in 2011 based on Monte Carlo simulation reported that using 70 μm polyamide film on top of the MOSFET sensor provides considerably better energy response in compared with 20 μm, in the energy range of 15–300 keV. The 70μm polyamide film MO*Skin*'s energy response dropped dramatically in radiation energy lower than 50 keV, which led to a plateau in the energy range of 50–300 keV. The study of percentage depth dose of the MO*Skin* detector was carried out by comparing simulated MO*Skin* response with simulated water response under a 100 kVp, which showed good agreement at shallow depths less than 15 mm, to be within ±3% and beyond 15 mm water depth, the MO*Skin* generally under-responds up to a maximum of 23% at water depth of 60 mm. Similarly for a 150 keV, simulated MO*Skin* showed good

agreement at shallow depths less than 20 mm with simulated water response, to be within ±3% and beyond 20 mm the MO*Skin* under-responds by about 8% (Lian *et al*., 2011).

Attempts to experimentally study the MO*Skin* percentage depth dose has been performed by Lian *et al*. (2013) using 150 keV, benchmarked with the Markus ion-chamber. The measurement showed at depths larger than 80 mm in Solid Water® the MO*Skin* detector under-responds in compared to Markus chamber and the average agreement between them was 3%. However, at depths less than 80 mm MO*Skin* detector over-responds in compared to Markus chamber, with a trade-off uncertainty of ±3 mGy at 20 mm depth (Lian *et al*., 2013).

4.3. Materials and Methods

The MO*Skin* detector calibration and dependency on radiation energy were carried out under RQR standard radiation qualities (IEC 61267 (IEC, 2005)) in free-air-geometry (Fig. 4.1). The free-in-air geometry was achieved by placing the detectors at an elevated platform made of styrofoam. The radiation beams were generated by a Y-TU 160-D02 x-ray machine (COMET AG, Flammat, Switzerland), at the Secondary Standard Dosimetry Laboratory (SSDL) of the Malaysian Nuclear Agency. Table 4.1 shows the parameters of the various RQR standard qualities.

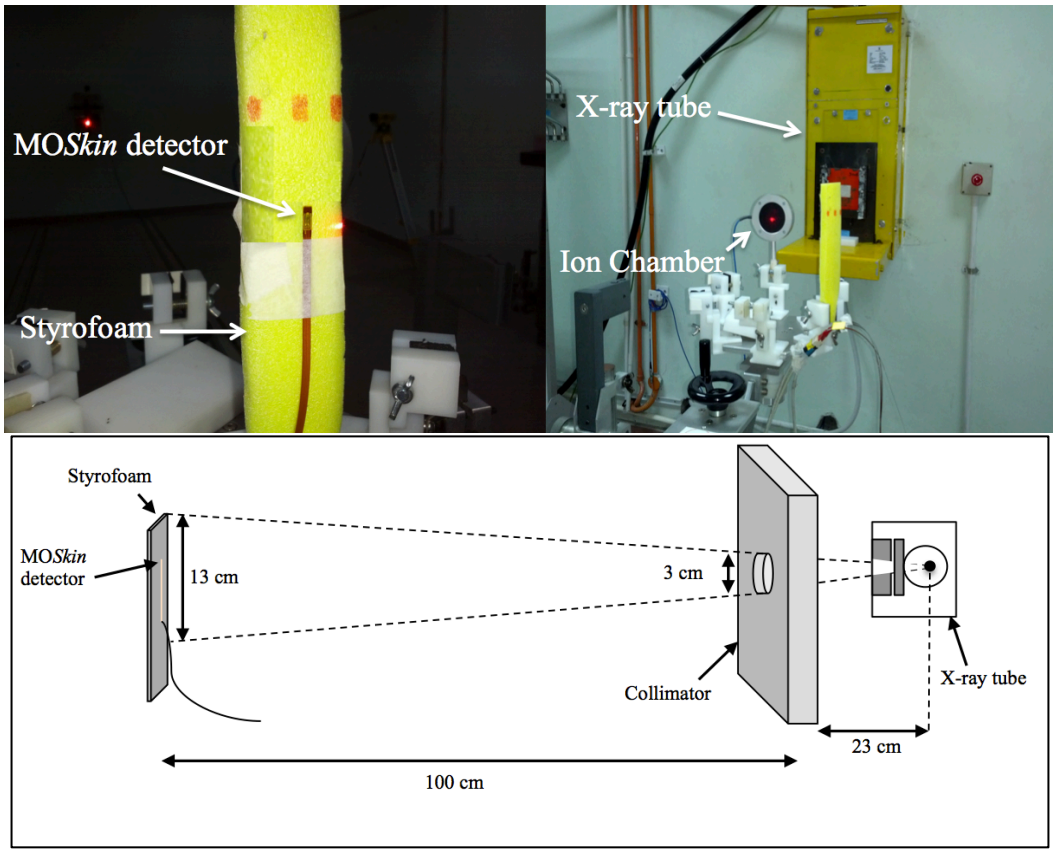

Figure 4.1 Calibration and energy dependence measurements setup under RQR standard radiation beams.

Table 4.1. RQR Standard Radiation Qualities.

Radiation beam quality	Tube potential (kVp)	Effective energy (keV)*	Added filtration (mmAl)	Half Value Layer (mmAl)
RQR3	50	27.0	2.7	1.8
RQR4	60	29.2	2.8	2.1
RQR5	70	31.6	3.1	2.5
RQR6	80	34.0	3.2	3.0
RQR7	90	36.0	3.4	3.4
RQR8	100	38.6	3.7	4.1
RQR9	120	42.7	4.0	5.1

* Effective energies were obtained from the NIST website (NIST, 2010)

The MO*Skin* detector linearity and reproducibility, angular dependency, field size, PDD in Solid Water® phantom, dose rate, frame rate and source to surface distance were studied using a clinical C-arm fluoroscopy unit (Philips Exper Allura FD20/20® x-ray unit, Philips Healthcare, Amsterdam, Netherlands) at the University of Malaya Medical Centre (UMMC). Characterisation procedures under the clinical x-ray unit was carried out using a 30 × 30 × 12 cm^3 water equivalent plastic phantom (Gammex 457, Gammex, Middleton, WI, USA) and the x-ray tube was positioned at gantry angle of 180º, perpendicular to phantom surface (Figure 4.2a). The detector was characterised for an 80 kVp photon beam (effective energy 42.76 keV) using exposure acquisition mode (3fps). Imaging field of view (FOV) or magnification was fixed at 48 cm, flat panel detector was placed at 120 cm from the tube (SID) and field size of 10 × 10 cm^2 was used. This setup is henceforth called the "standard setup" (Figure 4.2a). The MO*Skin* detector was placed in face-up orientation toward the x-ray tube unless otherwise stated. The characterisation procedures under RQR standard radiation qualities were benchmarked against a 30 cm^3 parallel plane ionisation chamber (model 233612, PTW, Freiburg, Germany), while measurements under the clinical x-ray unit were benchmarked against a 0.055 cm^3 Markus parallel plane ion chamber (model 23343, PTW, Freiburg, Germany). All measurements were repeated three times and the mean $\pm$ 1 standard deviation (1 S.D.) of the results were reported. Effective energies were obtained from NIST website.

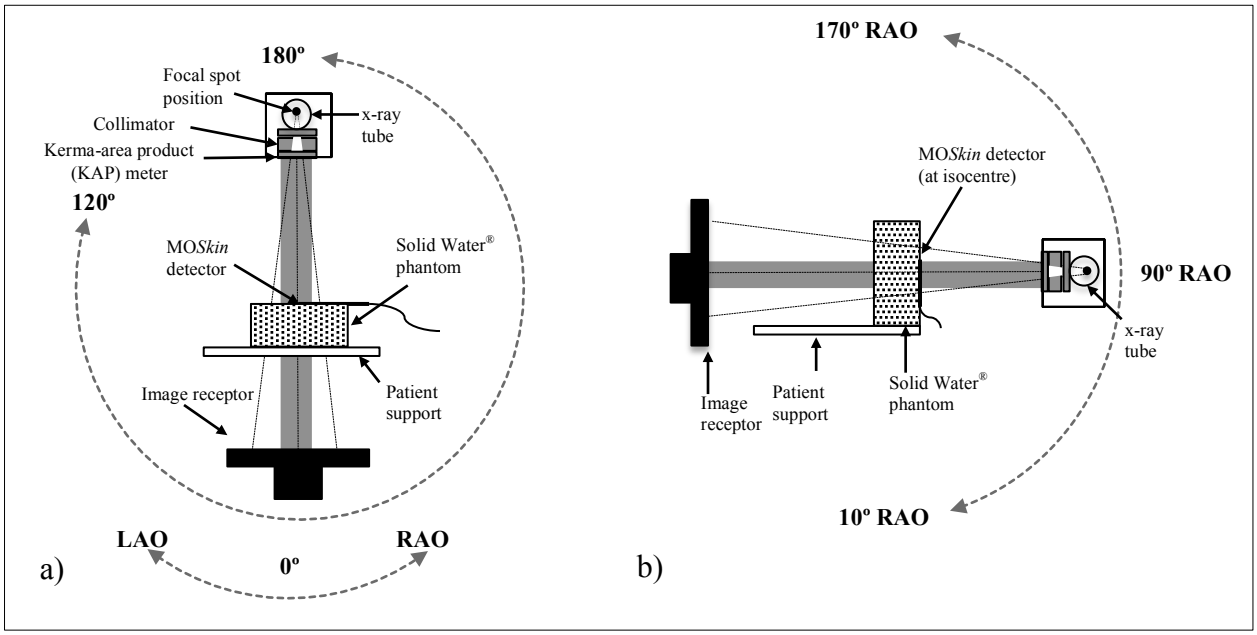

Figure 4.2 Characterisation setups with C-arm x-ray tube fluoroscopy unit, a) "standard setup and b) measurement setup for angular dependency test.

Two types of uncertainties in the analysis of the MO*Skin* characteristics results. The MO*Skin* reader shows the threshold voltage change with uncertainty of ± 1 mV, and immediate reading of the detector after the end of irradiation can generate voltage creep-up up to ± 4 mV (Kwan *et al*., 2008). The creep-up voltage depends on the time between successive readouts, which peaks 10 sec following the end of irradiation and this uncertainty can be reduced with a 1-minute post-irradiation wait time (Ramani *et al*., 1997).

The significance of these uncertainties is dependent on the total dose delivery to the MO*Skin* detector and it is negligible during high dose delivery, when the threshold voltage change is large. In this research, the dose delivered to the detector was in the lower range; therefore these uncertainties should be taken into account in our results. Furthermore, a 1-minute post-irradiation wait time was instituted. A study on temperature dependence of the MOSFET detector reported the threshold voltage variation of 50 mV for temperature change over 20 to 40 °C (Cheung *et al*., 2004).

To avoid the temperature effect on MO*Skin* detector reading, the MO*Skin* detector was placed on styrofoam or Solid Water® phantom inside of the measurement room for about 5 minutes before starting the measurement for temperature equilibrium. At the same time, the ambient temperature was continuously monitored.

4.3.1. Calibration

The MO*Skin* detector was calibrated under RQR7 beam quality (effective energy 36.1 keV) and exposure fixed at 140 mAs. The detector was placed on a styrofoam board at SSD of 100 cm and field size of 13 cm diameter. The PTW ion chamber measurements were corrected for temperature, pressure and energy and reproducibility of the PTW detector was measured to better than 99%.

4.3.2. Energy Dependence Measurement

Semiconductor detectors are known to be energy-dependent, particularly in the kV beam energy range. The high atomic number (Z) of the detector sensitive volume (silicon oxide, $Z \approx 14$) is expected to over-respond at low kV energies due to photoelectric absorption effect. This study was carried out to investigate the magnitude of the energy dependence of the MO*Skin* detector for the beam energy range commonly used in diagnostic radiological procedures. The MO*Skin* energy dependency was studied for the beam energy range of RQR3 to RQR9 (effective energy 27.0 to 42.7 keV). The exposure was fixed at 140 mAs. The MO*Skin* detector was placed at SSD of 100 cm and field size of 13 cm diameter was used.

4.3.3. Dose Linearity and Reproducibility Measurements

Automatic Dose Rate Control (ADRC) was used to control the clinical x-ray tube output. ADRC controls the light output of the image receptor by adjusting kVp and/or mA of the x-ray tube and this adjustment follows one of the pre-programmed kVp-mA curves (Dendy & Heaton, 2011). The small size and design of the MO*Skin* detector does

not alter the ADRC parameters when it is in the beam and exposure parameters remain constant. In this study MO*Skin* detector was set up as per "standard setup" and the sensitivity of the MO*Skin* detector was studied for the dose range of 2 cGy to 213 cGy. The MO*Skin*'s response was benchmarked against the Markus chamber. Any deviation in exposure time and/ or mAs were corrected based on exposure parameters recorded from the console (mAs, number of images, and KAP). Reproducibility of the MO*Skin* detector was assessed based on the mean of the standard deviations for three sets of measurements.

4.3.4. Field Size Dependence Measurement

Field size dependency is an important factor for point dose recording during interventional radiology procedures since multiple field sizes are often used within a treatment procedure. ADRC system adjusts the tube output to maintain the image brightness constant for different exposure field sizes. As the exposure field size decreases, the tube current increases and subsequently the exposure dose increases. The MO*Skin* was set up as per "standard setup" at SSD of 70 cm with selected field sizes from 5 × 5 to 20 × 20 cm^2.

4.3.5. Depth Dose Measurement

MO*Skin* and Markus detectors were initially set up as per "standard setup" followed by placement at different depths in a phantom. For all depth dose measurements, the detectors were placed along the beam central axis separately to minimise the uncertainty caused by the detector positioning. Depth dose measurement was tested for 0 to 35 mm depth from the surface of the Solid Water® phantom.

4.3.6. Source to Surface Distance Dependence

The MO*Skin* detector was setup as per " standard setup". The MO*Skin* detector was placed at SSD of 90 cm with exposure field size of 10 × 10 cm^2 then by moving the couch towards the x-ray tube; detector response at different distances (70 to 90 cm) was studied. MO*Skin* detector dose rate dependence was also evaluated in this section.

4.3.7. Frame Rate Dependence

The Philips Allura Xper FD20/20® system provides two modes of frame rate for angiography procedures, i.e. cardiac and vascular modes. The vascular application allows operators to select acquisition exposures with frame rates of 2, 3, 4 and 6 fps while the frame rates of 15 and 30 fps are for cardiac application. In this study, MO*Skin* detector was setup as per "standard setup" and both application types were used to study the dependence of the MO*Skin* detector to exposure frame rate. The exposure parameters were recorded from the console, kV, mA, ms and filter. The effective energies (keVs) were calculated based on measured HVLs using an Unfors detector (Unfors Raysafe AB, Billdal, Sweden).

4.3.8. Angular Dependence Measurement

The C-arm x-ray tube in head-end position can rotate from 120º Left Anterior Oblique (LAO) to 180º Right Anterior Oblique (RAO) and it cannot cover the entire range (Figure 4.2a). Due to this limitation, the Solid Water® phantom was placed at the edge of the patient support couch (Figure 4.2b) at SSD of 81 cm (isocentre of rotation). The MO*Skin* detector was placed in the centre of the surface of the Solid Water® at the central axis.

The C-arm x-ray tube was rotated from 30º RAO to 150º RAO with 20º intervals and the angular response of the MO*Skin* detector was assessed for face-up and face-down orientations. Other exposure parameters followed the "standard setup".

4.4. Results and Discussion

4.4.1. Detector Calibration

The temperature and pressure correction factors were applied to the PTW ion chamber responses and the readings were used to obtain the sensitivity of the MO*Skin* detector.

The threshold voltage change, ΔV_{th} is proportional to the irradiated dose. The detector sensitivity is defined as (Eq. 4.1)

$$\text{Sensitivity} = \frac{\Delta V_{th}\,(\text{mV})}{\text{Dose}\,(\text{cGy})}. \qquad \text{Eq. 4.1}$$

The sensitivity of the MO*Skin* detector for RQR7 beam quality (effective energy 36.1 keV) photon beam was measured to be 11.56 ± 0.36 mV cGy^{-1}. Previous research reported that the sensitivity of the MO*Skin* detector for 150 kVp x-ray beam (effective energy 64.8 keV) is about 6.70 mV cGy^{-1}, which was measured using EBT 2 film (Lian *et al*., 2013). The sensitivity of MO*Skin* detector in megavoltage beam energy was 2.63 ± 0.01 mV cGy^{-1} (Hardcastle *et al*., 2010). The higher sensitivity measured at lower beam energy is due to the increasing dominance of photoelectric absorption and consequently increasing response of the MO*Skin* detector at low energy. Lifetime of MO*Skin* detector can be calculated by knowing the initial voltage of the MO*Skin* detector (~10V), the sensitivity and its maximum threshold voltage (~24V). When used under diagnostic beam energy, the detector lifetime is approximately equivalent to 12 Gy of radiation exposure.

4.4.2. Energy Dependence

Figure 4.3 shows the MO*Skin* detector's response, normalised to RQR7 beam quality. As expected, the MO*Skin* detector showed enhanced response at lower beam energies. The detector over-responded by a factor of 1.15 at 50 kVp (effective beam energy 27.0 keV). At 120 kVp (effective beam energy 42.7 keV), the detector under-responded by a

factor 0.86. However, for the tube potentials that are commonly used in interventional radiology procedures (70 to 100 kVp), the detector response varies within ± 5%. The ratio of mass energy absorption coefficient of silicon (Si) to air was defined as (Eq. 4.2)

$$\text{Ratio of mass energy absorption coefficient} = \frac{(\frac{\mu_{en}}{\rho})\text{Si}}{(\frac{\mu_{en}}{\rho})\text{air}}, \qquad \text{Eq. 4.2}$$

where $\left(\frac{\mu_{en}}{\rho}\right)_{\text{Si}}$ and $\left(\frac{\mu_{en}}{\rho}\right)_{\text{air}}$ are mass energy absorption coefficients of Si and air respectively. The measured ratio was normalised to 1 at 36.1 keV. As Figure 4.3 illustrates, the change of the MO*Skin* detector's sensitivity for different effective beam energies shows the same behavior with the ratio of mass energy absorption coefficient of Si to air taken for effective photon energy of the x-ray spectra. This comparison does not take into account the change of recombination of electron-hole pairs in the gate of the MOSFET with decreasing photon energy (Kron *et al*., 1998). The ratio of mass energy absorption coefficient of the Si to air has the same trend with the ratio of Si to water.

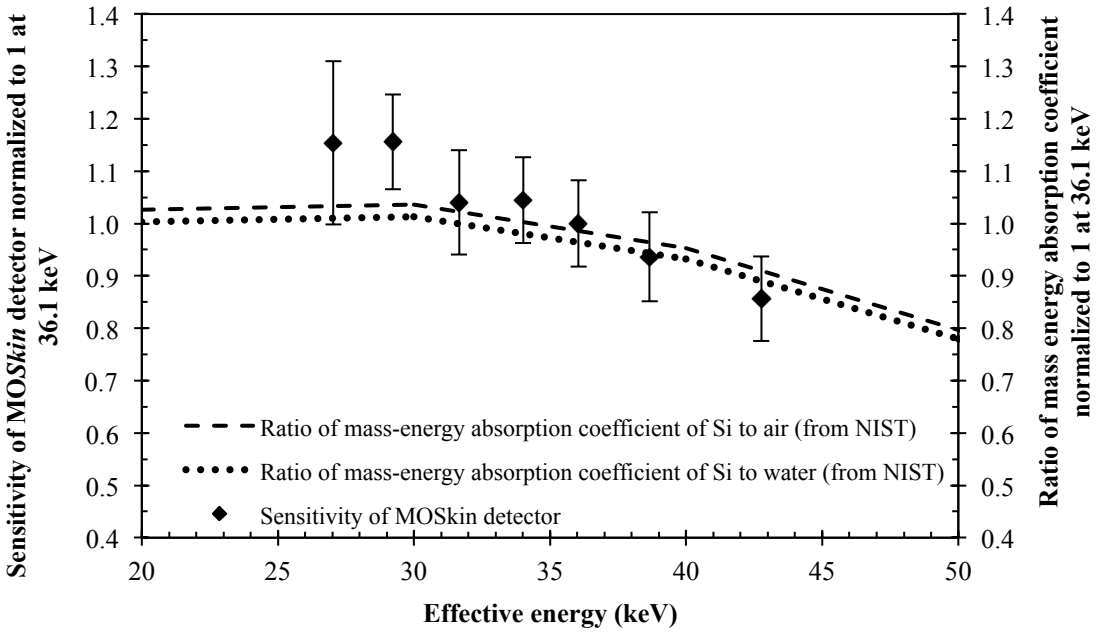

Figure 4.3. Energy dependence of the MO*Skin* detector for diagnostic energy range, under RQR standard beam qualities. The average standard deviation of three measurements is presented.

4.4.3. Dose Linearity and Reproducibility

The MO*Skin* detector showed linear response with the amount of delivered dose (2-213 cGy) measured by Markus ion chamber, over 0.99 (Figure 4.4). The reproducibility of the MO*Skin* measurements was found to be better than 94%.

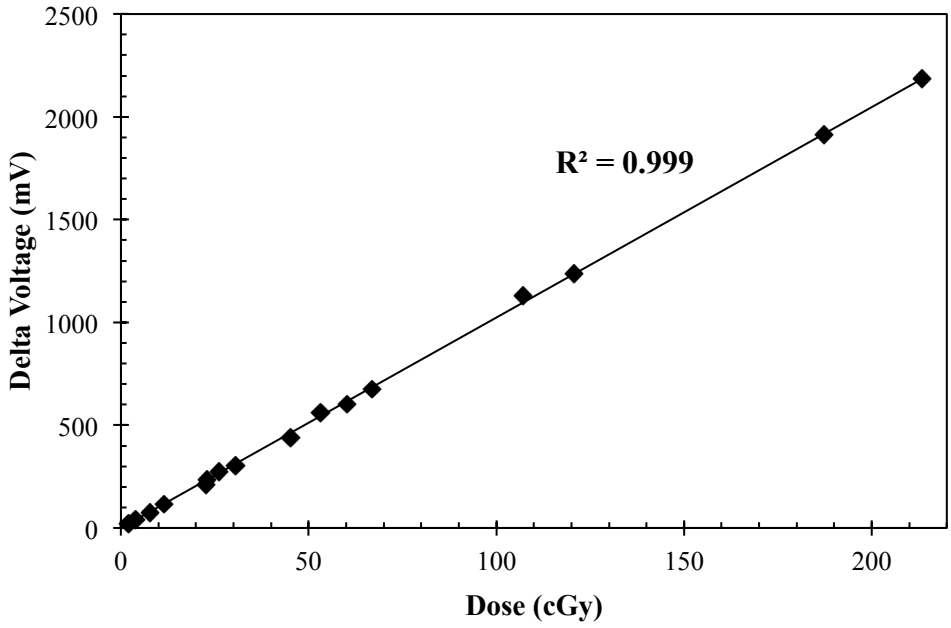

Figure 4.4. Linearity of the MO*Skin* detector benchmarked against the Markus ion chamber. Average standard deviation of this measurement was ± 2 mV.

4.4.4. Field Size Dependence

The ADRC controls the brightness of image for different exposure field sizes by adaptation of the mAs. Smaller exposure field size has higher beam exposure (mAs). For this experiment, the tube potential remained constant throughout the measurement at 80 kVp (effective beam energy 42.76 keV) and beam exposure changed from 61 to 8 mAs for 5 × 5 to 20 × 20 cm^2 exposure field size respectively. Figure 4.5 illustrates that the MO*Skin* detector is independent of field size variation (within ± 1%).

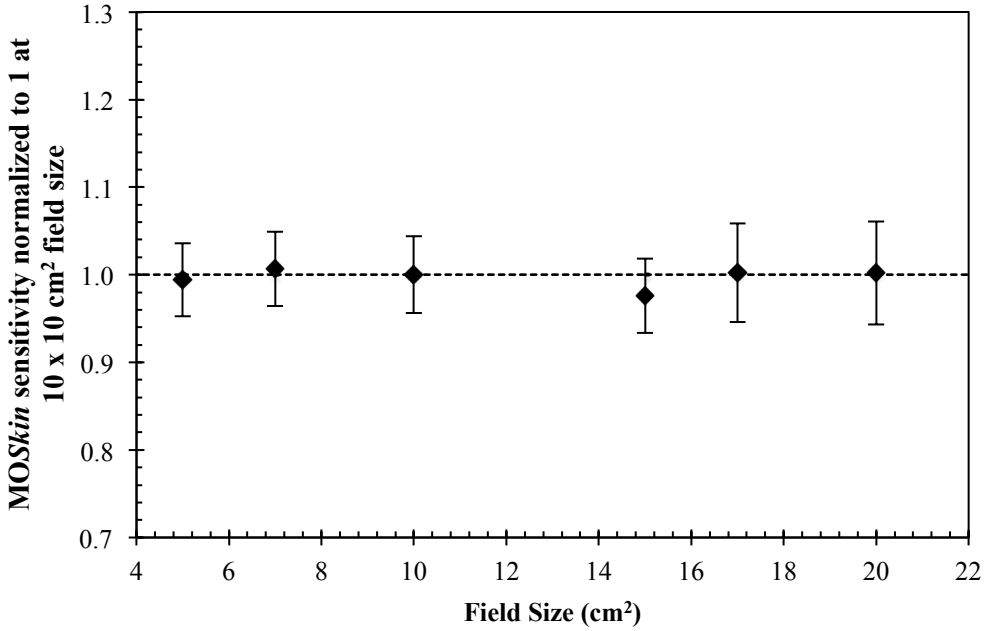

Figure 4.5. The field size effects on detector response placed on surface of the Solid Water® phantom. All the readings are normalized to field size of 10 × 10 cm^2.

4.4.5. Depth Dose Data

The percentage depth dose response of the MO*Skin* detector was tested previously, which showed good agreement with the Markus ion chamber under a 150 kVp (effective energy 64.87 keV). This study reported that, for depths of less than 80 mm, the MO*Skin* detector showed over-response compared with the Markus chamber (Lian *et al*., 2013). Figure 4.6 shows the percentage depth dose curves for MO*Skin* and Markus ion chamber. The detector's responses were normalised to its response at the surface of the Solid Water® phantom. MO*Skin* detector appears to be in good agreement with the Markus chamber, within ± 3%. The largest deviation between the MO*Skin* and Markus detectors' responses was 4% at 2 mm. These results are in good agreement with earlier study findings, while the MO*Skin* detector for this study was calibrated and measured for lower effective photon energy of 42.76 keV.

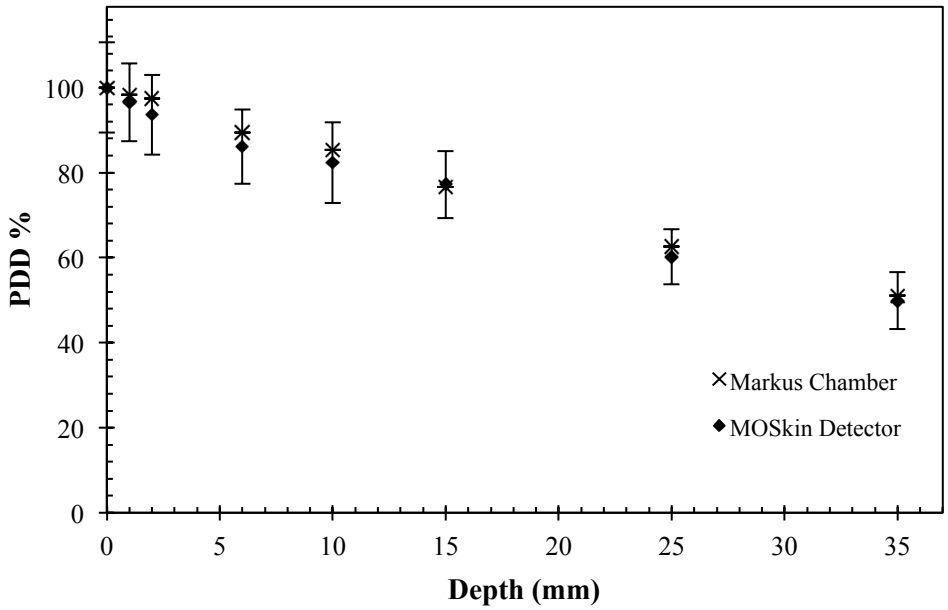

Figure 4.6. Depth dose in Solid Water® for FSD of 10 × 10 cm^2. All the readings are normalised to the surface dose (100%).

4.4.6. Source to Surface Distance Dependence

Figure 4.7 shows the dose measured by MO*Skin* and the Markus chamber corrected for inverse square law. MO*Skin* showed good agreement with the Markus chamber measurements (± 1%). The error bars increased with increasing distance due to lower dose delivery to the detector, consequently effects of reader and voltage creep-up uncertainties become noticeable. The SSD parameter is an important feature for interventional radiology dosimetry, because x-ray tubes are continuously rotating around the patient during interventional radiology procedures. Depending on the location of the patient's body, the x-ray tube is placed at different distances from the body surface. FDA has expressed concerns about SSD in fluoroscopic procedures and has suggested using SSD of 38 cm as a threshold for stationary fluoroscopes and 30 cm for mobile fluoroscopy units (Haynes *et al*., 2013). Figure 4.7 also shows the relative response of the MO*Skin* and Markus detectors, normalised to their ratio at 1.2 $mGy.s^{-1}$

dose rate. MO*Skin* detector shows very low dependency to exposure dose rate (less than 1%).

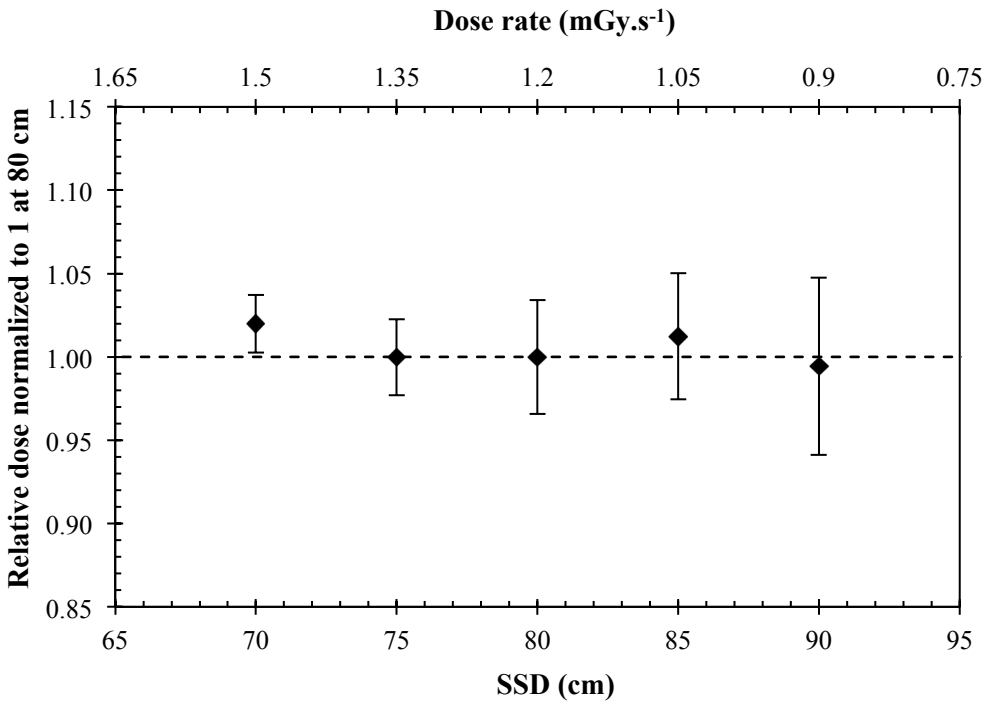

Figure 4.7. Source-to-surface distance and dose rate dependence of the MO*Skin* detector for a 80 kVp x-ray beam with exposure field size of 10 × 10 cm^2.

4.4.7. Frame Rate Dependence

Table 4.2 shows the different frame rates available on the Philips Allura Xper FD20/20® system, group under cardiac and vascular applications. Note that switching from the high frame rates to the low frame rates, the system automatically adjusted the tube potential (filtration) and dose rate. Figure 4.8 shows that MO*Skin* detector has low dependence on frame rate and dose rate variation (within ± 3%). This variation is within the uncertainty due to energy dependence of MO*Skin* detector.

Table 4.1. Effective energy and dose rate value for different frame rates of cardio and vascular applications, controlled by ADRC system.

Application types	Frame rate (fps)	Tube potential (kVp)	Added filtration (mm)	HVL (mmAl)	Effective energy * (keV)	Dose rate ($mGy.s^{-1}$)
Vascular	2	83.50	0.1 Cu+1.0 Al	5.07	42.54	1.68
	3	83.48	0.1 Cu+1.0 Al	5.09	42.61	1.99
	4	83.45	0.1 Cu+1.0 Al	5.07	42.54	2.53
	6	78.64	0	3.22	34.84	3.68
Cardiac	15	70.84	0	2.57	31.55	0.58
	30	70.93	0	2.58	31.60	1.19

* Effective energies were obtained from NIST website (NIST, 2010)

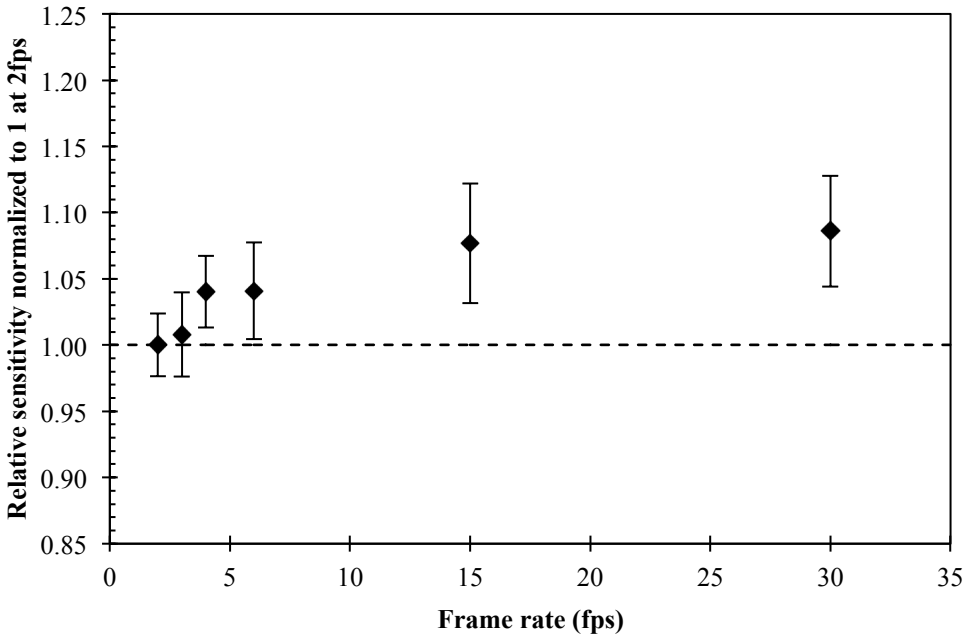

Figure 4.8. MO*Skin* detector frame rate and dose rate dependence of vascular and cardiac applications.

4.4.8. Angular Dependence

The angular dependence of the MO*Skin* detector is presented in Figure 4.9. The variation in the readings for the azimuth axis was within ± 5%. The lowest drop in sensitivity happened in -60º face-up and maximum sensitivity was obtained for 0º face-down. The MO*Skin* detector has different WED in face-down and face-up orientation (inherent anisotropy) on the surface of the phantom. This detector has a thicker build-up layer due to the silicon substrate in case of face-down orientation (see Figure 2.7a in chapter 2), which produces more secondary electrons and subsequently causes dose enhancement at sensitive volume of the MO*Skin*. Hence, the MO*Skin* detector shows higher sensitivity in a face-down orientation relative to a face-up orientation. As Figure 4.9 shows, the MO*Skin* detector's sensitivity decreases with increasing exposure angle. This change in the MO*Skin* detector's sensitivity is due to the intrinsic angular dependence of MO*Skin* and the effect of backscatter radiation. Published reports about

angular dependency of the MO*Skin* detector for 6 MV x-ray field reported that this detector has very low intrinsic dependency on exposure angle (Kwan *et al*., 2008; Qi *et al*., 2011) and the minimum angular dependency for this detector was measured for dual MO*Skin* within ± 2.5% in the azimuth axis under charge particle equilibrium condition (Hardcastle *et al*., 2010).

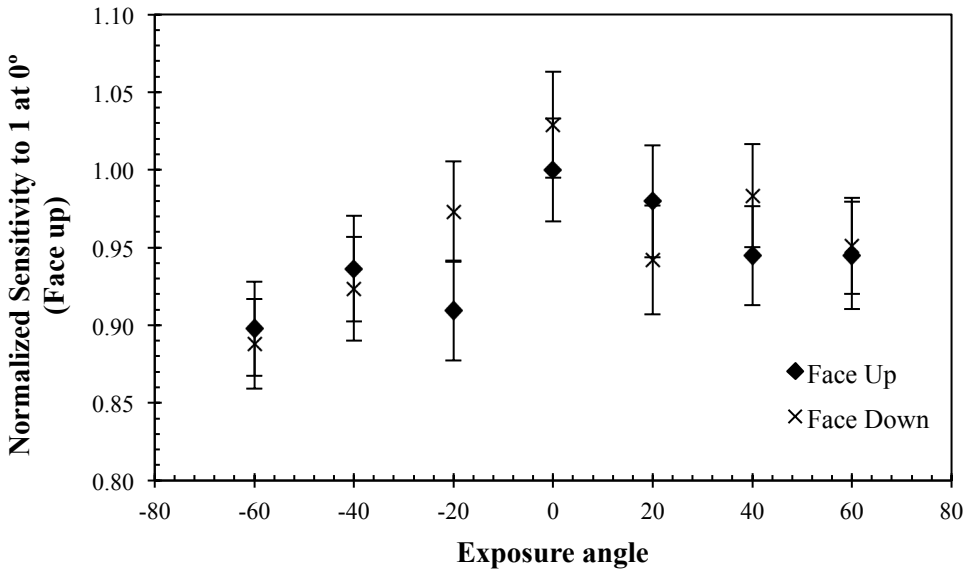

Figure 4.9. The azimuth angular dependence of the MO*Skin* detector. The MO*Skin* response was normalised to the 0° value in face-up orientation.

4.5. Chapter Summary

In this chapter, the MO*Skin* detector was characterised under diagnostic beam energies in attempt to address research objective 1. The dose linearity, reproducibility, depth dose measurements were performed. The detector's response with variation of beam energy, field size, source-surface distance, frame rate, and beam incidence angles were also investigated. This chapter demonstrated that the MO*Skin* detector is suitable for monitoring skin dose during interventional radiology procedures, taking into accounts the various uncertainties and limitation of the detector. Skin dose is an important issue for patient radiation safety during interventional radiology procedures, MO*Skin* detector with WED equal to 0.07 mm, small physical size and high spatial

resolution for depth dose measurement is a suitable detector for *in-vivo* skin dose measurement.

The limitation of this system is that MO*Skin* as a point dosimetry system may not be placed at the location where the skin experiences the most intense radiation dose. Hence, they may underestimate the MSD during interventional radiology procedures. For this purpose, a 2-dimensional dosimeter such as film would still provide the best solution. Compared to other commercially available dose tracking system, which predicts 2D dose distribution of patient via parameters from the fluoroscopic machine, this system does not provide 2D dose distribution information. Nevertheless, this system is a real-time dose tracking system using actual direct dose measurement. Similar to other dose tracking systems, this system also enables interventional radiologists to balance the expected clinical benefits and radiation risks of performing a procedure.

Using multiple MO*Skin* detectors simultaneously to measure dose at selected region of interest or radiosensitive organs such as eye lens would still be useful in providing insights to the radiation dose received by these organs.

A new application for MO*Skin* as a real-time dosimetry system in measurement of radiation dose received by the patient's eye lens during neuro-interventional procedures will be considered in the following chapter.

CHAPTER 5: REAL-TIME PATIENT'S EYE LENS DOSE MONITORING DURING CEREBRAL ANGIOGRAPHY PROCEDURES

5.1. Introduction

Long radiation exposure during complicated fluoroscopy guided interventional radiology procedures may expose patients to tissue reactions. Skin injuries are the most common clinical effects (Wagner *et al*., 1999; Mooney *et al*., 2000), while lens opacity and cataract formation are the main delayed ocular complications and usually appear after 10-20 years unlike skin reactions, which are visible after about 2 weeks.

The purpose of this chapter is to investigate research objective 2 in order to demonstrate a new real-time dose monitoring system for determining patient's eye lens dose during neuro-interventional procedures, and research objective 3, to evaluate correlations of the patient's eye lens dose with dose metric parameters, like KAP, FT, and AK of the frontal (AK_F) and the lateral tube (AK_L).

5.2. Literature Review

Since the radiation dose received by the human organ/tissue is not directly measureable during a clinical procedure, the International Commission on Radiation Units and Measurements (ICRU) in 1990 defined a set of personal dose equivalents, Hp(d), in order to conservative estimate the equivalent dose received by different human organs/tissues. The equivalent dose quantity was described earlier in chapter 2, section 2.5.2. The personal dose equivalent was defined based on point dose determined in ICRU-sphere soft tissue equivalent phantom (with a 30 cm diameter and a density of 1 $g.cm^{-3}$) at a defined depth of d. For lens of the eye and skin, depths of 3 mm (Hp(3)) and 0.07 mm (Hp(0.07)) are employed, respectively (ICRU, 1993). The eye lens dose measurement requires a calibrated detector at 3 mm water equivalent depth. In the absence of this detector, ICRP in 2007 states that a calibrated detector for skin dose

measurement (Hp(0.07)) can be also used to record the radiation dose received by the eye lens (ICRP, 2007).

One of the earliest studies on evaluation of patient's eye lens dose during neuro-interventional procedures was performed on 5 patients who underwent intra-cerebral arteriovenous malformations (AVMs) procedure (Berthelsen & Cederblad, 1991). In this study thermoluminescent dosimeters (TLDs) were used to measure the absorbed doses in the different points of the skin and eyes of the patients. This study reported eye doses of 22 to 139 mGy, which were considerably lower than assumed threshold dose for lens opacities at that time (over 2000 mGy). Later in 1998, evaluation of patient's eye lens dose was considered for patients who underwent diagnostic and treatment of the lachrymal drainage system (Meriçı *et al*., 1998). In this study the diagnostic procedures were performed using frontal tube and treatment procedures were performed using frontal and lateral tubes. For this reason, there was no significant difference between patients' left and right eyes during diagnostic procedures; however, for treatment procedures the untreated eyes received considerably higher doses than treated eyes, due to its closer proximity to the lateral tube. This study reported that the average of patients' eye lens doses received during diagnostic and treatment procedures were 1.1 mGy (0.39-2 mGy) and 38 mGy (14-66 mGy), respectively.

Effect of the lateral tube on considerable difference in radiation dose level at patient's eyes was also reported for 10 patients who underwent fluoroscopically guided transluminal balloon dilation as well (Ilgit *et al*., 2000). This study reported the average of the radiation doses at untreated eyes was eight fold higher than average of the radiation doses received at treated eyes (38.5 mGy and 4.6 mGy, respectively). A study on 30 patients having undergone cerebral embolization reported the average patients' right eye doses was 60 mGy with maximum dose of 500 mGy, which were considered lower than threshold for detectable opacity formation (1000 or 2000 mGy (Wagner &

Archer, 1998)) at that time (Theodorakou & Horrocks, 2003). Moritake *et al*. studied the radiation dose distribution over the patient's head during 28 therapeutic neuro-interventional procedures (Moritake *et al*., 2008). This study showed that patients' right eyes received higher dose than left eyes, 380 ± 593 mGy (7–2079 mGy) and 79 ± 173 mGy (5–913 mGy), respectively because the lateral x-ray tube was placed on the right side of the patient during examinations and right eye may exceed the threshold dose of eye lens opacity formation (500- 2000 mGy) suggested by the ICRP in 2007 (ICRP, 2007). Study on patient's eye lens dose during neuro-interventional procedures, including diagnostic, coiling, and embolization, revealed that the average doses to the patients' eye lenses (left eye) were 7.8 mGy (diagnostic), 51 mGy (coiling), and 71 mGy (embolization), which were considerably higher than radiation doses recorded at patients' right eyes. The maximum eye lens dose of 515 mSv was recorded for a coiling procedure (Sandborg *et al*., 2010). A summary of all these studies is given in Table 5.2.

5.3. Material and Methods

5.3.1. Patients

The real-time monitoring of eye lens dose was carried out on 35 patients, 24 female patients (45 ±16.9 years) and 11 male patients (age 46 ±16.8 years), comprising 19 diagnostic angiographies, 8 treatments of cerebral aneurysms, and 8 embolizations of AVMs. The same interventional radiologist and radiography team performed the neuro-interventional procedures from March 2013 to March 2014.

5.3.2. X-ray Equipment

The neuro-interventional procedures were performed using the Philips Allura Xper FD20/20® biplane system (Philips Healthcare, Best, The Netherlands) at the University of Malaya Medical Centre (UMMC). The specification of the Philips Allura Xper FD20/20® biplane system can be found in Chapter 3, section 3.4.

5.3.3. Data Acquisition

For all the neuro-interventional procedures, the lateral x-ray tube was positioned on the left side of the patients' heads throughout the treatments. According to a survey on routine exposure parameters during 53 neuro-interventional procedures, which will be extensively presented in chapter 6, subsection 6.4.5, in 73.7% of the projection times, the frontal tube projections were acquired in the posterior-anterior direction (10º RAO-10º LAO) and in 93% of the time the lateral tube direction was changed from 70º RAO to 90º RAO. Therefore, the lenses of the left eyes were constantly exposed to the primary x-ray beam from the lateral x-ray tube. The difference between radiation dose received at left and right eyes during cerebral angiography procedures was studied in a pilot study on two patients, which revealed that radiation dose delivered to the left eye region is significantly higher (~5 times) than the dose delivered to the right eye. For this reason, in this study we focused on the measurement of the dose delivered to patients' left eye. The study of the patients' eye lens dose was implemented using MO*Skin* detectors. The MO*Skin* detector radiation characteristics have been well documented in chapter 4. The patients were asked to keep their eyes closed during the treatment procedure. Two MO*Skin* detectors were positioned on the patient's left outer canthus (LOC) and left eyelid (LE) (Figure 5.1a). This detector is not visible on the displayed image and does not interfere with the treatment procedure (Figure 5.1b). The MO*Skin* detectors were placed on the patient's body for at least 5 minutes to allow for the detectors to equilibrate with the patient's body temperature before commencing the measurement. MO*Skin* dosimetry system equipped with acquisition laptop using FETch software was placed in front of the interventional radiologist and the radiographer during treatment procedures (Figure 5.2). Exposure parameters were recorded from the console. Measured doses were compared with exposure parameters such as FT, KAP, AK_F and AK_L.

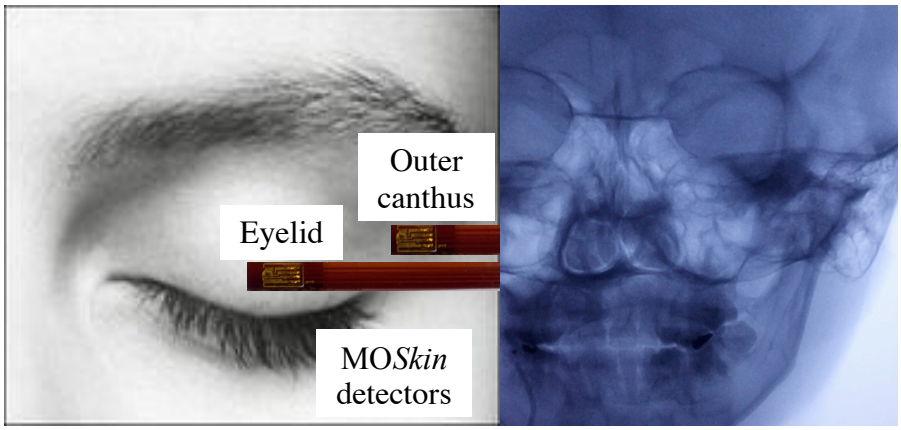

a) b)

Figure 5.1. (a) The MO*Skin* detectors were positioned on the left eyelid and left outer canthus regions during neuro-interventional procedures. (b) This detector is almost invisible on the displayed image.

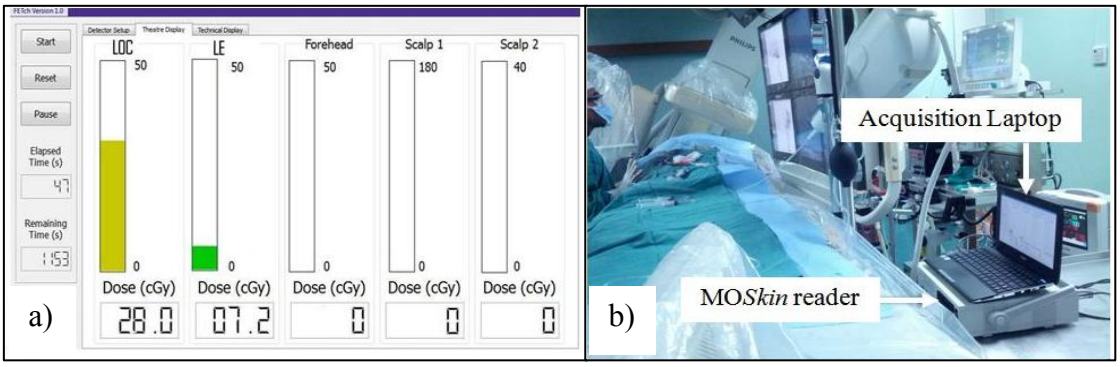

Figure 5.2. (a) FETch display showing the accumulated dose values in column bar charts. (b) MO*Skin* dosimetry system was placed at treatment room and accumulated dose values were displayed using the FETch software in front of the interventional radiologist and the radiographer during treatment procedures.

5.3.4. Statistical Analysis

Regression correlation tests were carried out to determine the relationships between the MO*Skin* response and total fluoroscopic time, KAP, AK_L and AK_F. All analyses were carried out using SPSS (version 16, SPSS, Chicago, IL).

5.4. Results

5.4.1. Patient's Eye Lens Dose

The average dose received at the outer canthus and eyelid regions showed that the radiation dose received at the outer canthus region was significantly higher than the dose received by the eyelid region (Table 5.1). The range of the AK for each tube and, consequently, KAP for AVM procedures was higher than for other procedures. Due to higher dose delivery in AVM procedures, patients received higher dose at the outer canthus and eyelid locations (Figure 5.3 and Table 5.1).

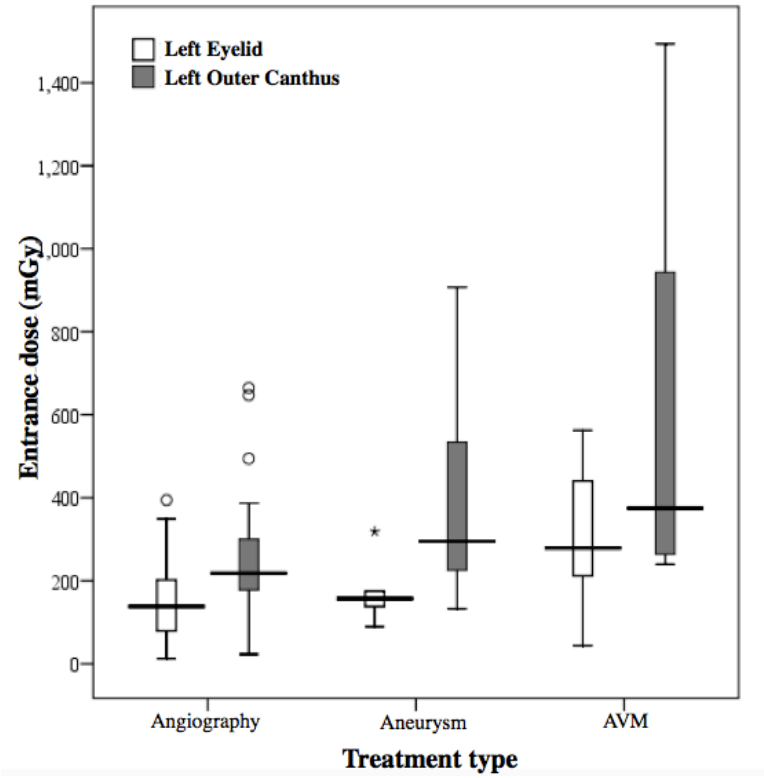

Figure 5.3. The boxplot shows the median and distribution of the dose delivered to the outer canthus and eyelid areas for each treatment procedure for the 35 participating patients, comprising 19 diagnostic angiographies, 8 treatments of cerebral aneurysms, and 8 embolizations of AVMs.

Table 5.1. Exposure parameters and dose delivered to LE and LOC areas, averages, medians, and 95th percentiles.

	KAP ($Gy.cm^2$)	AK_F (mGy)	AK_L (mGy)	FT (min)	LE Dose (mGy)	LOC Dose (mGy)
Angiography						
Average	178.8	512.1	302.3	7.2	155.0	267.8
Median	154.9	430.9	264.0	6.5	137.9	218.2
95%	385.5	893.5	716.9	12.4	353.4	648.8
Aneurysm						
Average	211.7	1060.5	516.0	18.2	168.4	393.0
Median	196.6	997.5	388.8	12.4	157.1	294.9
95%	342.1	2139.2	1125.6	44.6	268.8	809.4
AVM						
Average	314.8	1513.5	705.3	13.7	308.4	612.3
Median	238.6	855.4	439.4	8.4	278.6	374.9
95%	649.8	4193.3	1664.2	32.2	524.7	1441.4

KAP indicates kerma area-product; AK_F, air-kerma for frontal tube; AK_L, air-kerma for lateral tube; FT, total fluoroscopic time; LE, left eyelid; LOC, left outer canthus.

Figure 5.4 shows the correlation between the exposure parameters and received dose at LE and LOC. There is a strong correlation between accumulative KAP and dose values at LE and LOC regions (LOC: R^2=0.78 and LE: R^2=0.68) (Figure 5.4a). Moderate correlations were observed between total fluoroscopic time and dose at LE and LOC (LOC: R^2=0.52 and LE: R^2=0.40) (Figure 5.4b). The accumulative AK for lateral and frontal tubes shows a strong correlation with measured dose at LOC (AK_L: 0.93 and AK_F: 0.78) (Figure 5.4c,d) but a weak correlation with measured dose at LE (AK_L: 0.28 and AK_F: 0.10) (Figure 5.4c,d).

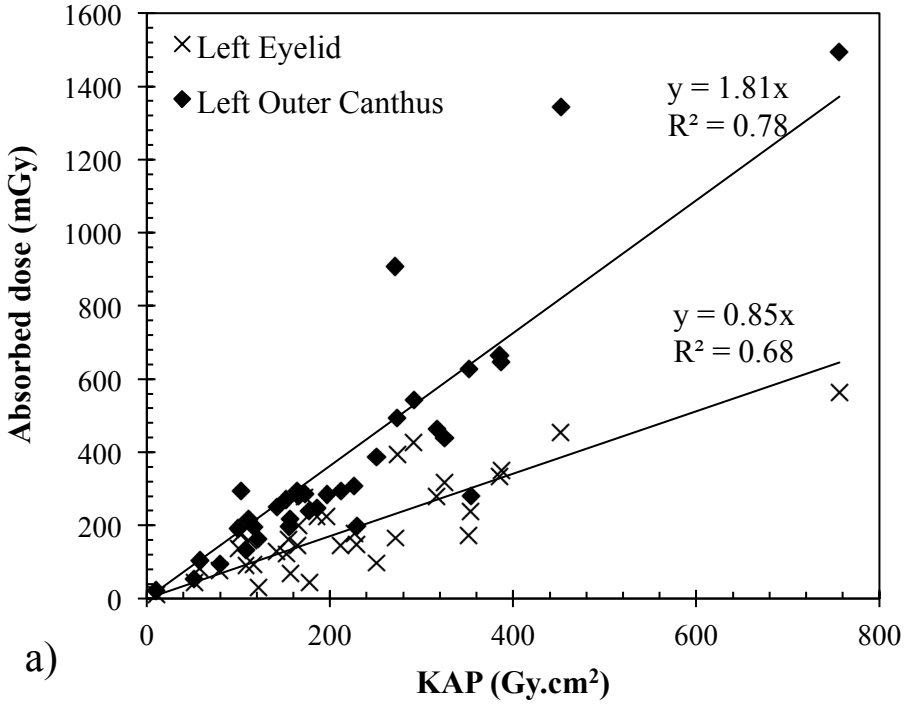

a)

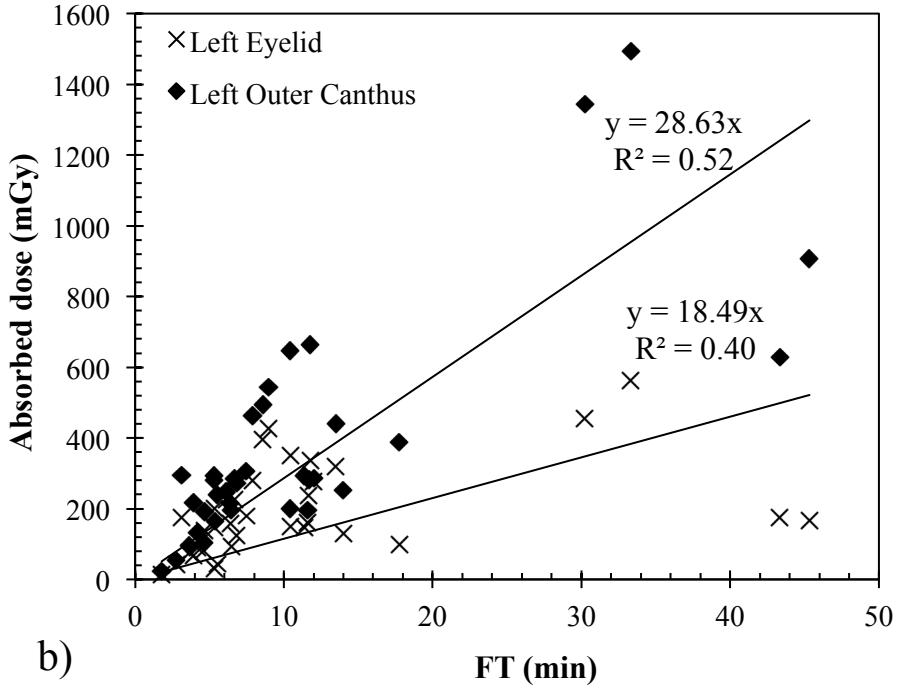
Left Eyelid
Left Outer Canthus
y = 28.63x
R² = 0.52
y = 18.49x
R² = 0.40
Absorbed dose (mGy)
FT (min)
0
200
400
600
800
1000
1200
1400
1600
0
10
20
30
40
50

b)

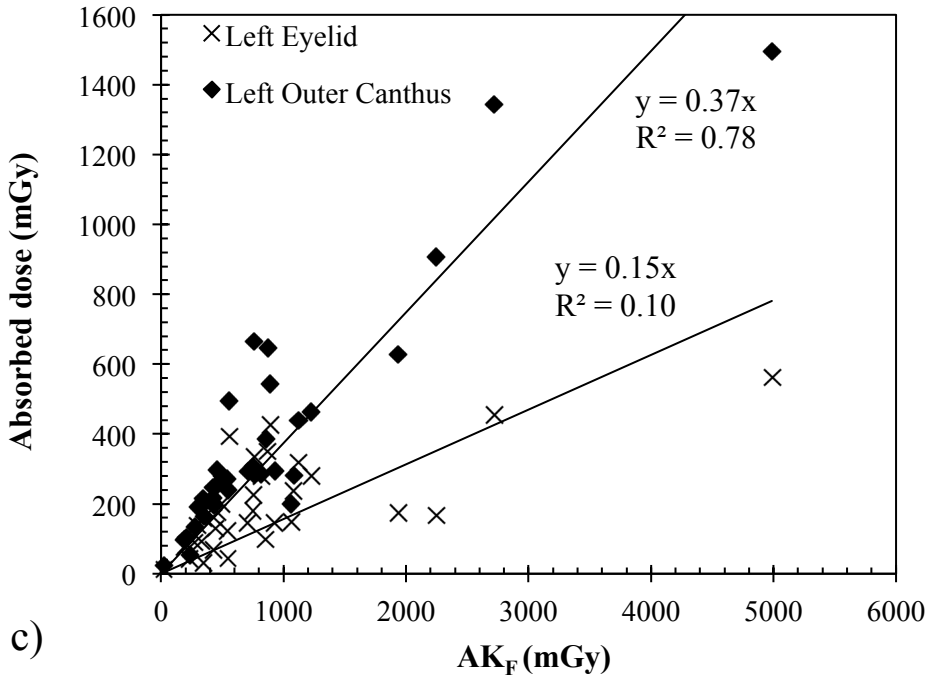
Left Eyelid
Left Outer Canthus
y = 0.37x
R² = 0.78
y = 0.15x
R² = 0.10
Absorbed dose (mGy)
AK_F (mGy)
0
200
400
600
800
1000
1200
1400
1600
0
1000
2000
3000
4000
5000
6000

c)

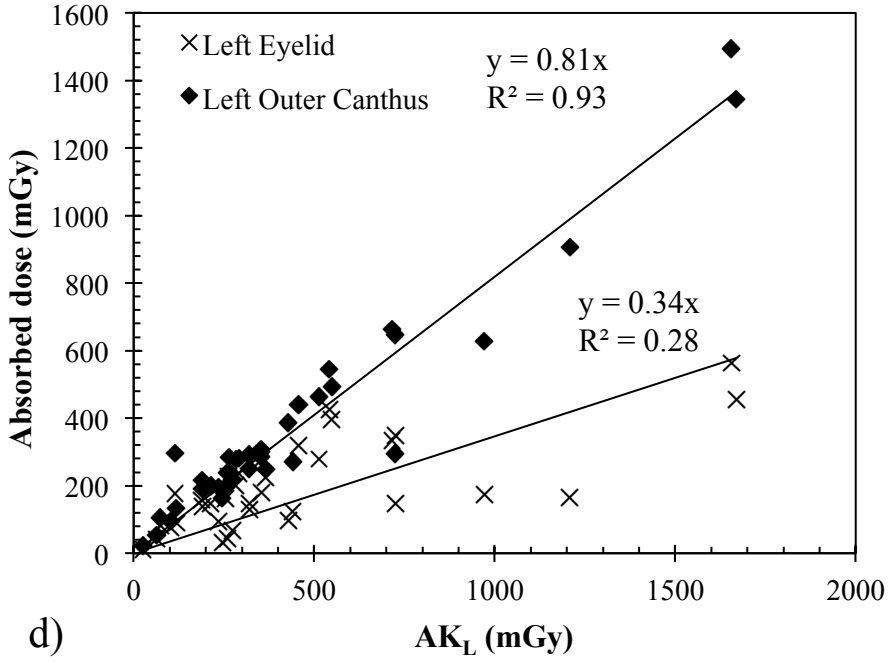

Figure 5.4. Correlation between the measured dose to left outer canthus and left eyelid regions to (a) KAP, (b) FT, (c) AK_L and (d) AK_F.

5.4.2. Study of Exposure Parameters

Figure 5.5 shows the accumulated dose trend at LOC for a particular AVM case, highlighting the unique capability of the MO*Skin* dosimetry system. Using the MO*Skin* detector, we can study the trend of the patient's accumulated dose during an interventional radiology procedure. By matching the MO*Skin* detector response and exposure time from the console we can correlate the dose measured by the MO*Skin* detectors with the machine exposure parameters, thereby understanding their contribution to the patient's received dose.

The system not only enables us to record real-time patient's dose, but also enables us to investigate the contribution of each exposure to patient's dose in terms of exposure parameters (kV, mAs, exposure angulation and rotation and number of frames) (Figure 5.5) or exposure types (Fluoroscopy, DSA, cine and road mapping) (Figure 5.6). From Figure 5.5, it was found that the sharp increments in the detector threshold voltage were

due to high dose rate DSA acquisition technique. For this particular AVM procedure, the DSA contributed to 94% of the total dose to eye lens followed by road mapping (4.7%), cine trace (0.05%) and fluoroscopy (0.08%). This information (Figure 5.5& Figure 5.6) is important for post-procedure analysis for future dose minimisation strategies and can be utilised for the interventional radiologists' training as well.

The contribution of each exposure parameters on patient's dose will be investigated in chapter 6.

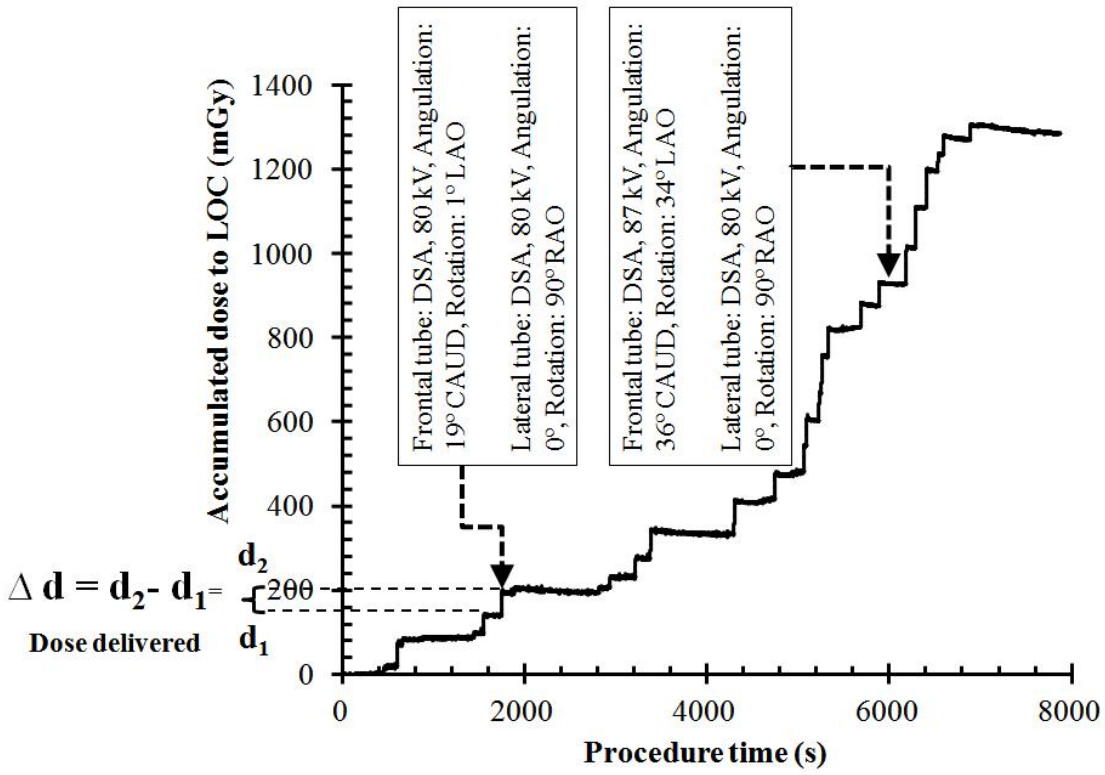

Figure 5.5 The accumulated dose trend line at LOC for an AVM procedure. From the real-time response pattern of the MO*Skin* detector, it is possible to investigate the dose delivered to the patients. The temporal dose pattern allows us to evaluate the contribution of each exposure to dose delivery to the patient's eye. Two particular exposures were labeled in this graph, d_1 is dose before exposure and d_2 is the dose after exposure. The increment dose (Δd) indicates the absorbed for this particular exposure.

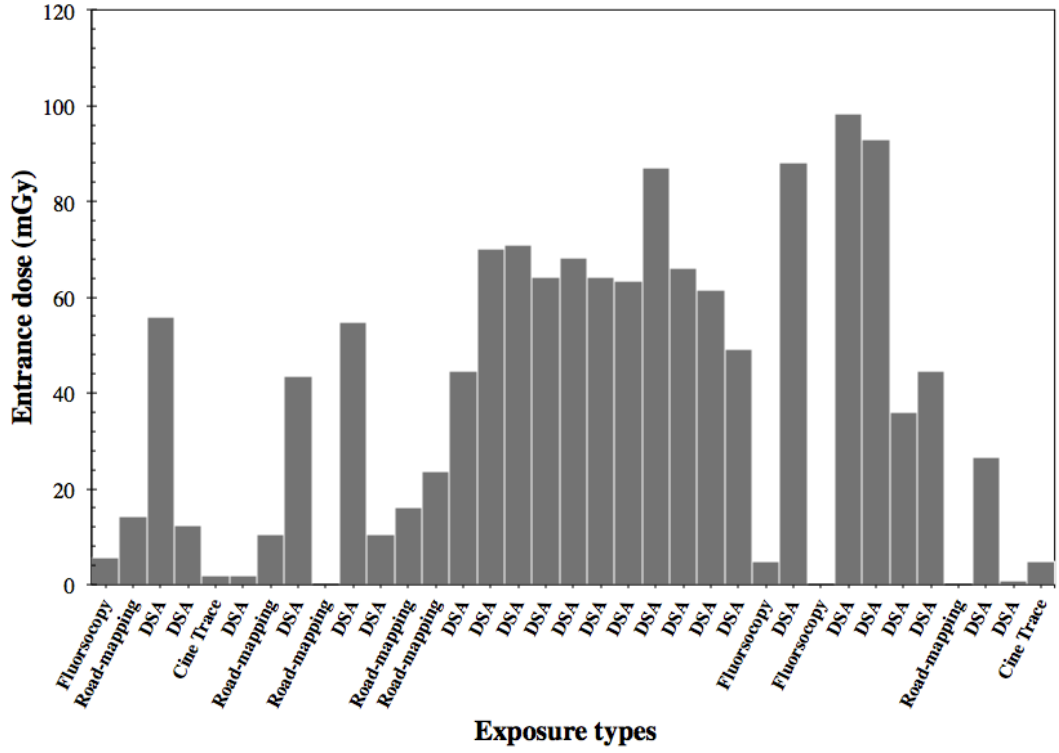

Figure 5.6 The dose delivered to the patient's LOC depicted as contribution of different types of exposure (e.g. fluoroscopy, road mapping, DSA and Cine Trace).

5.5. Discussion

Different techniques have been recommended to reduce radiation dose during interventional radiology procedures, such as using pulsed mode fluoroscopy exposure, shortening the exposure time, increasing distance between x-ray source and patient, reducing distance between image receptor and patient, minimising the magnification, maximising collimation, using last image hold technique, changing C-arm angles and using low frame rate exposure (Miller *et al*., 2003; Church *et al*., 2008).

Applying these strategies and using a direct dosimetry system can significantly improve patient radiation safety during interventional radiology procedures. Direct dose measurement is not feasible for all interventional radiology procedures; for this reason, the dose metric parameters (FT, KAP, AK_{IRP}) are regularly monitored and recorded. To prevent skin injuries, a certain threshold level has been suggested for each parameter,

for instance FT 40-60 min, KAP 500 Gy.cm^2, IRP 5 Gy and maximum skin dose 3 Gy (Stecker *et al*., 2009). While these parameters are mostly recorded after each interventional radiology procedure as a rough estimate about the radiation dose received by patient, which some studies have shown that they do not provide sufficient information during a procedure to control local skin dose to a given patient (Vano *et al*., 2001; Balter *et al*., 2002; Balter, 2006; Jaco & Miller, 2010). The actual patient's entrance skin dose can be calculated from exposure air-kerma at the reference point by incorporating table attenuation, backscatter factor, correction of actual source skin distance (Inverse square law) of reference point to actual skin point and correction of mass energy absorption coefficients of skin to air as was explained earlier in chapter 2 (Eq. 2.13) (McParland, 1998). Recently, automatic skin dose simulation tools were used to estimate the entrance skin dose from the geometrical and exposure information extracted from DICOM tags and system parameters. These software are able to map the estimated skin dose distribution on standard and anatomical patient model phantoms (Johnson *et al*., 2011; Khodadadegan *et al*., 2011).

In this study, KAP values showed strong correlation with doses received at LE and LOC regions. For the cerebral angiography procedure, the patient's eyes are frequently exposed to primary radiation beams. This may be the main reason for observing this strong correlation between KAP and measured dose at LE and LOC regions. In our centre the lateral tube was always placed at the left side of the patient's head, therefore AK_L and measured doses at LE and LOC showed strong correlation, unlike the frontal tube, which showed a weak correlation with the measured doses.

For all cases measured dose at LOC was higher than LE. This difference can be explained by two reasons; first, the closer proximity of LOC detector to the lateral x-ray tube compared to LE detector and second, collimation of the radiation field. The radiography team was well trained to minimise the irradiation dose to the left eye lens

by collimating the radiation field of the lateral tube. With proper collimation of the radiation field, the detector on the eyelid would be out of the direct radiation of the lateral tube, while the detector on the outer canthus would still be in the direct beam. The collimation effect would be significant for embolization procedures at the posterior region of the skull, which can completely place the patient's eyes outside of primary beam. This finding clearly shows the importance of choosing the right location for the point dose measurement during a non-homogenous dose distribution procedure. The maximum eye lens dose of 1492 mGy was measured at LOC region for an AVM case, followed by 907 mGy for an aneurysm case and 665 mGy for a diagnostic angiography procedure.

This study showed that among the 35 patients, LOC regions of 8 patients and LE region of one patient were found to receive higher dose than the assumed threshold dose for cataract formation (500 mGy). Recent studies have reported the average and maximum patient eye doses for neuro-interventional radiology procedures (Table 5.2). Generally, therapeutic procedures are more complicated than diagnostic procedures, which lead to longer exposure time and higher dose delivery to patients' bodies (KAP). Results of our study are in good agreement with earlier studies. As shown, detectors positioned at the lateral margin received higher doses in comparison to those placed on the eyelids or inferior and superior margins. DSA as a high frame rate and high quality imaging technique plays a major role in patient's dose contribution. Some studies have tried to evaluate the effect of DSA exposure on patient dose (Casselden, 1988; Mustafa & Janeczek, 1989). The MO*Skin* detector enables us to study the contribution of various exposure parameters on patient's dose during a clinical procedure. However, the main objective of the patient dosimetry is to monitor the total dose delivered to the patient body as well as the dose delivered to the radiosensitive organs.

Table 5.1. A summary of published data on eye doses for neuro-interventional radiology procedure.

Ref.	Interventional procedure	Number of patient	Detector type	Mean KAP ($Gy.cm^2$)	Mean Fluoroscopy time (min)	Detector position	Eye lens dose (mGy)	
							Maximum	Average
(Berthelsen & Cederblad, 1991)	Embolization	5	TLD	-	59.8	Lateral margin	139	90
(Meriçı *et al*., 1998)	Diagnostic	15	TLD	-	0.4	Inferior and superior margins	2	1.1
						Lateral margin	150	99
	Lachrymal drainage system	10	TLD	-	5.6	Inferior and superior margins	66	38
						Lateral margin	294	176
(Ilgit *et al*., 2000)	Balloon dacryocystoplasty	10	TLD	-	3.9	Inferior and superior margins	68	38
(Theodorakou & Horrocks, 2003)	Embolization	30	TLD	106.0	14.0	-	500	60
(Moritake *et al*., 2008)	Therapeutic interventional radiology	28	PLD	-	55.6	Lateral margin	2079	380
(Sandborg *et al*., 2010)	Diagnostic	19	TLD	54.7	6.9	Left Eyelid	-	7.8
	Coiling	27	TLD	121.0	32.0	Left Eyelid	515	51
	Embolization	25	TLD	189.0	39.8	Left Eyelid	289	71
This study	Diagnostic	19	MO*Skin*	178.8	7.2	Left Eyelid	394	155
						Lateral margin (LOC)	665	268
	Embolization	16	MO*Skin*	314.7	15.9	Left Eyelid	563	238
						Lateral margin (LOC)	1492	502

A real-time dose monitoring system can provide real-time information for each particular exposure. This information can be used to study the techniques to optimise patient's radiation safety during interventional radiology procedures, such as changing the exposure angulation, adjusting the exposure collimation, and shortening the exposure time when the dose at detector position is reaching to a critical level.

5.6. Chapter Summary

In conclusion, this chapter discussed research objective 2 to demonstrate the feasibility of the MO*Skin* dose monitoring system as a real time, *in-vivo* dose measurement system. This system was successfully used to measure patient eye lens dose during neuro-interventional procedures. In addition, the MO*Skin* dose monitoring system enables interventional radiologists to have better awareness of the patient's eye lens dose during clinical procedures. This chapter also provides respective findings to research objective 3 to indicate indirect dose measurements using machine available dose metrics such as KAP, FT, and air-kerma are not accurate indicator of the actual dose received by patient's eye undergoing interventional radiology procedures. This information can only be obtained via actual *in-vivo* dose measurements.

In the following chapter, MO*Skin* detector was used as a real-time dose monitoring system in order to study the contribution of each controllable exposure parameters, such as exposure direction, frame rate, exposure duration, distance between image receptor to patient's body, and image magnification on patient's skin and eye lens dose during a neuro-interventional procedure.

CHAPTER 6: AN INVESTIGATION OF THE CONTRIBUTION OF ROUTINE RADIOLOGICAL EXPOSURE PARAMETERS TO PATIENT'S DOSE DURING NEURO-INTERVENTIONAL RADIOLOGY PROCEDURES: A PHANTOM STUDY

6.1. Introduction

Interventional radiologists are often unaware that skin injuries can even occur with modern interventional units and they are not generally conscious about magnitude of the radiation dose to the patient's body. For this reason, many of interventional radiologists underestimate the potential of occurrence of the skin injuries and consequently an underreporting of the number of skin injuries during interventional procedures is suspected. Various controllable exposure parameters could considerably change the patient's dose during fluoroscopy radiology procedures, such as exposure direction, field dimension, frame rate, beam-on duration, and distance between image receptor to patient's body. The purpose of this chapter is to investigate the effects of routine exposure parameters on patient's dose during neuro-interventional radiology procedures, which will attempt to discuss research objective 4.

6.2. Literature Review

Until the late 1980s, diagnostic procedures were classified as low dose radiation procedures and were only linked with stochastic risks. Since the 1980s, fluoroscopically-guided interventional radiology procedures have become widespread and have been used effectively to diagnose and treat numerous vascular and cardiac diseases. However interventional radiology procedures provide enormous advantages over invasive surgical procedures, like shorter hospitalisation time, less trauma to the patient, lower infection risk and lower treatment costs (UNSCEAR, 2010) long periods of radiation exposure may increase the risk of deterministic effects in patients, thus causing radiation-induced skin injuries.

Vano *et al.* in 2001 reported patients maximum skin dose during 26 coronary angiographies and seven percutaneous transluminal coronary angiographies (PTCAs) and compared with KAP values. Values of 107-711 mGy were reported for the patients' maximum skin doses, which were not in good correlation with the KAP values (Vano *et al*., 2001b). Vano *et al.* in their further investigation on incidence of skin injuries in 14 patients who underwent multiple coronary angiographies (between 4 and 14 times) and who had more than four PTCAs (between 5 and 10 times), reported mean values of patients' maximum skin doses per procedure were 217 mGy for the diagnostic examinations and 391 mGy for the PTCA procedures. This study reported, a slight clinical demonstrated radiation skin injury in one patient who had a history of 10 coronary angiographies and 10 PTCAs (estimated maximum skin dose 9.5 Gy), a slight telangiectasia and discrete pigmentation in one patient who had a history of 14 coronary angiographies and 10 PTCAs (estimated maximum skin dose 7.3 Gy), and a pigmentation in a patient who underwent seven coronary angiographies and six PTCAs (estimated maximum skin dose 5.6 Gy). There was no skin injuries reported in other 11 patients (Vano *et al*., 2001a).

A study on patients' maximum skin dose during interventional cardiology procedures revealed that among 8 coronary angiography (CA) and 16 PTCAs procedures, radiation skin dose greater than 3 Gy recorded in only one PTCA procedure (Giordano *et al*., 2010). This study showed that, for coronary angiography procedures the average and maximum skin dose values were recorded 162.5 mGy and 470 mGy, respectively. In other hand, the average and maximum skin dose values of PTCA procedures were reported 964.3 mGy and 3780 mGy, respectively. There was a good correlation reported between fluoroscopy time and maximum skin dose values during PTCAs ($r = 0.80$) and a strong correlation between KAP and maximum skin dose ($r = 0.90$).

Vano *et al.* in 2013 reported the results of a two-years follow-up program applied to potential skin injuries during 708 interventional neuroradiology procedures (325 in 2009 and 383 in 2010). Several optimising actions were implemented during 2010, such as decreasing the number of pulses/second, a 20-hour training course focused on radiation protection for fluoroscopy guided procedures, and display the patient dose information in the x-ray room during the procedure. This study showed that, however the 2009 median values for KAP and dose level at IRP were very similar to the 2010 ones; but, the third quartile of dose level at IRP values were lower in 2010 (3.3 Gy) than in 2009 (3.9 Gy) and number of patients needed follow-up program (total IRP values exceeded from 5 Gy) dropped from 19 patients (5.9%) in 2009 to 11 patients (2.9%) in 2010 (Vano *et al*., 2013).

During interventional radiology procedures, x-rays can enter the patient's body from different directions with various exposure parameters, such as collimation size and exposure type. These changes cause an inhomogeneous skin dose distribution during a clinical procedure, which make finding patients' skin dose distribution complicated. For this reason having a clear picture about the contribution of different exposure parameters on patient's dose is essential.

6.3. Materials and Methods

This work included two aspects: the first part involved a survey of the exposure parameters commonly used during clinical neuro-interventional procedures; the second part, an analysis of the effects of these parameters on patient's eye lens and entrance skin dose (ESD) using an anthropomorphic tissue-equivalent phantom.

This chapter looked at 58 patients who underwent neuro-interventional procedures operated with the Philips Allura Xper FD20/20® biplane system by the same interventional radiologist and radiography team. The exposure parameters (exposure time, field dimension, frame rate, angulation, rotation, etc.) were extracted from the x-

ray machine's computer and this data is henceforth called the "machine data". The machine data extracted from the Philips Allura Xper FD20/20® system provided detailed information on exposure parameters and exposure types, which are vendor specific. These include DSA, cine trace, fluoroscopy, fluoroscopy-mapping, cine 3D, and fluoroscopy smart mask. In the interest of brevity, the extracted machine data were summarised into three main exposure types, i.e. fluoroscopy, DSA and cine imaging techniques. Fluoroscopic techniques were used for wire or catheter guiding, anatomy visualisation and to locate sites of surgical excision. Fluoroscopy, fluoroscopy-mapping and fluoroscopy smart mask exposure techniques were grouped under fluoroscopy exposure.

DSA is often used as high definition dynamic imaging of contrast-enhanced blood vessels with high quality image acquisitions. Cine imaging is a DSA-based technique used to provide a vessel mask image for fluoroscopy-mapping (called cine trace). Alternatively, it can produce reconstructed 3D images to enable better assessment of vessel shape, size, and relationships with adjacent vessels (called cine 3D). The exposure parameters (tube voltage (kV), filtration, and tube current-time product (mAs)) in the Philips Allura Xper FD20/20® suit are controlled by Automatic Dose Rate Control (ADRC) system. Further information about the Philips Allura Xper FD20/20® biplane system and ADRC system were presented in chapter 3 section 3.4 and section 3.5, respectively. The ADRC system seeks to attain an adequate image quality and adhere to standard regulations for diagnostic reference levels (DRLs) based on As Low As Reasonably Achievable (ALARA) principle. This system controls the image contrast to noise ratio (CNR) and patient's dose following pre-programmed filtration and exposure parameters (tube voltage and current-time product).

In the second part of this chapter, the contribution of various exposure parameters to patient's eye lens and skin doses was investigated using an adult female phantom (ATOM®, model 702, CIRS, Norfolk, VA). The radiation dose measurements were performed using the MO*Skin* dosimetry system. The head section of the phantom up to the shoulder was used in our study. Five MO*Skin* detectors were placed on the occipital region, left and right ears and left and right eyes of the phantom (Figure 6.1a & Figure 6.1b). The Philips Allura Xper FD20/20® biplane system, equipped with one ceiling mounted and one floor mounted x-ray tubes, was used. These provide two sequential images from the lateral and frontal directions respectively (Figure 6.1c). The phantom was placed on the patient support couch, centred at the machine isocentre (focal spot to isocentre distance, 81 cm) with non-magnified imaging (field dimension: 48 cm) and the flat panel detector was placed at 120 cm from the focal-spot point. The phantom was exposed by 3fps acquisition mode (cerebral vascular application) for duration of 20s. The x-ray tube's output was controlled by the ADRC system during measurement. This setup is henceforth called the "standard setup". Effects of controllable exposure parameters (exposure time, angle, field dimension, image receptor to patient distance, and frame rate) on ESD and eye lens dose were considered individually.

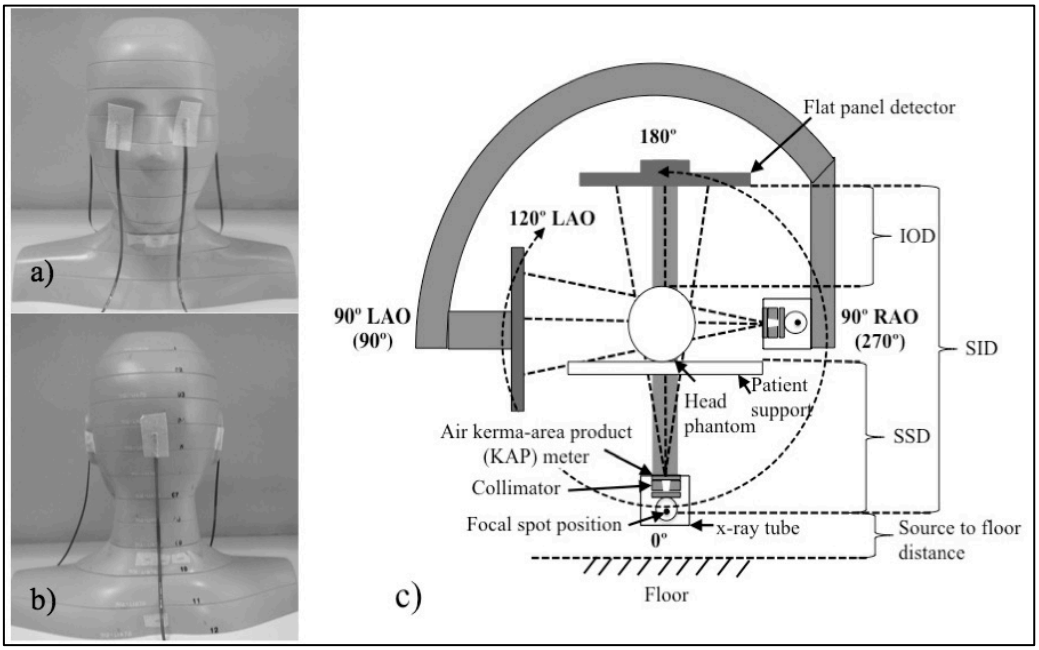

Figure 6.1 (a & b) The MO*Skin* detectors were positioned on the occipital, left ear, left eye, right ear and right eye of the anthropomorphic phantom and c) Diagram of measurement arrangement under the Philips Allura Xper FD20/20® biplane system.

6.3.1. Exposure Time

The treatment outcome is the first priority in all procedures; hence, the use of long periods of high frame rate imaging techniques may be unavoidable in complex cases. The beam-on period for different exposure types, such as fluoroscopy, cine, and DSA imaging was investigated using the machine date. The exposure parameters (tube voltage and current-time product) of these imaging techniques have also been extracted from the machine data.

The effect of the DSA exposure time on patient's dose was studied using the anthropomorphic phantom. In this study, the measurement was set up as per the "standard setup" and contribution of exposure time on ESD and eye lens dose were investigated for the frontal and the lateral tubes individually. For anterior-posterior projections the frontal tube was placed under the couch at 0º and for lateral projection the lateral tube was rotated to 90º from the left side of the head phantom (90º RAO)

(Figure 6.1c). The ESD and eye lens dose were measured for various exposure times of 10s, 20s and 30s.

6.3.2. Field Dimension

When image field dimension is changed, the system adjusts the collimators to reduce the area of exposure while automatically increasing the tube output. This is because the ADRC system attempts to control the patient's dose and also maintain sufficient dose to the flat panel detectors to ensure consistent image brightness by adjusting the tube voltage (kV) and/or tube current-time product (mAs). This is in contrast with a simple collimation of the radiation field, where the tube voltage and current-time product were not varied. In this study the field dimension ranges for different exposure types were extracted from the machine data.

The contribution of imaging field dimension to patient dose was studied for both frontal and lateral tubes. The measurement was initially set up as per the "standard setup". For the posterior-anterior projection (exposure angle: 0º), the field of view was centred on the occipital region detector and for lateral projection (90º RAO); the field of view was centred on the left eyelid detector.

6.3.3. Image Object Distance

It should be mentioned that, the machine data does not directly provide information about image receptor to patient's body distance, but provides information about the source-image-distance (SID), couch to floor distance, and object thickness (Figure 6.1c). These parameters can be used to calculate the distance between the frontal tube image receptor to patient's body of different projection angles using Eq. 6.1 (Figure 6.2)

$$\text{Image receptor to patient's body distance} = SID - (X + Patient's\ thickness). \qquad \text{Eq. 6.1}$$

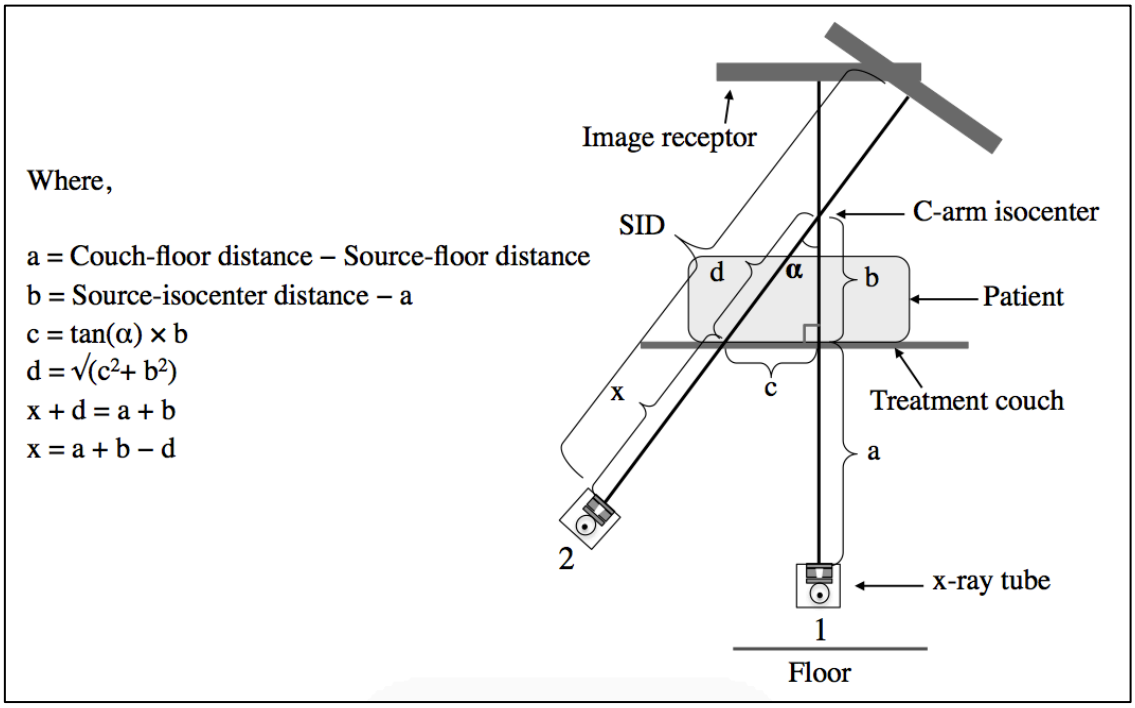

Figure 6.2 Calculation of distance between the image receptor to patient's body of different tube angles using extracted exposure parameters from machine data. The x-ray tube was plotted from 0º (#1) and αº (#2).

Source to floor distance for the Philips Allura Xper FD20/20® is 32.5 cm. Object thickness was extracted from the machine data, which was calculated automatically for each exposure by measuring the radiation dose at the exit of the x-ray tube and at the surface of the flat panel detector. Subtraction of these dose levels shows the amount of the attenuated dose by the patient's body (assumed to be water equivalent).

The contribution of image receptor to patient's body distance to patient's dose was studied using the head phantom. For this measurement, the patient support couch was positioned at the shortest distance to the floor (57 cm). The image receptor was positioned at different distances from the phantom surface, at 50, 40, 30 and 20 cm by varying SID from 120 to 90 cm. Other exposure parameters were set up as per the "standard setup".

6.3.4. Frame Rate

Modern fluoroscopy often uses pulsed radiation mode in order to reduce radiation dose to the patient. The routine exposure frame rates of the DSA imaging technique during the 58 neuro-interventional procedures were extracted from the machine data. The contribution of the DSA exposure frame rate to patient dose was measured using the head phantom set up as per the "standard setup" with varying frame rates, 2, 3, 4 and 6 fps.

6.3.5. Exposure Angle

The exposure angles for frontal and lateral tubes vary greatly, depending on the interventional radiologist's opinion according to the clinical circumstances. The routine exposure angles for the frontal and the lateral tubes during neuro-interventional procedures were extracted from the machine data.

To test their contribution to patient's dose, the phantom was initially set up as per the "standard setup". The effect of exposure angle on the delivered dose was studied for different projection angles for the frontal and lateral tubes (frontal tube: 60º LAO to 60º RAO; lateral tube: 70º RAO to 170º RAO in 10º intervals). The exposure parameters (tube voltage and current-time product) were recorded from the console.

6.4. Results

Study of the machine data for 58 clinical neuro-interventional procedures showed that the frontal tube is used more frequently, contributing to 75.4% of the total KAP (Table 6.1). DSA contributed the highest patient's dose (80.9%) followed by cine imaging (11.2%) and fluoroscopy (7.9%). In terms of total frame number, this amount of radiation dose was delivered using DSA (5.3%), cine (8.0%) and fluoroscopy (86.7%) (Table 6.2). Hence, DSA procedures, although used sparingly during clinical

procedures, contributed the largest patient dose. Therefore, in this work, the DSA acquisition mode was used in the study the various exposure parameters. In addition it was found that, the most frequent tube energy during DSA imaging technique were 80kVp (effective energy 42.7 keV) (52.4% of all DSA exposures).

Table 6.1. Contribution of the frontal and lateral tubes in terms of their KAP, AK, and number of imaging frames during 58 neuro-interventional procedures (%).

	KAP	**AK**	**Number of frames**
Frontal tube	75.4	75.4	74.8
Lateral tube	24.6	24.6	25.2

Table 6. 2. Contribution of different exposure types operated by the frontal and lateral tubes during the neuro-interventional procedures (%).

	Tube	**DSA**	**Cine**	**Fluoroscopy**
KAP	Frontal	79.6	11.5	8.9
	Lateral	82.3	10.9	6.8
AK	Frontal	76.3	12.1	11.6
	Lateral	77.3	12.9	9.8
Number of frame	Frontal	4.5	7.6	88.0
	Lateral	6.1	8.5	85.4

6.4.1. Exposure Time

Exposure time varies widely depending on the complexity of the procedure and the experience of the interventional radiologists. Study of the machine data showed that fluoroscopic exposures were the most commonly used exposure type, contributing to 86.9% of the total exposure time (with median exposure time of 4s and maximum exposure time of 192s). The fluoroscopy imaging was used with various ranges of exposure times (Figure 6.3). DSA technique was performed with short beam-on periods

(mean = 8.6 ± 3.4 s), making up 11.3% of the total exposure time. Cine imaging technique had the shortest beam-on periods (mean= 2.9 ± 1.9 s) and contributed to 1.8% of the total exposure time. In general, the x-ray tube current-time product (mAs) during DSA imaging technique was considerably higher than other imaging techniques during the neuro-interventional procedures.

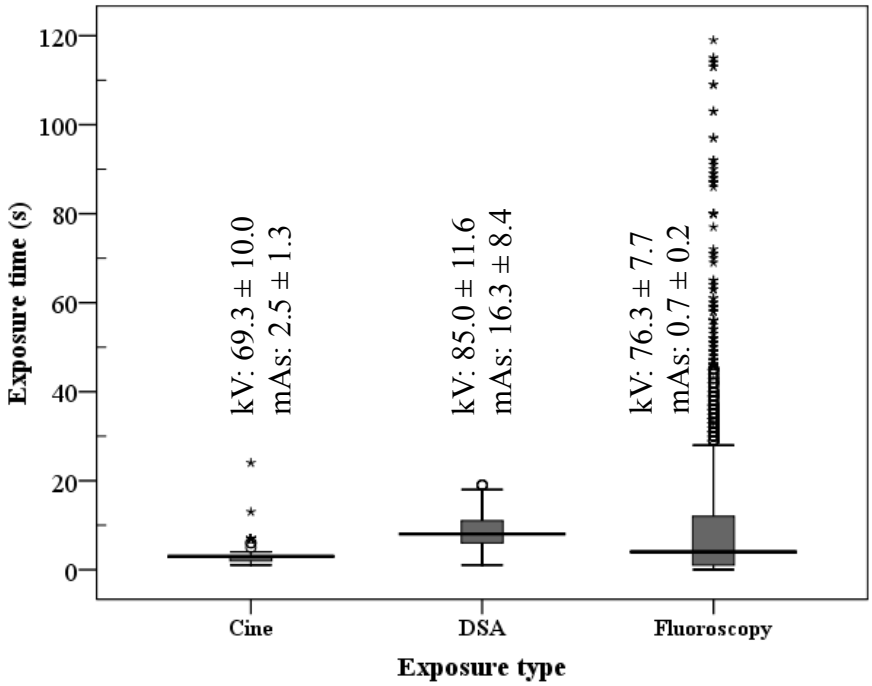

Figure 6.3 Exposure time for various exposure techniques during neuro-interventional radiology procedures. Mean and 1 standard deviation of the tube voltage (kV) and tube current-time product (mAs) were also presented.

The effect of DSA acquisition time on patient's dose was studied using the phantom. Figure 6.4 shows the dose for a range of exposure times (10s to 30s) at different phantom locations. With the frontal tube positioned under couch, the ESD in the occipital region was increased linearly from 3.73 cGy to 10.27 cGy (by a factor of 2.75), however phantom eyes and ears were exposed by the exit radiation, which relatively transfers considerably lower radiation dose (max <2 cGy) (Figure 6.4a). When the lateral tube was placed on left side of the head phantom (90º RAO), changing the

exposure period from 10s to 40s increased the radiation dose at left ear and left eye by a factor of 2.76 and 2.82, respectively (Figure 6.4b).

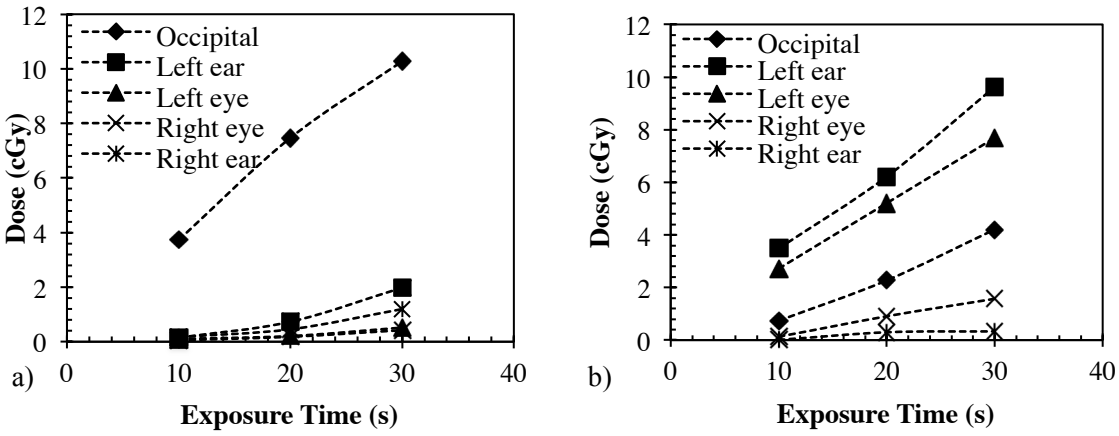

Figure 6.4 Exposure time effects on received dose at different locations of the phantom delivered with the (a) frontal tube at 0º and (b) lateral tube at 90º RAO.

6.4.2. Field Dimension

From the machine data, the most common image field dimensions of the frontal and lateral tubes for DSA, cine, and fluoroscopy exposures were found to be 37, 31 and 31 cm, respectively. The field dimensions of 48 cm and 41 cm are non-magnified images for the frontal and lateral tubes, respectively.

Study of the field dimension contribution on patient's showed that, when the imaging field dimension is changed, the ADRC automatically adjusts the tube voltage (kV) and current-time product (mAs). Changing the frontal tube field dimension from 48 cm to 15 cm increased the ESD at the occipital region by a factor of 1.94 (from 14.7 to 28.6 cGy) (Figure 6.5a). In this measurement for smaller field dimensions (< 31 cm), the ears were out of the exposure field of view; hence received very low radiation. Changing the lateral tube field dimension from 42 cm to 15 cm considerably increased the left eye dose by a factor of 4.75 (from 1.2 to 5.7 cGy) (Figure 6.5b).

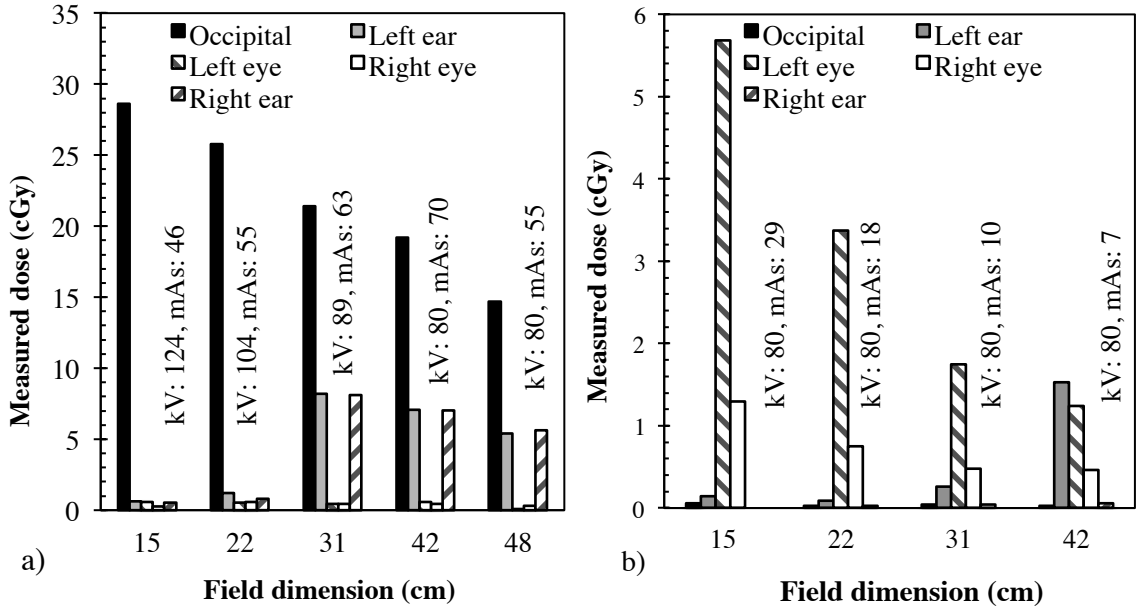

Figure 6.5 Effect of the image field dimension on x-ray tube output and exposure dose, a) for frontal tube placed at 0º and b) for lateral tube placed at 90º RAO.

6.4.3. Image Object Distance

Measurement of the frontal tube and image receptor positions based on Eq. 6.1 showed that, the image receptor of the frontal tube was mostly placed 10-20cm away from the patients' bodies (52.4%), followed by 0-10cm (23.4%), 20-30cm (19.3%), and 30-50cm (4.9%). This survey enables us to gain a better understanding of the common distances of the frontal tube image receptor to patient's body during a clinical neuro-interventional procedure.

The effect of image receptor to patient's body distance variation on patient's dose was studied using the phantom. Variation of the frontal tube's image receptor to phantom surface distance from 10 to 40 cm when the x-ray tube was positioned under the couch (0º) changed the exposure current-time product (mAs) from 28 to 61. As a result the occipital dose was doubled (Figure 6.6).

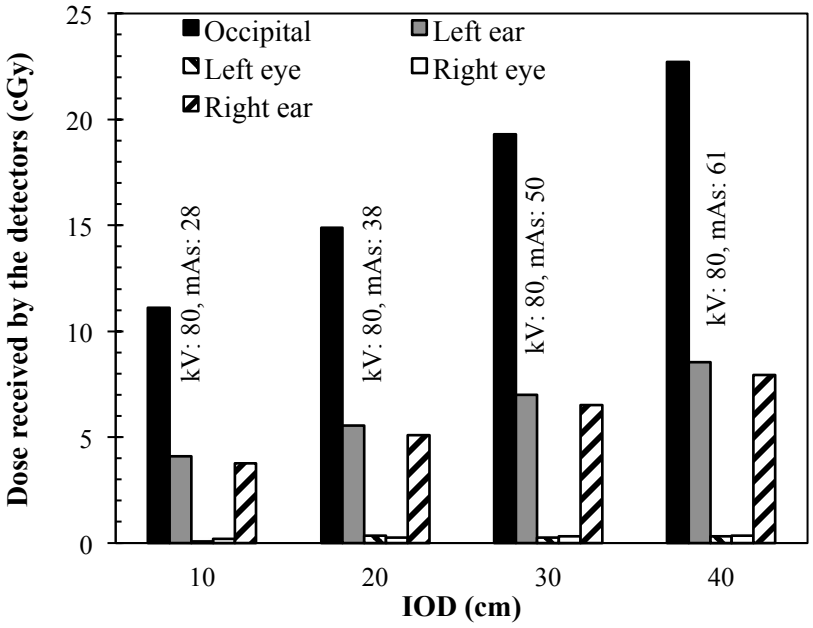

Figure 6.6 Effects of IOD variation on delivered dose to the detectors.

6.4.4. Frame Rate

The machine data showed that in 50.1% of cases frame rate was 3fps for DSA exposures, which was followed by 4fps (21.7%), 2fps (17.4%), 0.5fps (9.4%), and 0.5fps (1.4%).

The effect of the DSA exposure frame rate on patient dose was studied for the frontal tube using different frame rates, 2, 3 and 4 fps. The phantom study showed that that by changing the frame rate from 2fps to 4fps, the ESD at the occipital region increased by 88% (Figure 6.7).

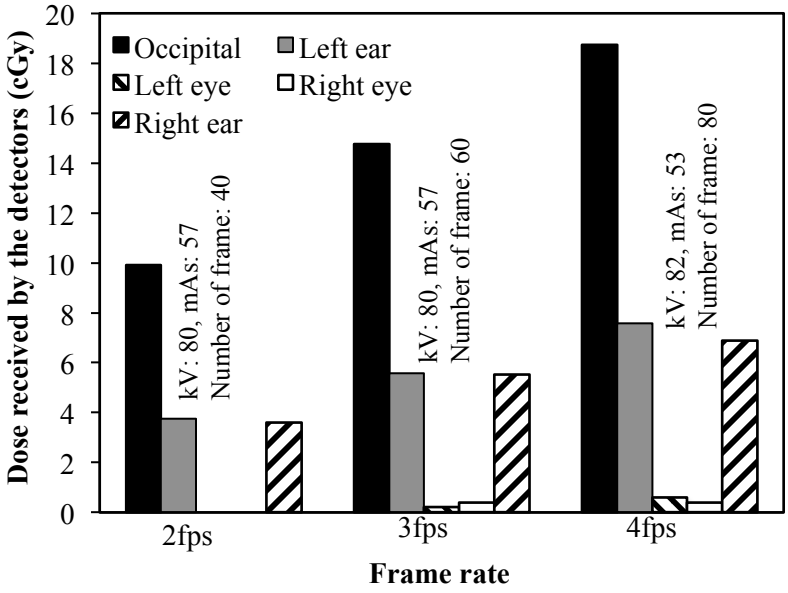

Figure 6.7 Effect of the frame rate on exposure parameters and exposure dose.

6.4.5. Exposure Angle

Figure 6.8 shows the projections used during neuro-interventional procedures. Study of machine data illustrated that 73.7% of the frontal tube projections were acquired in the posterior-anterior direction (10º RAO-10º LAO) and 93% of the lateral tube projections were acquired from 70º RAO to 90º RAO (Figure 6.9a). The tubes' angulations frequently changed within 10º caudal to 10º cranial (frontal tube: 77.2% and lateral tube: 100%) (Figure 6.9b).

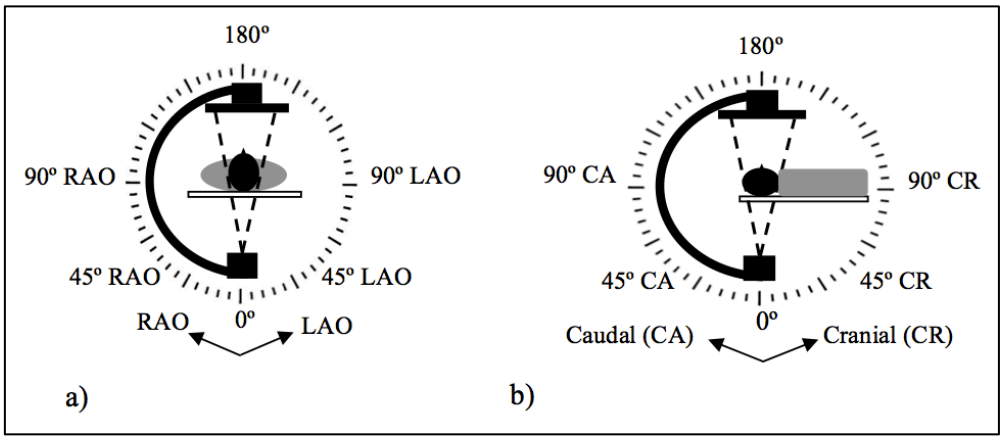

Figure 6.8 Diagram of the frontal tube projections; a) rotation (RAO and LAO) and b) angulation (cranial and caudal) in relation to the patient's position.

The frontal and lateral tube rotations effects on radiation dose to the occipital region and eye lens were evaluated using the head phantom. Figure 6.10a and Figure 6.10b show the effect of frontal x-ray tube rotation on exposure current-time product (mAs) and dose to the occipital and left eye regions. As Figure 6.10a shows, the frontal tube exposure current-time product (mAs) has its maximum value when the x-ray tube was positioned under the couch (0º), and its value gradually decreases by rotating the imaging direction. This study showed that rotation the frontal tube projection from 0º to 60º RAO and 60º LAO reduces the radiation dose received by the detector at occipital region up to 40% (Figure 6.10a).

However, rotation of the frontal tube from 0º to 60º RAO reduces the exposure current-time product (from 28 to 17 mAs), this rotation gradually places the patient's left eye inside of the entrance radiation field. Consequently, changing the exposure rotation from 0º to 60º RAO significantly increased the dose received by the detector positioned at phantom's left eye up to 11.4 times (Figure 6.10b).

Study of the lateral tube's exposure angle showed that changing the exposure direction from 70º RAO to 90º RAO increases the radiation dose to the left eye by up to 86%. The left eye dose showed a gradual rise from 90º RAO to 170º RAO, due to the increase in the exposure current-time product (mAs) (Figure 6.10c).

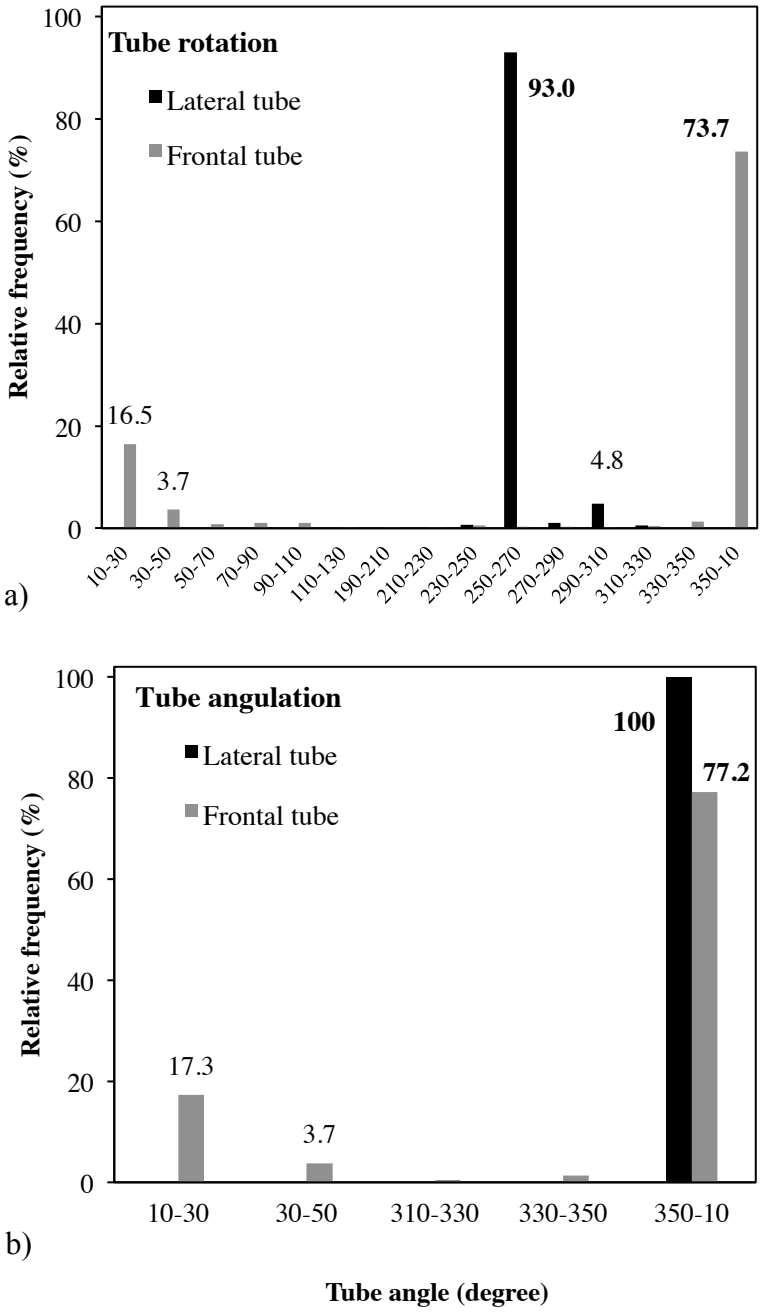

Figure 6.9 a) Rotation of the frontal and lateral tubes during the 58 neuro-interventional procedures (LAO orientation: 0º to 180º and RAO orientation: 180º to 360º and b) x-ray tubes angulations (caudal orientation: 0º to 180º and cranial orientation: 180º to 360º).

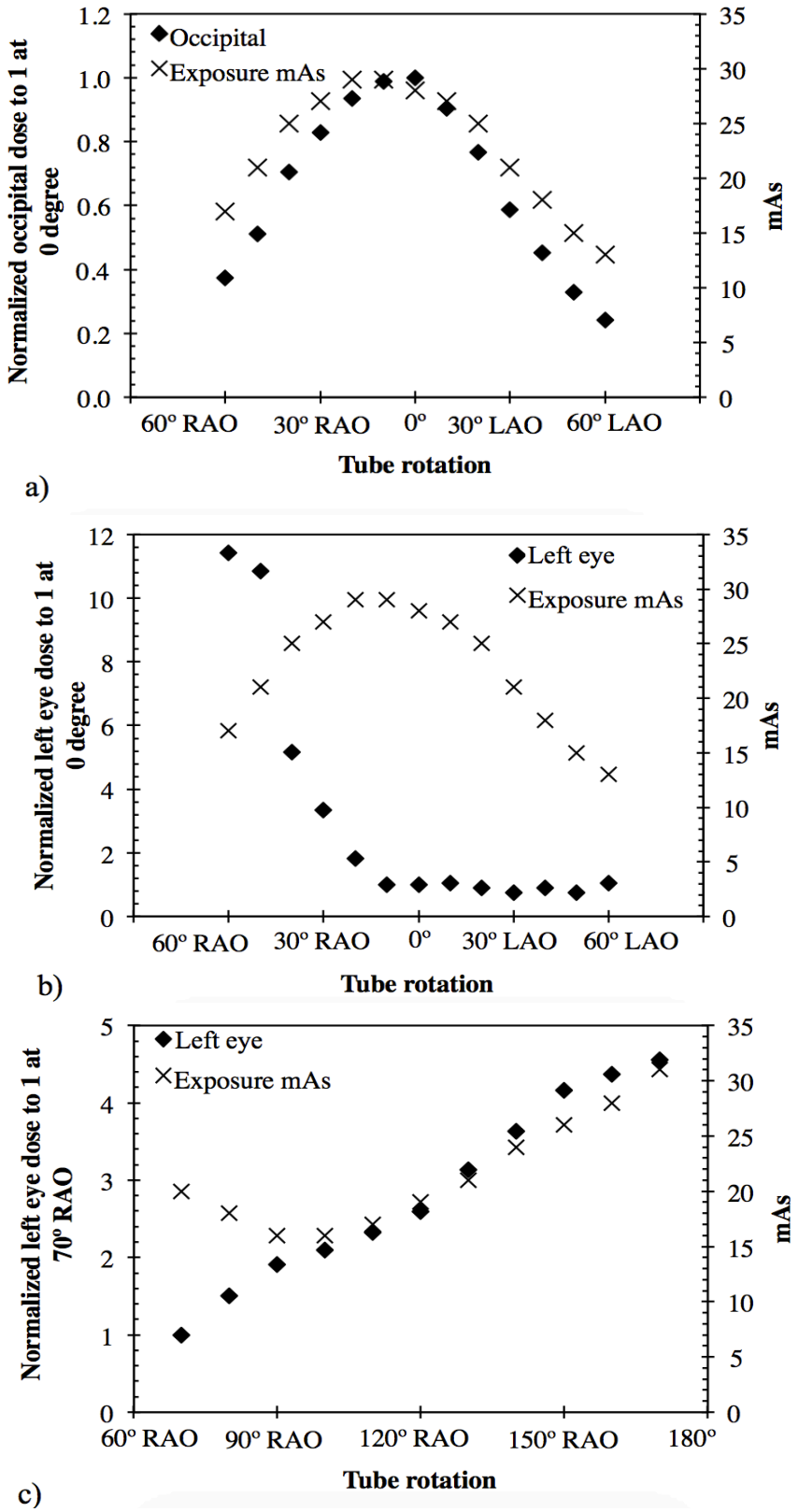

Figure 6.10 Effect of the frontal tube rotation on exposure current-time product (mAs) and dose delivery to the a) occipital region, b) left eye, and c) Effect of the lateral tube rotation on dose delivery to the left eye.

6.5. Discussion

As it is well known, operators play an important role in controlling the patient dose level during fluoroscopy guided interventional radiology procedures. In an attempt to manage radiation dose to the patient, operators are asked to record patient dose via available dose metric systems (KAP, fluoroscopy time, and air-kerma at the interventional reference point) and to keep these values under the suggested threshold level to avoid skin injuries, KAP 500 Gy.cm^2, fluoroscopy time 40-60 min, and air-kerma at the interventional reference point 5 Gy (Stecker *et al*., 2009). The dose metric values are recorded in the patient's medical record. The patient's radiation dose history should be considered for those patients who are undergoing an additional high radiation dose procedure or a repeated angiography procedure. Patients who have received a large radiation dose should be followed up.

As this chapter showed, DSA imaging technique contributed the highest patient radiation dose (80.9% of the total KAP) even though it was only used 11.3% of the total exposure time (Figure 6.3). A study on exposure parameters during coronary interventional procedures revealed that 66% of the total KAP is caused by digital cine angiography, which occupies only 13% of the total exposure time (Efstathopoulos *et al*., 2004). These findings show that a small change in the time for high dose-rate imaging techniques (DSA and cine imaging) may considerably reduce the patient dose during interventional radiology procedures.

Modern fluoroscopic suites can electronically magnify the image and provide a range of field dimensions (magnification ranges), resulting in different dose rate levels. The brightness gain of the image receptor decreases as the field dimension increases and the ADRC system compensates for the blurrier image by boosting the tube exposure rate and consequently increases the patient's dose (Bushberg *et al*., 2003). Different research groups have emphasised the importance of limiting the electronic magnification usage

and suggested that this technique be used only when necessary (Mahesh, 2001; Vano *et al*., 2001; IAEA, 2010; Chida *et al*., 2010).

Generally, patient dose increases when the magnification level increases (smaller field dimension) and patient ESD is assumed to be increased by the square of the ratio of the image intensifier diameters (Mahesh, 2001). This assumption may give an unrealistic estimation of patient ESD. For instance, based on this assumption, when the electronic magnification is changed from 48 cm to 15 cm field size, the patient's ESD increases by a factor of 10.2 ($(48/15)^2$), but our study showed that ESD (at occipital region) would increase by a factor of 1.9 (Figure 6.5a).

Several studies have shown that closer proximity of the patient's eye to the lateral tube is one of the main reasons there is a considerable difference in the left and right eyes doses (Ilgit *et al*., 2000; Sandborg *et al*., 2010). This study showed that the lateral tube was mostly used at 70º RAO to 90º RAO, (93% of total KAP) and for this exposure angle range, the left eye dose increased up to 86% (Figure 6.10c). Furthermore, for lateral tube angulations of 90°RAO to 170°, which considered as anterior-posterior view, the exposure current-time product (mAs) steadily growths. Thus, direct x-ray beam and higher beam intensity contributed to the increase in radiation dose to the eye for these angles.

Early skin reactions (early erythema) can be observed after 2 Gy (Wagner, 1998), which is four times higher than the suggested threshold dose for cataract formation (0.5 Gy (Stewart *et al*., 2012)). Therefore, unlike skin reactions, which are generally visible in few hours to few weeks after irradiation, lens opacity and cataract formation appear after several years (Table 2.1). Hence, controlling and monitoring patient eye lens dose is essential for long fluoroscopy guided interventional procedures.

6.6. Chapter Summary

Complex neuro-interventional procedures may incur high radiation exposures to patient, resulting in radiation induced tissue reactions such as skin injuries and cataract formation. Optimisation of radiation exposure techniques can help to achieve a reasonable minimum skin dose and/or eye lens dose to the patient. In this chapter, a detailed survey of routine exposure parameters of 58 neuro-interventional procedures is presented. The contribution of each exposure parameter on patient's skin and eye was quantitatively evaluated using an anthropomorphic phantom. Although the success in treatment is the first priority for all interventionalists, while other treatment risks, such as patient radiation dose are relatively less important, this study showed that making small changes in selected exposure parameters could help interventionalists to strike a balance between the benefits of long interventional procedures and radiation risks for the patients.

The findings of this study emphasized on the judicial usage of acquisition imaging technique, stationary beam direction, and image magnification in order to reduce patient dose during a clinical interventional procedures. As mentioned earlier, patient's eye lens dose is highly subjected to the lateral tube projections. However, collimation of the radiation field of the lateral tube is the most effective method to minimise the irradiation dose to the left eye lens, when the interventionist needs to visualise the arterial system at anterior part of the patient's brain for diagnosis and/or treatment practices, collimation of the lateral tube is not possible. Therefore, the following chapter will propose an alternative method to reduce the patient's eye lens dose when it is positioned in direct radiation beam of the lateral tube.

CHAPTER 7: A METHOD TO REDUCE PATIENT'S EYE LENS DOSE IN NEURO-INTERVENTIONAL RADIOLOGY PROCEDURES

7.1. Introduction

Fluoroscopy guided neuro-interventional procedure is used to visualise the arterial system for diagnosis and treatment. Complex procedures involving prolonged radiation exposure might exceed the threshold dose for cataract formation. These procedures are mainly performed under biplane fluoroscopy units, whereby the lateral x-ray tube is generally utilised at one side of patient's head almost perpendicular to the patient's eye. Physical collimation is the most effective way of reducing the radiation dose to the patient's eye lens, but in instances where collimation is not possible, an attenuator may be useful in protecting the eyes. The purpose of this chapter is to design and fabricate an eye protector to reduce the patient's eye lens dose, while does not interfere with the clinical procedure. This chapter considers research objective 5, in order to study the radiation attenuation properties of the custom-made protector and its effects on image quality and exposure parameters.

7.2. Literature Review

Eye lens is one of the radiosensitive organs in the human body (Durchschlag *et al*., 1999). Among the different radiological modalities, computed-tomography (CT) scans of the head and neck (Siddle *et al*., 1990; Moulin *et al*., 1996; Niu *et al*., 2010) and fluoroscopy guided neuro-interventional procedure (Ilgit *et al*., 2000; Moritake *et al*., 2008; Sandborg *et al*., 2010) had been observed to pose a higher risk of cataract formation, especially among those with visual impairment, young patients, and patients who required multiple CT scans or prolonged neuro-interventional procedures. For CT scans, different techniques had been suggested to reduce the eye lens dose, such as

positioning the eyes outside the scanning region, angling of the gantry along the supraorbital meatal line (Heaney & Norvill, 2006; Matsubara *et al*., 2011) and using in-plane shields (Hopper *et al*., 2001; Heaney & Norvill, 2006). Bismuth-impregnated latex shield (F&L Medical Products, Vandergrift, Pa.) contains the heavy metal bismuth (equivalent to 0.45 $mg.cm^{-3}$ lead), which was particularly designed to reduce primary radiation dose to superficial organs, like eye lens, breast tissue, and thyroid gland during CT examinations. The ability of the bismuth shield in reducing radiation dose to the lens of patient's eyes was tested during 30 routine cranial CT examinations (Hopper *et al*., 2001). In this study, patients were classified into three groups: 1) patients with eyes protected with a single thickness of bismuth shield, 2) eyes protected with a double thickness of bismuth shield, and 3) eyes protected by a triple thickness of bismuth shield. This study showed that, the use of single, double, and triple bismuth shields reduced the average radiation dose up to 39.6%, 43.5%, and 52.8%, respectively, while there was no statistical difference found between single, double, and triple bismuth shielding in patient study. However, the review of artifacts projected into the brain revealed that no significant artifact caused by the eye shielding were observed into the brain region; using in-plane shielding caused significant artifact into the superficial orbit and the lens (Hopper *et al*., 2001). The artifact generated by the bismuth shield was evaluated during 127 patients underwent spiral CT scans of the paranasal sinuses in the axial plane. This study reported the relative increase in the CT number (HU) within the eyeball with the bismuth protection located on the patients' eyes was 180.6±17.7 HU, 103.3±11.7 HU, and 53.6±9.2 HU in 2 mm, 5 mm, and 9 mm beneath the skin level on the axial images, respectively. The average and standard deviation of eyeball density measured in three patients without the protection was reported 17.97± 3.7 HU (Hein *et al*., 2002). Heaney & Norvill reported that, angling the gantry along the supraorbital meatal plane in head scanning could reduce the

patient's eye lens dose by approximately 88% relative to the protocols which patient's eyes are placed in the radiation field. In other hand, using the bismuth eye shields could reduce the eye lens dose by up to 48% when the patient's eyes are placed in the radiation field and gave no significant lessening the eye lens when the gantry angled along the supraorbital meatal plane (Heaney & Norvill, 2006). Mukundan *et al.* tested the efficiency of the bismuth shield in reduction of radiation dose under different tube potentials, 100, 120, and 140 kVp. In this study, MOSFET detectors were used to measure radiation dose and a double layer of the Bismuth shield was placed 1 cm apart from the surface of the anthropomorphic pediatric phantom eyes. The average dose reduction to the eye globe was recorded to be 41%, 42%, and 39%, at 100, 120, and 140 kVp, respectively, and radiation dose of the eye lens reduced up to 45%, 25%, and 36%, at 100, 120, and 140 kVp, respectively (Mukundan *et al*., 2007).

However, using the bismuth shield could considerably reduce the patient's organ dose; but, the incidence of streak artifacts and dramatic degradations in image quality have been reported, when the bismuth layer is placed in contact with the patient's surface (Heaney & Norvill, 2006; K. Lee *et al*., 2010). In order to reduce the degradation of the image quality, the bismuth shield should be placed 1 cm apart from the patient's body and also applying automatic exposure control (AEC) systems could considerably help to maintain the image quality constant (Lee *et al*., 2010) and streak artifacts were not noted at 2 cm and 6 cm gaps of shielding to the surface distances (Kalra *et al*., 2009).

During interventional radiology procedures, unlike the CT examination, it is not practicable to block part of the radiation beam. The suggested protector should not significantly change the image quality and exposure parameters (kV and mAs). For these reasons it is essential to bear in mind that, a protective layer during an interventional radiology procedure should be able to attenuate part of the radiation

beam in order to reduce the patient's dose, not blocking the radiation, which causes loss of information in patient's image.

7.3. Materials and Methods

7.3.1. Eye Protector

In this chapter a custom-made eye protector was fabricated using polyurethane rubber (VytaFlex®40, Smooth-On, Inc., Easton, PA.). The polyurethane rubber due to its low viscosity can be easily poured into different mould shapes and also remains pliable without any structural change under the stress. It is very light and its attenuation properties can be simply modified by adding high and low density materials, like $CaCO_3$ and phenolic microspheres, respectively (Jones *et al*., 2003; Winslow et al., 2009). The mixture of the 10 g polyurethane with 1.5 g $CaCO_3$ was stirred until evenly mixed and left to set in a 50 mm diameter cylinder mould and the resulting eye protector was 16 mm thick. The elemental composition of the polyurethane rubber was analysed using a Scanning Electron Microscope (Quanta FEG 650; FEI, Hillsboro, OR, USA) attached to an Energy Dispersive x-ray Spectroscopy (EDS) analyser. The physical density of the eye protector was measured based on the theory of the buoyant force. More information about SEM-EDS system and buoyant force theory can be found in chapter 3.

The attenuation properties of the eye protector were calculated theoretically. Total mass attenuation coefficient of the material for various photon energies (15keV to 80keV) was derived from the XCOM photon cross-section database (NIST, 1999). The x-ray spectrum for different fluoroscopy and acquisition modes of a Philips Allura Xper FD20/20® unit (Philips Healthcare, Best, The Netherlands) was calculated using the SpekCalc x-ray spectrum generator program (Institute of Cancer Research London, UK). The SpekCalc x-ray spectrum generator is a software program, which can take the

x-ray tube specifications, like tube potential and anode angle, and produce an energy spectrum of the generated x-rays.

To evaluate the radiation attenuation properties of the eye protector material, the percentage depth dose (PDD) response was measured using the Philips Allura Xper FD20/20® biplane system. Square polyurethane rubber slabs (20 cm × 20 cm) were fabricated with different thicknesses for this measurement. The PDD responses were measured using a 0.055cm^3 Markus parallel plate ion chamber (model 23343, PTW, Freiburg, Germany). The Markus chamber was placed inside a special slot within a Solid Water® slab (Gammex 457, Gammex, Middleton, WI) and 12 cm thick of the Solid Water® was used as backscattering material. The polyurethane slabs were positioned 80cm away from the focal spot and exposed to 80 kVp (acquisition mode, 3 frame per second (3fps)) of radiation energy with a field size of 10 cm × 10 cm (Figure 7.1). As reported earlier in chapter 6, the survey of routine exposure parameters of 58 clinical neuro-interventional procedures revealed that the most frequent tube energy and frame rate of DSA imaging technique were 80 kVp and 3fps, respectively (52.4% and 50.1% of all DSA exposures).

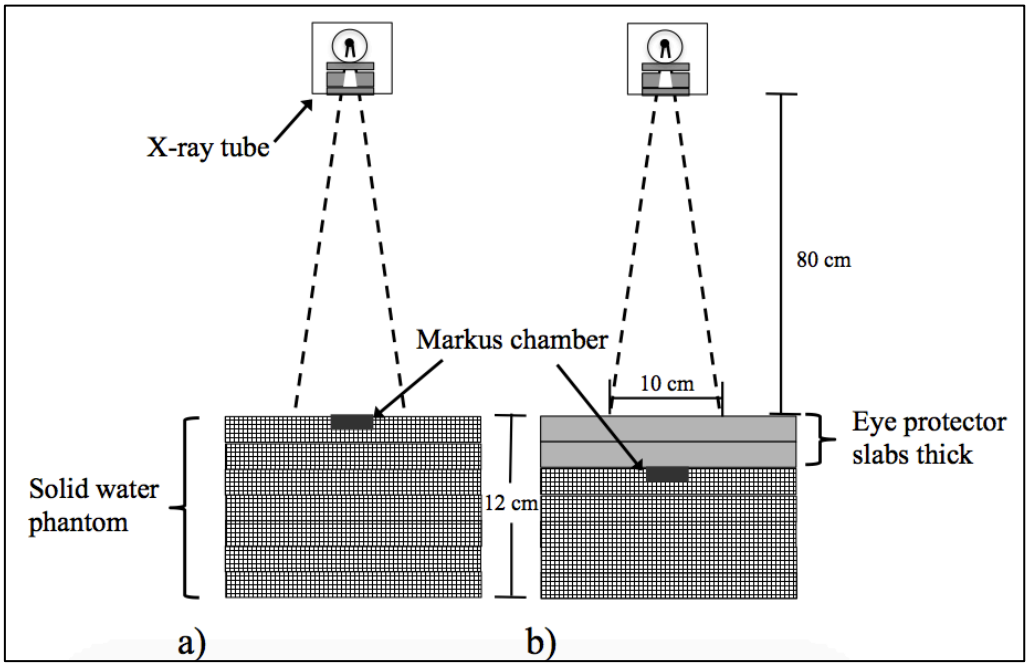

Figure 7.1 Diagram of the experimental setup of the PDD test. The percentage depth-dose curve was obtained by normalising the Markus chamber responses at different depth (from 1 mm to 30 mm) of the eye protector slabs (b) to its response at the surface of the Solid Water® phantom (a).

7.3.2. Phantom Study

The exposure parameters of a clinical aneurysm procedure were recorded and the procedure was replayed and simulated onto an adult female anthropomorphic phantom (ATOM, CIRS, Norfolk, VA). The effects of the eye protector on the radiation dose to the eye lens position and dose distribution over the head and eyelid region were studied using the Gafchromic® film (XR-RV3, ISP, Wayne, NJ).

The XR-RV3 film has been comprehensively characterised for beam qualities of 60–120 kVp, which offered this detector as a suitable and reliable dosiemtry system for patient's dosimetry during interventional procedures (McCabe *et al*., 2011). The XR-RV3 film has been used widely for evaluation of radiation dose distribution and patient's maximum skin dose during clinical interventional procedures (Bednarek *et al*., 2011; Tsai *et al*., 2014; Bordier *et al*., 2015).

In this chapter the XR-RV3 film was calibrated for an 80 kVp photon beam (effective energy 42.7 keV) using the Philips Allura Xper FD20/20® machine. The XR-RV3 film was placed on a 30 x 30 x 12 cm^3 Solid Water® phantom and the x-ray tube was positioned at gantry angle of 180º. Imaging field of view (FOV) was fixed at 48 cm, flat panel detector was placed at 120 cm from the x-ray tube, and field size of 10 × 10 cm^2 at the surface of the phantom was used. The calibration was benchmarked against a 0.055 cm^3 Markus parallel plane ion chamber (model 23343, PTW, Freiburg, Germany).

In order to study the radiation dose distribution over the patient's head during the clinical neuro-aneurysm procedure, a sheet of the XR-RV3 was cut to the geometry of the phantom and sandwiched between the phantom's slabs at the level of the eyes, and a piece of the XR-RV3 was (50 mm diameter) placed underneath the eye protector (Figure 7.2). The simulated interventional procedure was repeated with and without using the eye protector at the surface of the phantom's left eyelid. The human eyeball has limited rotational degrees of freedom. The medial and lateral oblique rectus lie in a horizontal plane and have primary actions of adduction and abduction, respectively, which allow a normal eye to rotate 45º to 50º in the horizontal plane from the primary eye position (Tasman & Jaeger, 2001). The effect of the eye protector on reduction of the eye lens radiation dose was studied by subtraction of the radiation dose distribution with and without the eye protector.

The film scanning was performed using an Epson 10000XL flatbed scanner (Epson Canada, Ltd., Toronto, Ontario, Canada) and captured images were analysed using Imagej 1.47 software (National Institute of Health, USA). Further explanation about the radiochromic film scanning can be found in chapter 3, section 3.3.

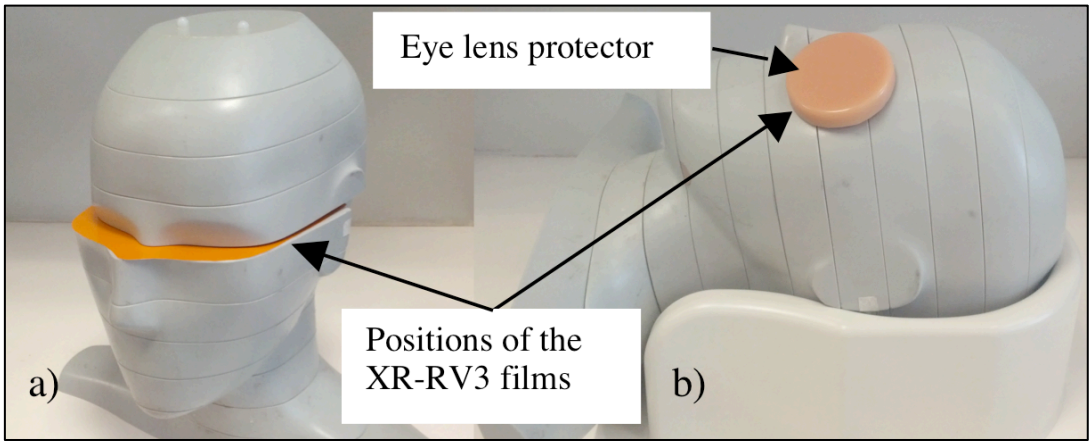

Figure 7.2 Photograph showing the XR-RV3 films positions, a) sandwiched within the anthropomorphic phantom's slabs at the positions of the eyes and, b) underneath the protector layer at the surface of the left eyelid.

7.3.3. Effect of the Eye Protector on Captured Image and Exposure Parameters

The magnitude of interference of the eye protector on image quality of exposure parameters was studied quantitatively and qualitatively. The visibility of the eye protector in fluoroscopy and DSA images and its level of interference on the diagnostic image quality were quantitatively studied by two experienced neuro-interventional radiologists. The effects of the eye protector on image quality were also studied quantitatively by measuring the changes of the images pixel values of the anthropomorphic phantom at the region of the eyeball with the placement of the eye protector on the phantom.

The effect of the eye protector on the automatic dose rate control (ADRC) was studied using fluoroscopy (low, medium, and high modes) and acquisition imaging techniques (0.5 fps, 2 fps, 3 fps, 4 fps, and 6 fps).

7.4. Results and Discussion

7.4.1. Design and Fabrication of the Eye Protector

The EDS test of the polyurethane component showed the material is comprises of carbon: 63.1%, oxygen: 19.6%, nitrogen: 10.8%, and calcium: 6.5%. The physical density of the eye protector was found to be 1.11 $g.cm^{-3}$. The attenuation properties of the eye protector were evaluated theoretically using XCOM software, comparing against the beam spectrum of the fluoroscopy procedures. The component total mass attenuation for photon energies of 15 keV to 80 keV was calculated using XCOM software (Figure 7.3a). The mass attenuation coefficient of the eye protector dropped dramatically from 2.9 $cm^2.g^{-1}$ at 15 keV to 0.33 $cm^2.g^{-1}$ at 40 keV followed by a plateau for higher photon energies. This showed that the eye protector could be efficiently utilised to absorb soft x-rays. Figure 7.3b shows the energy spectrum for selected commonly used fluoroscopic and acquisition modes. The ADRC system automatically applies various filtrations for the different exposure modes, resulting in the filtration of some of the lower photon energies. Despite the inherent filtration and additional filtration added by ADRC system, the beam spectrum still contained some portion of low-energy x-rays, which will be absorbed in superficial tissues, like skin.

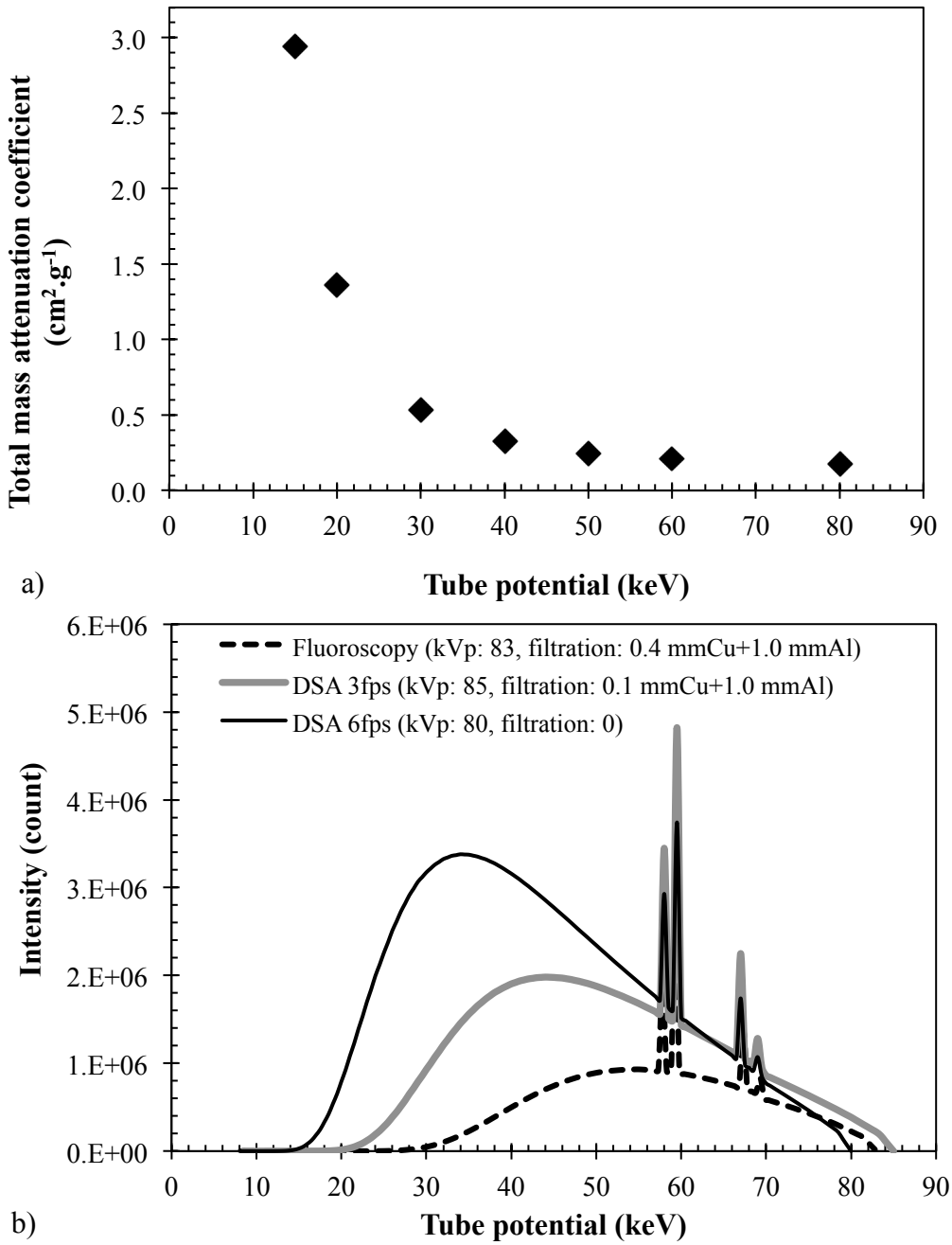

Figure 7.3 a) The total mass attenuation coefficient of the eye protector for low photon energies and, b) x-ray spectrum generated using the SpekCalc x-ray spectrum generator for different fluoroscopy and DSA exposure modes using the Philips Allura Xper FD20/20® unit.

Figure 7.4 shows the result of the eye protector PDD test. Radiation doses at different thicknesses of eye protector material were measured using the Markus chamber. This study showed that at the thickness of 16 mm, the eye protector

attenuates 20% of the radiation. Based on the attenuation rate of the eye protector medium and effect of this material on images, a judicious decision was taken to propose 16 mm of the polyurethane mixture as a patient's eye protector during neuro-interventional procedures.

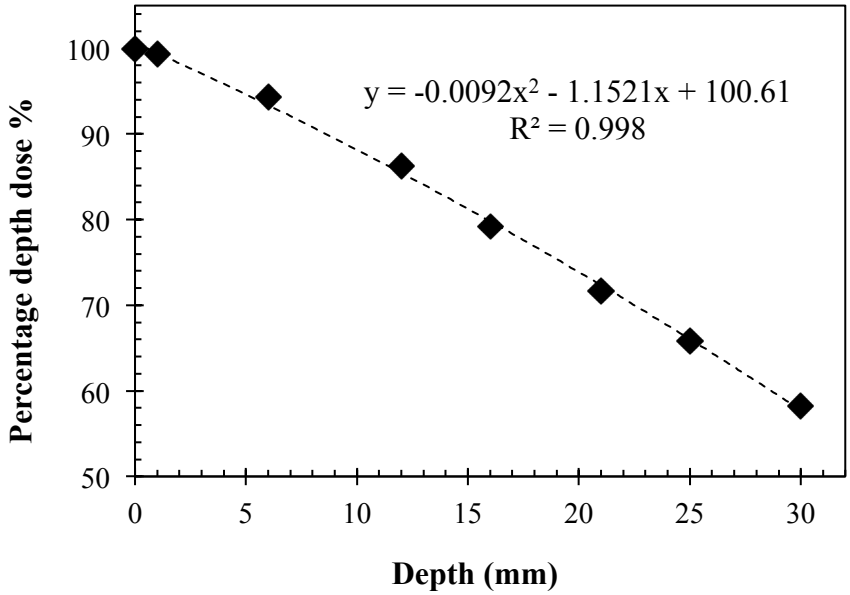

Figure 7.4 Radiation dose penetration through the polyurethane rubber at different depths using an 80 kVp photon beam (effective energy 42.7 keV).

7.4.2. Effect on Dose Distribution

The XR-RV3 film was calibrated for 80 kVp photon energy using the Philips Allura Xper FD20/20® machine, which showed increase of the XR-RV3 film optical density perfectly fitted on a second-degree polynomial curve (Figure 7.5). The average and standard deviation of the coefficient of variations of the XR-RV3 film pixel values for different dose ranges (1.3 cGy to 140 cGy) was found to be 0.25% and 0.02%, respectively.

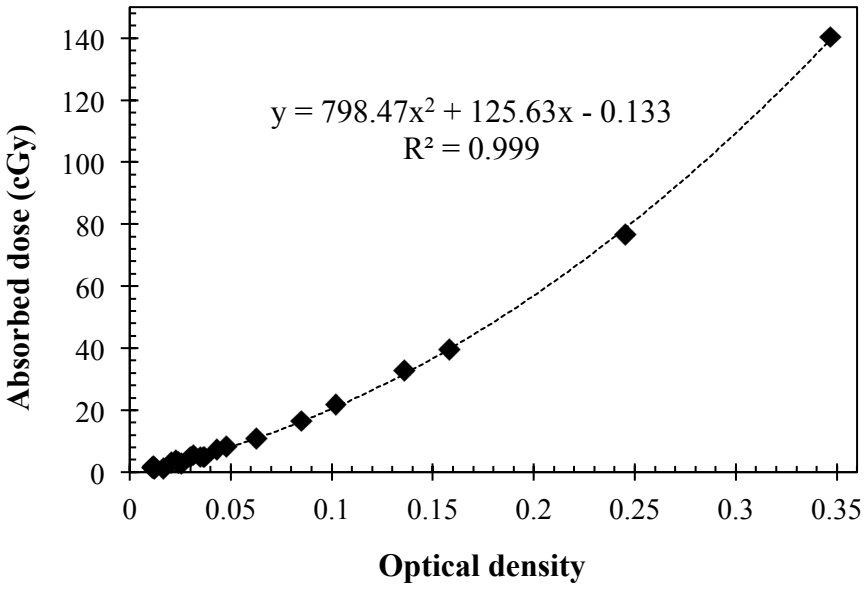

Figure 7.5 The calibration curve of the Gafchromic® RV-RV3 film for 80 kVp photon beams.

Figure 7.6 shows the photograph of the anthropomorphic phantom cross-section and the 2D dose distribution of the radiation dose over the patient's head with and without the eye protector. The subtracted radiation dose distribution with and without the eye protector revealed that, the eye protector could reduce the eye lens dose up to 62.1% (from 93.6 to 35.5 cGy) (Figure 7.7c). However the effect of eye protector is highly depends on location of the lens, due to limited horizontal rotation of the eyeball (about 45º from the primary position (Tasman & Jaeger, 2001)), the eye protector could efficiently reduce the radiation dose throughout region (over 10%).

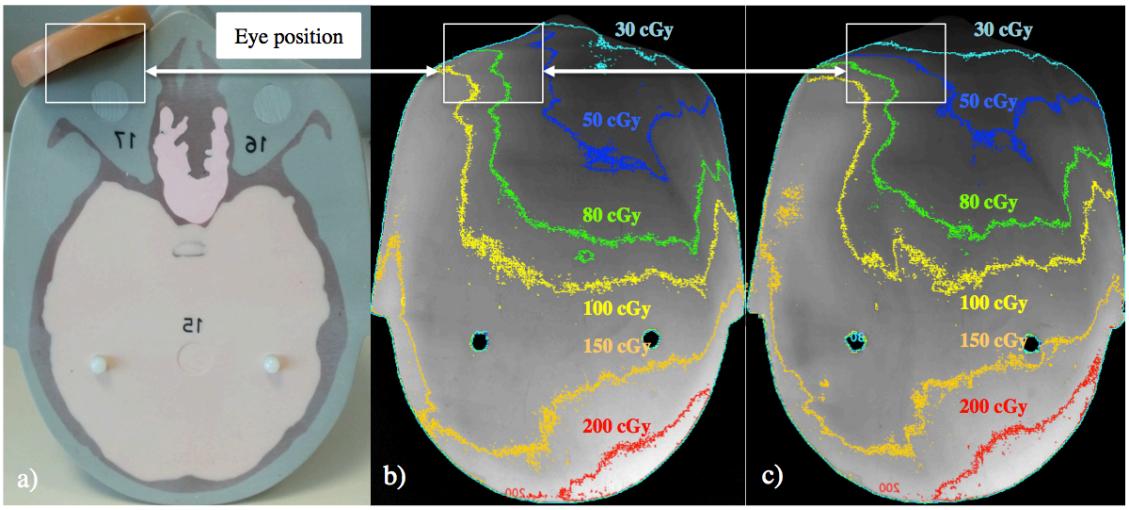

Figure 7.6 Photograph showing the cross-section of the anthropomorphic phantom with the eye protector placed on the left eye lens (a), scanned images of 2D dose distribution measured using Gafchromic® XR-RV3 films without (b), and with the eye protector (c).

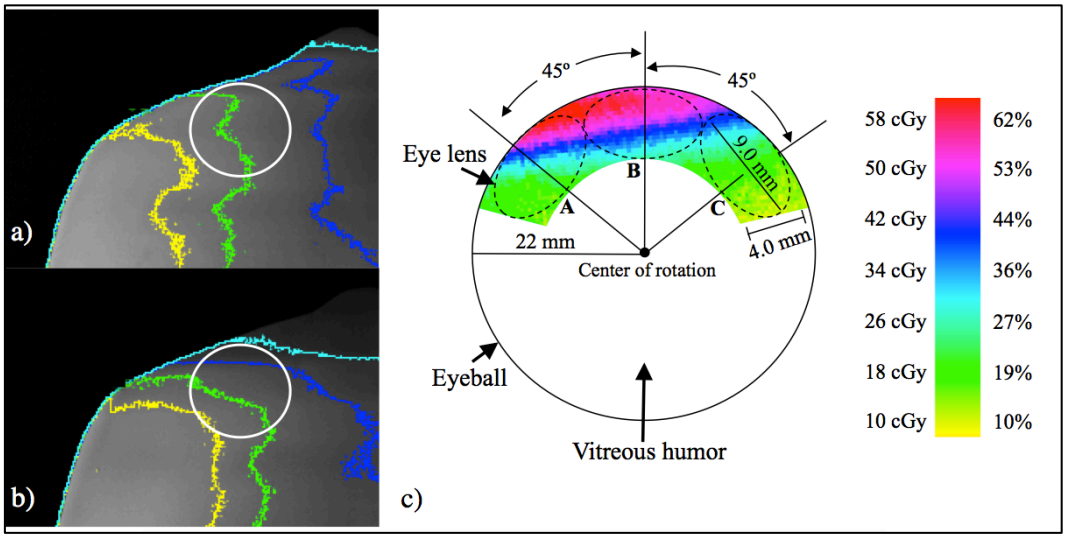

Figure 7.7 The radiation dose distribution over the phantom's left eye (22mm in diameter) without (a) and with (b) the radiation protection layer. The subtracted image of the radiation dose distributions over the eyeball with and without using the eye protector layer, which shows the dose reduction in colour bar, based on dose unit (cGy) and percentage of dose reduction (c). The eye lens physical size was sketched with 4.0 mm in thick and 9.0 mm in length (Valentin, 2002).

Figure 7.8 clearly shows that there is a high dose gradient across the eyelid, which is contributed largely by the direct incident beam from the lateral x-ray tube. Study on the effects of the protective layer on the eyelid showed this protector considerably reduced the maximum eyelid dose by up to 23.3% (from 115.1cGy to 88.2cGy) and also reduced the entrance radiation dose to the left eye by up to 57.1% (from 70cGy to 30cGy).

One may note that although based on the PDD study, the 16 mm eye protector was able to reduce radiation dose by 20%. However, the dose reduction measured in a simulated clinical case showed a higher dose reduction (57.1%). This may be explained by the fact that the eye protector was mostly attenuating the incident beam from the lateral x-ray tube. Therefore, when placed on top of the patient's left eyelid, the lateral beam traverses a larger distance through the eye protector (~ 29 mm) before reaching the patient eyelid (Figure 7.9).

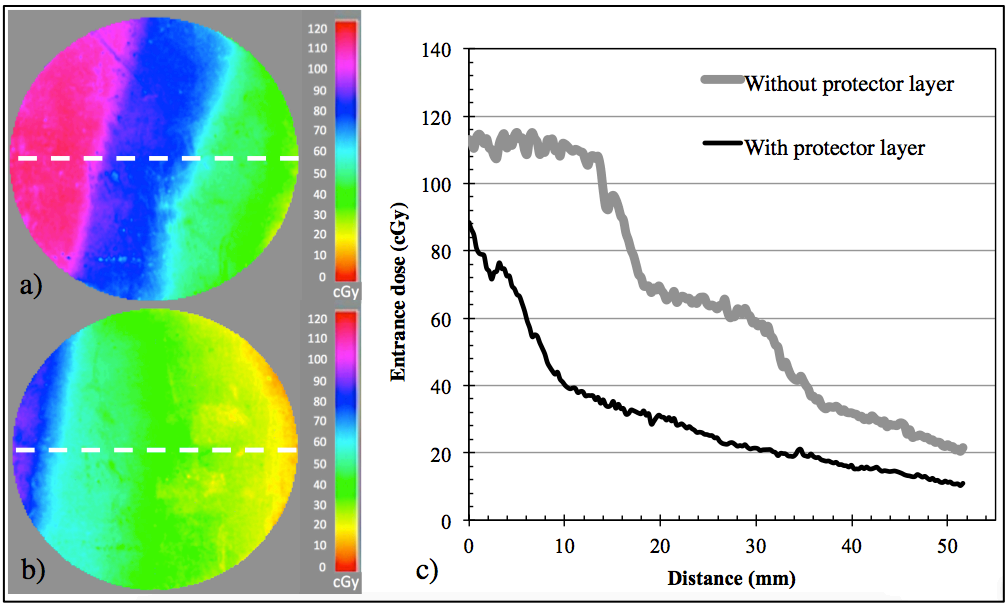

Figure 7.8 The radiation dose distribution over the left eyelid without (a) and with (b) the radiation protection layer. The radiation dose profiles with and without the eye protector (c).

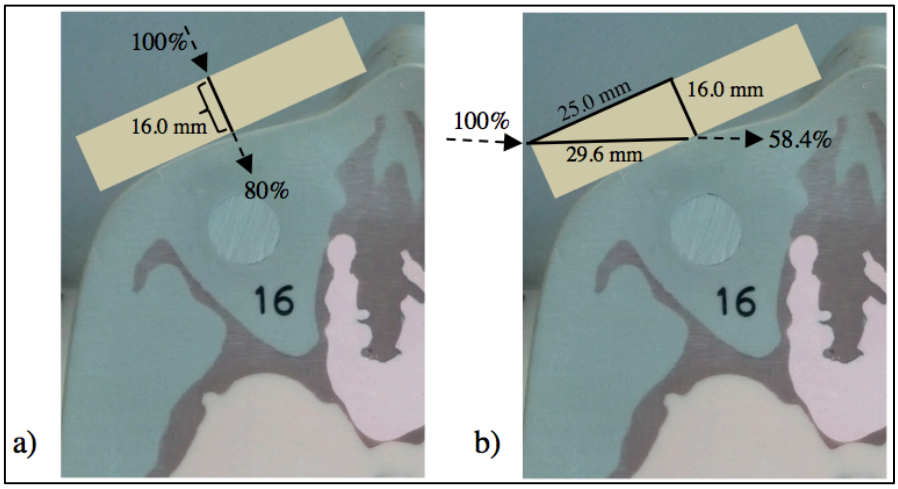

Figure 7.9 The attenuation range of the lateral tube radiation by using the protector later, a) when the radiation is perpendicular to the protector and b) when the radiation comes from the side.

Further investigation into the rotation and angulation of the x-ray tubes for the clinical aneurysm procedure revealed that the frontal tube was most frequently utilised at 0º (under the treatment couch) and a certain angle at right side of the patient's head (37º left anterior oblique (LAO)). The lateral tube was constantly positioned at left side of the patient's head (90º right anterior oblique (RAO)) throughout this procedure (Figure 7.10a). Both frontal and lateral tubes angulation (Cranial (CR)-Caudal (CA)) did not change considerably and been positioned repetitively at 0º (Figure 7.10b). These findings are in a good agreement with our earlier study on survey of the 58 neuro-interventional procedures, which were presented in chapter 6, section 6.4.5.

These findings explain the dose distribution measured by the film during the aneurysm procedure (Figure 7.6), which shows higher dose levels at occipital and left side of the phantom's head. The average and standard deviation of the tubes potential of the fluoroscopy imaging were found to be 78.7±3.5 kVp and 74.9±2.3 kVp for the frontal and lateral tubes respectively. The frontal and lateral beam energies during acquisition imaging (DSA) were changed within 84.9±4.9 kVp and 82.6±2.9 kVp, respectively.

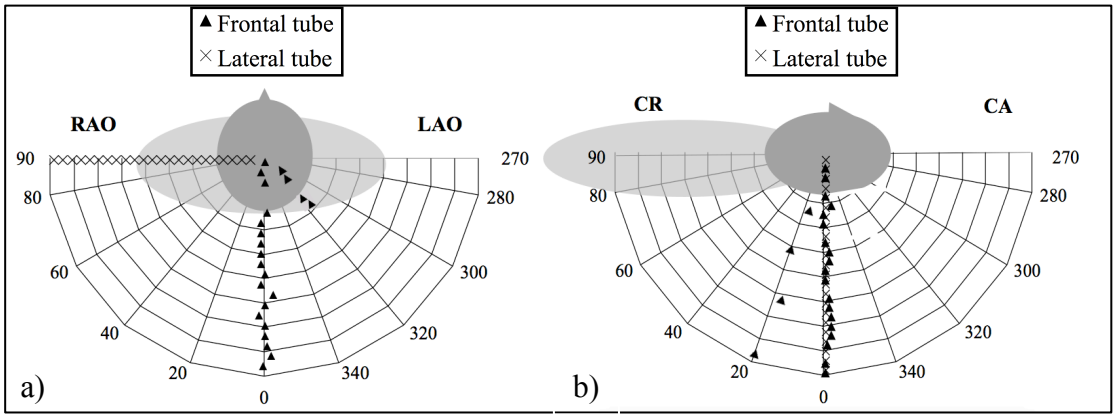

Figure 7.10 Diagram of the frontal and lateral tube rotations (a) and angulations (b) during the aneurysm procedure.

7.4.3. Effect of Eye Protector on Image Quality and Exposure Parameters

The eye protector could be seen faintly on the fluoroscopic images (Figure 7.11), but was completely invisible on the DSA images due to image subtraction (Figure 7.12). For qualitative evaluation, the two interventional radiologists rated the interferences of the eye protector's shadow on the fluoroscopy image as minimal and would not interfere with their clinical performance. The effects of the eye protector on fluoroscopy images were also studied quantitatively. This study revealed that the eye protector increases the image pixel value (0-255) up to 11.97 ± 1.48 (4.69% ± 0.58%). The eye protector did not alter the tube potential (kV) but did slightly increase the tube current (mA) during fluoroscopy imaging and tube current-time product (mAs) during DSA imaging. The maximum increase in the tube current during fluoroscopy imaging was 0.4 mA (3.7%) and maximum increase in the tube current-time product during DSA imaging was 4 mAs (8%) (Table 7.1).

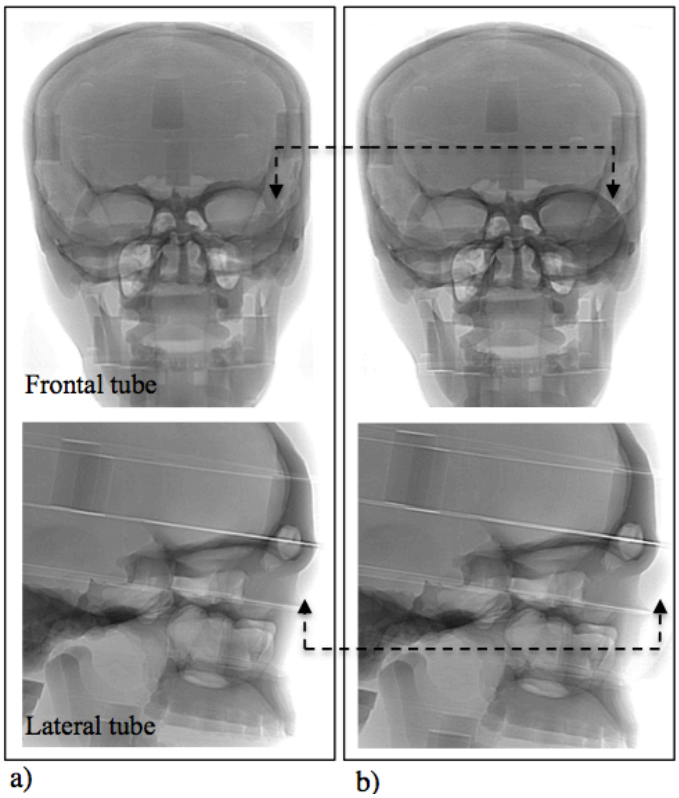

Figure 7.11 Effect of the protector layer on fluoroscopy images from the frontal and lateral tubes of the phantom head without eye protector (a) and with eye protector (b).

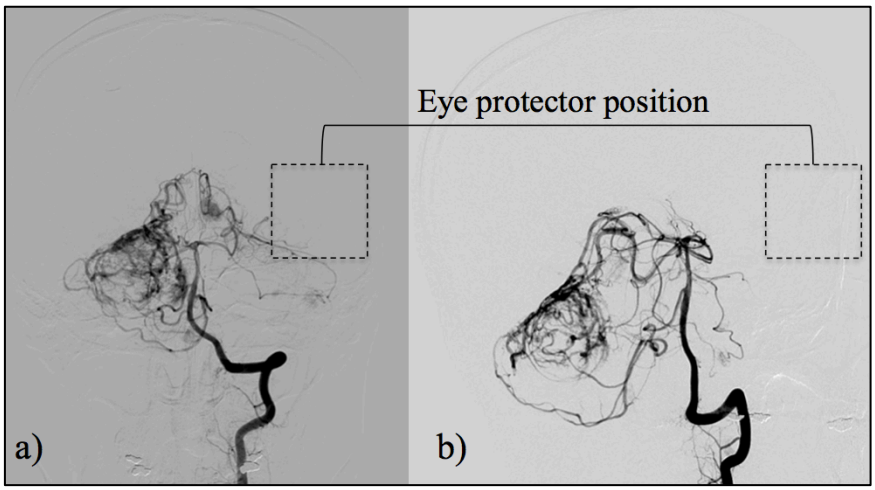

Figure 7.12 Effect of the protector layer on DSA images during a clinical cerebral angiography procedure from the frontal (a) and lateral (b) tubes with eye protector on the left eyelid.

Table 7.1 Effect of the protector layer on exposure parameters during fluoroscopic and DSA imaging techniques.

Exposure type	Mode		Frontal		Lateral	
			kV	**mA**	**kV**	**mA**
Fluoroscopy	**Low**	With	83	12.1	80	4.9
		Without	82	12.1	80	5.0
	Medium	With	75	15.6	67	11.1
		Without	75	15.1	67	10.8
	High	With	74	10.7	66	6.3
		Without	74	10.3	66	6.3
			kV	**mAs**	**kV**	**mAs**
DSA	**1fps**	With	85	16	85	5
		Without	85	15	85	5
	2fps	With	80	54	80	16
		Without	80	50	80	16
	3fps	With	85	39	85	12
		Without	85	36	85	12
	4fps	With	85	16	85	5
		Without	85	15	85	5
	6fps	With	80	22	80	6
		Without	80	22	80	6

7.5. Chapter Summary

This chapter illustrated the design and fabrication process and testing of an eye protector for patients undergoing neuro-interventional procedures (research objective 5). Complex neuro-interventional procedures are commonly performed using biplane angiography units. This could result in unintended radiation dose injury to the eye lens. Collimation of the lateral tube is the most effective method to reduce radiation dose to patient eye lens. In the situation where the application of collimation is not possible, a protective layer that serves to attenuate direct radiation beam can be useful to reduce

the radiation dose to the eye lens. In this chapter, a custom-made eye protector was fabricated to achieve this purpose. This chapter showed that, the presence of the eye protector has minimal effects on the ADRC exposure parameters and image quality but was effective in attenuating the direct radiation exposure from the lateral tube and thereby reducing the eye lens dose.

In this chapter, impacts of the eye protector on patient's eye lens dose were only tested for a randomly selected aneurysm procedure, which can be considered as one of the limitations of this study. Moreover, the commercially available anthropomorphic phantom do not have a particular design for eyeballs and generally consider human eyeball as a homogenous organ with the same attenuation properties with soft tissue, which can potentially cause an additional uncertainty for this study and also former researches those have performed with anthropomorphic phantoms to address the radiation dose received by the patient's eye lens dose. For this reason, the necessity of further study on this issue was felt, in order to design and fabricate an anthropomorphic phantom comprising different parts of the human eyes and organs with closer attenuation properties to actual structures than current anthropomorphic phantoms. The finding of this research will be presented in the following chapter.

CHAPTER 8: ASSESSMENT OF PATIENT'S EYE LENS DOSE USING A CUSTOM-MADE ANTHROPOMORPHIC HEAD PHANTOM

8.1. Introduction

Anthropomorphic phantoms have been used widely in radiation dosimetry studies. These phantoms are constructed from different tissue-equivalent materials, modeling actual organs physical shapes and also attenuation characteristics. In commercially available anthropomorphic phantoms such as RANDO® (Alderson Research Laboratories Co., Stanfora, CN) and ATOM® (model 702; CIRS, Norfolk, Va) there is no particular design for the eye and it is considered as a homogenous organ with the same tissue substitute with soft tissue, which cannot be a precise representative of actual human eye.

The purpose of this chapter therefore was to address research objective 6 to design and fabricate a custom-made anthropomorphic phantom, which provides greater options for dosimeter placement at different depths of the eyeball. The phantom will be used to evaluate patient's eye lens dose during fluoroscopy guided neuro-interventional procedure.

8.2. Literature Review

In general, phantoms used in diagnostic radiology can be categorised based on their functions and applications into two classes as imaging or dosimteric (White, 1993; Jones *et al*., 2006). Imaging phantoms are primary tools to assess image quality in order to optimise acquisition protocols, resulting in concomitant decreases in radiation dose to the patients. Dosimetric phantoms are used to assess absorbed dose in the patient's body during a clinical procedure. The dosimteric phantoms are generally constructed with several tissue substitute materials, which are mainly chosen based on patient's characteristics, like gender and age. White in 1993 reported the change of the various

tissue compositions (water, protein, lipid, etc.) with age for fetus to adult male and female patients (White, 1993). This study clearly indicated the importance of considering age and sex in construction of dosimteric phantoms.

Keinbock has initiated the search on tissue-equivalent materials in 1906 by proposing water as a substitute material for human muscle. Since that time, various materials have been proposed for construction of body phantoms, like epoxy resins (White *et al*., 1977), polyurethane (Griffith *et al*., 1979), polystyrene (White, 1978), and polyethylene (Hermann *et al*., 1985). The International Commission on Radiation Units and Measurements (ICRU) report 44 listed down radiation characteristics, mass and electron densities, and elemental compositions of 62 tissue-equivalent materials (Griffiths, 1989).

Jones *et al.* in 2003 presented a series of tissue-equivalent materials to specifically mimic newborn soft tissue, bone tissue, and lung tissue using epoxy resin base materials (Jones *et al*., 2003). Phenolic microspheres and various fillers were utilised in order to adjust their mass densities and x-ray attenuation coefficients, respectively. The test on tissue equivalency of the fabricated newborn tissue-equivalent materials showed yield estimates of absorbed dose at depth (4 cm) to within 3.6% for soft tissue, 3.2% for bone tissue, and 1.2% for long tissue in correspond to the doses assigned to reference newborn tissues reported by Oak Ridge National Laboratory (ORNL). This study was followed by a new method for construction of a tomographic physical phantom for newborn patient based on patient's CT image set, using the corresponding tissue-equivalents of newborn organs (Jones *et al*., 2006). In a new attempt at anthropomorphic phantom construction urethane-based compounds, combined with $CaCO_3$ and poly-fil polystyrene micro beads, were used to mimic the human soft-tissue and lung, respectively. The polyurethane based materials were chosen to improve phantom's pliability and durability under the stress and also is constructed in a 5 mm slice thickness

in order to offer easier dosimeters accommodation for *in-vivo* patient's dose measurement (Winslow *et al*., 2009).

There are several commercial anthropomorphic phantoms, which are fabricated from various tissue mimicking materials, represent the anatomical shape of human organs and provide similar attenuation characteristics to those of real human organs for radiation dosimetry purposes according to their age and gender categories. Evaluation of the organ doses using an anthropomorphic phantom provides several advantages over computational methods, since during a clinical procedure the photon energy spectrum and irradiation geometry are varied continuously, which make computational methods very complicated. The anthropomorphic phantoms mainly imitate the human organs with three tissue equivalent materials for bone, soft tissue, and lung.

One of the common limitations of all anthropomorphic phantoms is, in these phantoms there is no particular design for phantom eye lens and in general the eyeball is considered as a homogenous organ with same tissue substitute with soft tissue. The ICRU in 1989 reported the eye lens and soft tissue mass attenuation coefficients (Griffiths, 1989). The comparison between mass attenuation coefficients of the eye lens and soft tissue showed that although there is a negligible difference (less than 1%) for beam energy over 100 keV, the difference between their mass attenuation coefficients nonetheless become noticeable (over 22%) in lower energies than 10 keV (Figure 8.1).

Of particular interest for this chapter is the use of anthropomorphic phantoms for measuring radiation dose at the patient's eye lens. This chapter also proposes to use three-dimensional (3D) printing technique to construct a custom-made anthropomorphic head phantom for radiation dosimetry purposes, allowing the fabrication of precise anatomical shapes and suitable radiation attenuation characteristics.

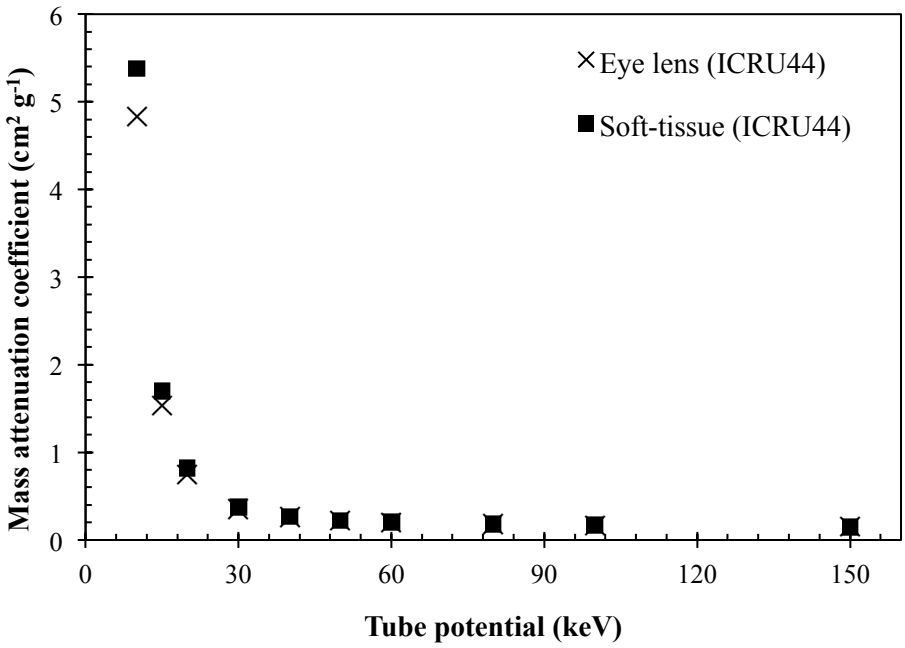

Figure 8.1 The mass attenuation coefficients of the human eye lens and soft tissue based on the ICRU44 report (Griffiths, 1989).

8.3. Material and Methods

In general this chapter includes four steps. The first step is the study of the attenuation properties of the various organs in the human head based on measurements and published data in reference books (e.g. (Griffiths, 1989)). The second step, investigates attenuation properties of the various tissue substitute materials based on their elemental compositions, CT-numbers, physical densities, effective atomic number, and mass attenuation coefficients.

The third step is the fabrication of an anthropomorphic head phantom using new tissue mimicking materials and last step is using this phantom for evaluation of patient's eye lens dose during a neuro-interventional procedure.

8.3.1. Determination of the Properties of the Human Eye Lens

The CT number of human eye lens was determine by evaluating a sample of CT images of 13 patients who underwent CT examination procedures were considered in order to evaluate CT-number of various human organs, like brain, skull, and eye (cornea, lens, and vitreous humor). All cases were examined under head and neck imaging protocol (120 kV) using a dual energy CT-scanner (SOMATOM Definition, Siemens Healthcare, Forchheim, Germany) at the University of Malaya Medical Centre (UMMC). The extracted DICOM images were studied using an open source medical image processing software, OsiriX version 5.7.1 (OsiriX Medical Imaging Software; http://www.osirix- viewer.com).

8.3.2. Determination of the Properties of tissue substitute materials

Selected tissue substitute materials were evaluated in terms of their CT numbers, elemental compositions by relative weights, physical densities, effective atomic numbers, and their linear attenuation coefficients (μ).

Polyurethane rubber (VytaFlex 40, Smooth-On, Inc., Easton, PA, USA) mixed with different ratios of calcium carbonate ($CaCO_3$) was studied as a substitute material for different parts of the eye. Calcium sulphate hemihydrate (plaster of Paris; $CaSO_4 \cdot 2H_2O$) was evaluated as a bone tissue-equivalent substitute, and polyacrylamide component was tested as a substitute material of the brain. CT-number of each sample was obtained using the SOMATOM Definition CT-scanner using the head and neck imaging protocol (120 kV).

The elemental composition by relative weights of all materials were analysed using a SEM-EDS machine (Quanta FEG 650; FEI, Hillsboro, OR, USA) at 30 keV electron beam. The XCOM photon cross-section database (NIST, 1999) was used to obtain the mass attenuation coefficient of the materials. Furthermore, density of each component was measured based on theory of the buoyant force using the mass balance technique.

The linear attenuation coefficient (μ, cm^{-1}) of each material was calculated by multiplying the mass attenuation coefficient ($\frac{\mu}{\rho}$, $cm^2.g^{-1}$) to the substance's density ($\rho =$ $g.cm^{-3}$).

The μ of each component was verified by an experimental measurement. The experimental measurement was carried out using a technetium-99m radionuclide (Tc^{99m}) as a mono-energetic source (gamma rays: 140.5 keV, 98.6%) and photons were counted by a gamma camera (BrightView SPECT; Philips Nuclear Medicine, Milpitas, CA, USA) (Figure 8.2). The transmitted photons were counted for 60 s for each measurement. The distance between radiation source and image detector was fixed to 70 cm and energy window of gamma camera set to ± 5% of the main photon energy (140.5 keV) in order to remove low energy scattered photons from the total number of counts. Each tissue substitute material was fabricated in the form of slabs with dimensions of 10 × 10 cm^2 with various thicknesses and the linear attenuation coefficient for each material was calculated using the Bouger–Lambert–Beer law following the equation below (Eq. 8.1) (Johns & Cunningham, 1983)

$$I = I_o e^{-\mu x}, \qquad \text{Eq. 8.1}$$

where I_o is the initial photon intensity, I is the intensity of the photon after passing through medium, x is the thickness of the attenuator, and μ is the linear attenuation coefficient for that particular material. These results have been compared with a reference report of ICRU44.

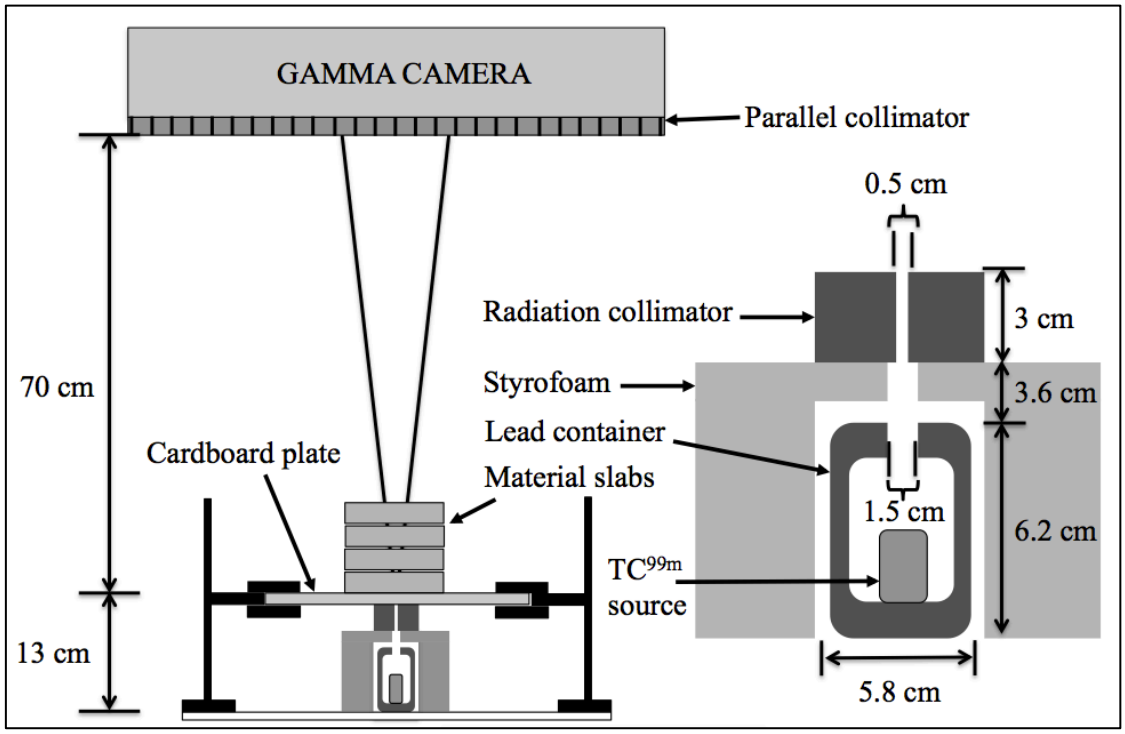

Figure 8.2 A block diagram of the measurement setup using TC^{99m}, lead container, Styrofoam, varying thicknesses of phantom materials, and the gamma camera. This study shows the attenuating property of each sample by considering the transmission rate of the gamma rays passing through the slabs.

The effective atomic number, Z_{eff}, generally reflects x-ray and gamma ray interactions with matter, which is used for dosimetric properties. The Z_{eff} can be calculated using different approaches like single value XMuDat computer program (Nowotny, 1998). This method produces a single value for a component effective atomic number based on the following formula (Eq.8.2)

$$Z_{eff} = \sqrt[m]{f_1 \times (Z_1{}^m) + f_2 \times (Z_2{}^m) + f_3 \times (Z_3{}^m) + \cdots}\ , \qquad \text{Eq. 8.2}$$

where f_n is the weight fraction contributions of each element in the composition and Z_n is the element atomic number. The m is a constant, which is generally set to 3.6 for components with $Z_{eff} < 6$ and 4.1 for components with $Z_{eff} > 6$ (Jackson & Hawkes, 1981). The same concept has been used by Khan *et al*. in 1994, which based on their practical findings proposed m= 2.94 for calculation of the Z_{eff} of a composition (Khan &

Gibbons, 1994). A single number cannot precisely represent the effective atomic number of a material, since this parameter highly depends on photon interaction cross-section per atom (σ_i) and its corresponding photon energy (Eq. 8.3) (Manohara *et al*., 2008)

$$Z_{eff} = \frac{\sum_i^n f_i \sigma_i}{\sum_j^n (\frac{f_j \sigma_i}{Z_j})}$$

$$= \frac{\sum_i^n f_i A_i (\frac{\mu}{\rho})_i}{\sum_j^n (\frac{f_j A_j}{Z_j})(\frac{\mu}{\rho})_j}, \qquad \text{Eq. 8.3}$$

where σ_i is the total photon interaction cross-section per atom and is proportional to its mass attenuation coefficient ($\sigma_i = \frac{A_i}{N_A} \times (\frac{\mu}{\rho})_i$). The f_i is elemental fraction in the compound, μ is linear attenuation coefficient, ρ is density, A is atomic weight, Z is atomic number, and N_A is the Avogadro constant (Manohara *et al*., 2008). The mass attenuation coefficients $(\frac{\mu}{\rho})_i$ and interaction cross-sections (σ_i) were obtained from XCOM computer program available online from the NIST website (NIST, 1999). Effective atomic number (Z_{eff}) of each substances and different human organs (based on their elemental compositions reported by ICRU44) were calculated based on the components elemental photon interaction cross-sections for 140.5 keV photon beam.

8.3.3. Fabrication of an Anthropomorphic Head Phantom

This step comprises of two stages, first, evaluation of average physical size of human eye's compounds (eyeball, eye lens, vitreous humor, and cornea-anterior chamber) for 13 patients. The second stage was to fabricate an anthropomorphic phantom using suitable tissue substitute materials.

8.3.3.1. Bone Tissue-Equivalent Substitute

The bone tissue-equivalent substitute used was the calcium sulphate hemihydrate (plaster of Paris; $CaSO_4 \cdot 0.5H_2O$). Plaster of Paris has been widely used as a bone tissue equivalent phantom for *in-vivo* bone lead measurement for over two decades (Somervaille *et al*., 1988; Todd, 2000; Nie *et al.*, 2011).

Construction of the skull was carried out using a 3D printer (ZPrinter 450®, Z Corporation, Burlington, MA, USA). 3D printer is able to create 3D model from DICOM image. In this study a physical model of a human skull was printed using a high performance calcium sulphate hemihydrate powder (ZP®151) based on the CT scan of a 60 year old male patient. The 3D-printed phantom was sprayed with a fine mist of salt water (magnesium sulphate heptahydrate) to seal and strengthen the printed structure (sealing process can be found at (3DSystems, 2013a)).

8.3.3.2. Tissue-Equivalent Substitutes of Eye's Compartments

The polyurethane rubber mixed with $CaCO_3$ powder was used to fabricate different parts of human eye. The idea of using mixture of the polyurethane and $CaCO_3$ as a substitute material for human soft tissue has been proposed by Winslow and his colleagues in 2009 (Winslow *et al*., 2009).

Study on 13 head-neck CT-scans helped us to investigate the actual physical shapes of different sections of the human eyes (cornea-anterior chamber, lens, and vitreous humor). Each section of the eyeball was fabricated individually according to the average physical dimensions found from the patients' CT images. For the eyeball (vitreous humor), a plastic ball with 2 cm diameter was used as a mould. The mixture was left to set resulting in a 2 cm eyeball. For other eye sections proper polyurethane mixture and suitable moulds according to their physical shapes have been utilised.

8.3.3.3. Brain Tissue-Equivalent Substitute

The brain was made using polyacrylamide. Polyacrylamide is the most popular material for construction of thermal phantom especially high intensity focused ultrasound (HIFU), due to its high melting point, high formability, optical transparency, and wide range of electrical, thermal, and acoustical properties (Dabbagh *et al*., 2014a). The acrylamide-based polymers have also been used for ultrasonic elastography (Ling *et al*., 2010), needle–tissue interaction (Datla *et al*., 2014), and for simulation of human soft tissue in radiofrequency and microwave frequency ranges (Bini *et al*., 1984; Surowiec *et al*., 1992).

In this study, the polyacrylamide was utilised to fabricate a substitute tissue for human brain. The main reasons for using polyacrylamide as a brain substitute material rather than using polyurethane even having almost the same CT-number and attenuation property, were its high uniformity and fast hardening (shaping) process. Polyurethane showed slightly inhomogeneity eventually for big samples and the drying process of the inner layers of this component for large size samples is considerably slow. The brain substitute material was made using 0.2 g ammonium persulphate, Tetramethylethylenediamine, 0.04 g N-N- Methylenebiascrylamide, and 6 g acrylamide-monomer dissolved in 100 mL water. This phantom has been recently introduced as a thermal phantom for hyperthermia and thermal ablation procedures (Dabbagh *et al*., 2014b). The 3D printed skull was used as mould for making a brain. The cranial cavity was filled by the polyacrylamide and was left to set for a few minutes. Polyacrylamide is generally a water-based polymer, which needs to be sealed to avoid water evaporation. The brain phantom was removed from the skull and sealed with a thin plastic sheet.

8.3.4. Evaluation of Patient's Dose

The application of the fabricated phantom was tested using the Philips Allura Xper FD20/20® biplane system in order to explore the radiation dose distribution over the patient's eye when a perpendicular radiation beam exposes the patient's eyeball. The radiation dose was measured using the Gafchromic® XR-RV3 film. The head phantom was positioned on the treatment couch and the frontal x-ray tube was positioned at 0º (posterior-anterior projection) and 180º (anterior- posterior projection) in order to study the radiation dose penetration throughout the patient's eyeball. The XR-RV3 films (with area size of 8 mm × 8 mm) were placed on selected positions to measure entrance and exit dose of the cornea, exit dose of the lens, and the radiation dose level at the retina position (Figure 8.3). The phantom was exposed with 80 kVp exposure beam (effective energy of 42.7 keV) using a 3fps acquisition mode imaging technique for 30 s.

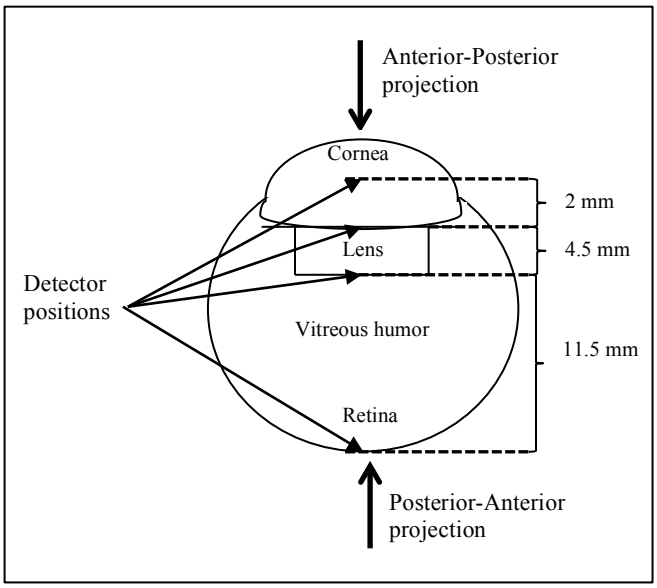

Figure 8.3 Diagram of the XR-RV3 films positions at defined depths of the eyeball and directions of x-ray projections.

8.4. Result and Discussion

8.4.1. Properties of the Eye Lens

It was found that the lens is denser than other parts of the eyeball (Figure 8.4 & Table 8.1). The polyurethane rubber was used as substitute for the eye components. Polyurethane was mixed with various ratio of the $CaCO_3$, in order to achieve different CT-number levels. In the first stage the CT-number of each medium was investigated. As expected as the weight of the $CaCO_3$ increases, the CT-number of the medium increases linearly (Figure 8.5).

Table 8.1 The average and standard deviation of 13 patients' organs CT-numbers, including different parts of human eyeball, brain, and bone.

Age	CT-number (HU)				
	Lens	Vitreous	Cornea-anterior chamber	Brain	Bone
47.5±11.3	102.1±10.4	10.1±4.5	31.7±4.2	37.3±4.5	983.7±254.4

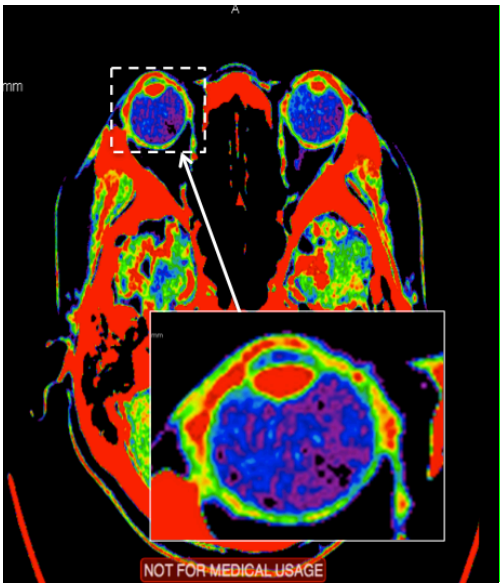

Figure 8.4 The cross-section view of a CT image of a patient's head displayed by the OsiriX software.

8.4.2. Properties of tissue substitute materials

In the second stage, the SEM images of different samples were taken (Figure 8.6) and EDS test was performed to evaluate the elemental composition of the each sample relative to their physical weight (%) and atomic weight (%) (Table 8.2). The elemental distribution maps were also recorded for each sample (Figure 8.7). The Z_{eff} of each component and different human organs based on the components elemental photon interaction cross-sections of a 140.5 keV photon beam were calculated based on Eq.8.3 (Table 8.2). This study showed that the polyurethane compositions have slightly higher Z_{eff} in compared with the effective energies of the eye lens and soft tissue.

In addition, the elemental compositions of different mediums were fed into the XCOM photon cross-section database and this software calculated the mass attenuation coefficient of each particular sample for various energy ranges. Figure 8.8 shows the mass attenuation coefficient of four polyurethane samples (mixed with 0.75 g, 1.5 g, 2 g, and 2.5 g of $CaCO_3$ powder). The comparison between mass attenuation coefficients of the polyurethane samples mixed with 0.75 g and 2.5 g $CaCO_3$ showed that although there is a negligible difference (less than 1%) for beam energy over 100 keV, nonetheless become noticeable in lower energies (over 15%) for energy less than 50 keV (Figure 8.8).

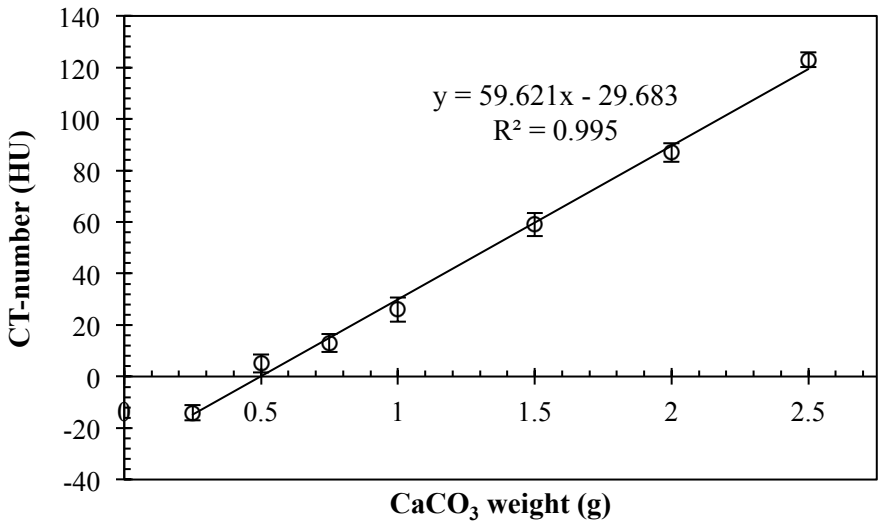

Figure 8.5 Variation of the CT-number with the weight of $CaCO_3$.

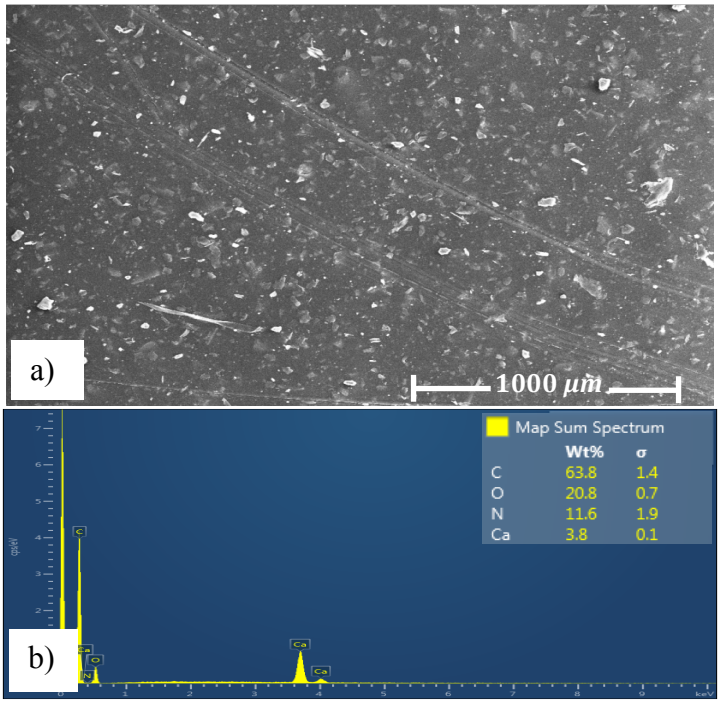

Figure 8.6 a) the SEM image of the polyurethane mixed with 2g $CaCO_3$. b) Displays of the EDS result, elemental spectrum and its corresponding elemental composition (weight%).

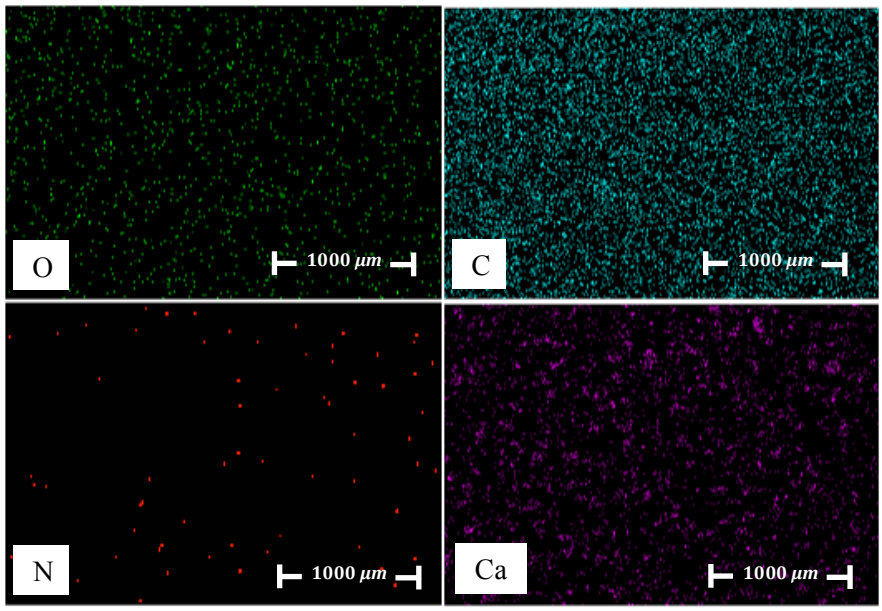

Figure 8.7 The distribution of elemental compositions of the polyurethane mixed with 2g $CaCO_3$ (oxygen (O), nitrogen (N), carbon (C), and calcium (Ca)), which can be used to visually evaluate the homogeneity of the elemental spreading over the sample medium.

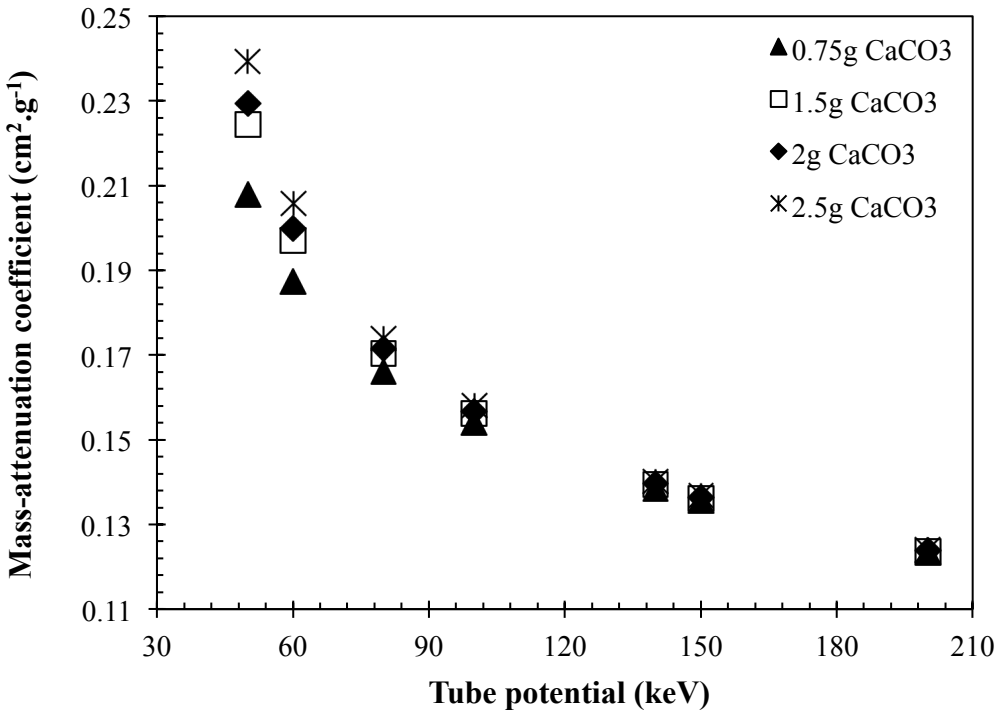

Figure 8.8 Mass attenuation coefficient of the polyurethane samples.

Table 8.1 The elemental compositions of the tissue substitute materials and human organs, measured physical density, and calculated the effective atomic numbers for each component or organ

$CaCO_3$ %weight in mixture (weight in 20g polyurethane)	Elemental composition (atomic %)													Specific gravity ($g.cm^{-3}$)	Effective atomic number (140.5 keV)
	N	**C**	**O**	**Ca**	**H**	**Na**	**Mg**	**P**	**S**	**Cl**	**K**	**Fe**	**Zn**		
3.61% (0.75g)	0.71	0.17	0.12	0.01	*	-	-	-	-	-	-	-	-	1.043	7.03
6.97% (1.5g)	0.69	0.16	0.13	0.01	*	-	-	-	-	-	-	-	-	1.069	7.16
9.09% (2.0g)	0.70	0.16	0.13	0.01	*	-	-	-	-	-	-	-	-	1.080	7.18
11.11% (2.5g)	0.70	0.17	0.12	0.02	*	-	-	-	-	-	-	-	-	1.098	7.29
Plaster of Paris	-	-	0.545	0.227	0.045	-	-	-	0.182	-	-	-	-	1.512**	12.56
Polyacrylamide	0.012	0.026	0.845	-	0.111	-	-	-	0.005	-	-	-	-	1.037	7.21
Eye lens compositions **ICRU44**[***]	0.057	0.195	0.646	-	0.096	0.001	-	0.001	0.003	0.001	-	-	-	1.070	6.93
Brain compositions **ICRU44**	0.022	0.145	0.712	-	0.107	0.002	-	0.004	0.002	0.003	0.003	-	-	1.040	7.07
Soft tissue compositions **ICRU44**	0.034	0.143	0.708	-	0.102	0.002	-	0.003	0.003	0.002	0.003	-	-	1.060	7.08
Bone compositions **ICRU44**	0.042	0.155	0.435	0.225	0.034	0.001	0.002	0.103	0.003	-	-	-	-	1.920	11.54
Liquid water **ICRU44**	-	-	0.888	-	0.112	-	-	-	-	-	-	-	-	1.000	7.22

* Not-detected element by EDS (Hydrogen),

** However the Plaster of Paris powder's density is 2.6 – 2.7 $g.cm^{-3}$ (3DSystems, 2013b), but the density of this powder when printed by 3D printer was found to be 1.512 $g.cm^{-3}$, which was found by dividing the measured weight of $5 \times 5 \times 1$ cm^3 printed block of the Plaster of Paris in its volume,

*** ICRU44: (Griffiths, 1989)

The linear attenuation coefficient of each substance was calculated by multiplying the sample's mass attenuation coefficient to its measured density. The linear attenuation coefficient of each sample was also obtained by experimental measurement using Tc^{99m} as a mono-energetic source and a gamma camera. The experimental measurement was only performed for the polyurethane samples (mixed with 0.75g, 1.5g, 2g, and 2.5g of $CaCO_3$ powder). This study showed that the linear attenuation coefficient values derived from the measurement are slightly greater than the values derived from the XCOM. As Figure 8.9 shows the measured linear attenuation coefficients for 140.5 keV photon beam agree with the calculated values to within 3%, with the standard deviation of less than 1.0%. This finding is in a good agreement with previous research by Hill *et al*., in 2008, which reported the disagreements of 3% and 7% between XCOM data and measurement findings using Tc^{99m} and gamma camera machine for solid phantoms and Perspex, respectively (Hill *et al*., 2008).

This level of agreement is considered acceptable due to some expected variations as, first, during the measurement using gamma camera the radiation source is not totally mono-energetic, since the energy window of ±5% (about 135.5 to 145.5 keV) was utilised for the scintillator crystal and Tc^{99m} as mentioned earlier emits gamma rays of other energies as well that may be collected by the energy window applied during the measurement, which are not included in XCOM calculations. The level of disagreement between the measured and calculated mass attenuation coefficient dropped to less than 2% by considering the exposure beam of 135.5 keV in XCOM calculations and up to 5% when the photon energy is set to 145.5 keV (Figure 8.9). The second reason, the SEM-EDS tested the elemental compositions of a very small area of the samples (less than 0.2 mm x 0.2 mm), which rises the inhomogeneity uncertainty, and the last possible reason, the lead container used to hold the radionuclide and also lead collimator could also

generate the secondary x-ray beam, which can contaminate the radiation beam emitted from the x-ray source during the experiment.

As Figure 8.10 shows the result of the SEM-EDS test is highly related to the region of the sample, which is taken for this test. The $CaCO_3$ powder does not dissolve in the polyurethane mixture, which increases the potential of the inhomogeneity uncertainty especially when a small area of the sample (~ 0.2 mm x 0.2 mm) is considered to represent the characteristic of the whole medium and elemental composition become very subjective to the selected area. In spite of the fact that the $CaCO_3$ powder was tried to mix well with the polyurethane composition, as it is clear from one of the SEM images, there is a higher concentration of the $CaCO_3$ powder in the centre and left-down corner of this sample (Figure 8.10). If this region is selected within the EDS's region of interest, due to higher existence of Ca in this region, the mass attenuation coefficient can be significantly changed. In order to minimise this uncertainty in this study, for each polyurethane material, evaluation of the samples elemental compositions were repeated three times from different parts of the samples surfaces.

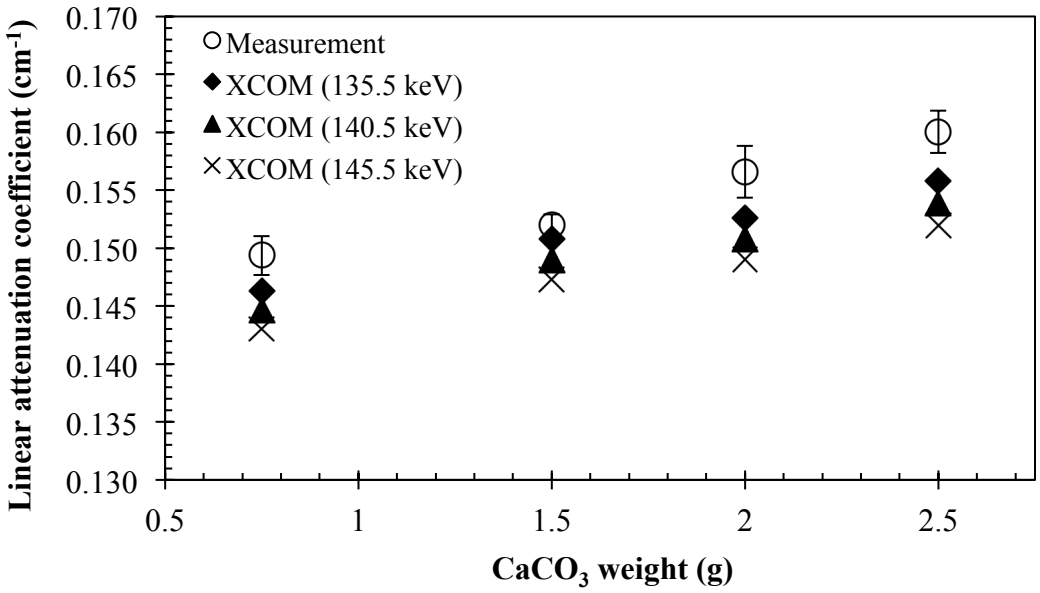

Figure 8.9 Comparison of the measured and calculated linear attenuation coefficients for different ratios of $CaCO_3$ mixture with polyurethane under 140.5 keV photon energy beam.

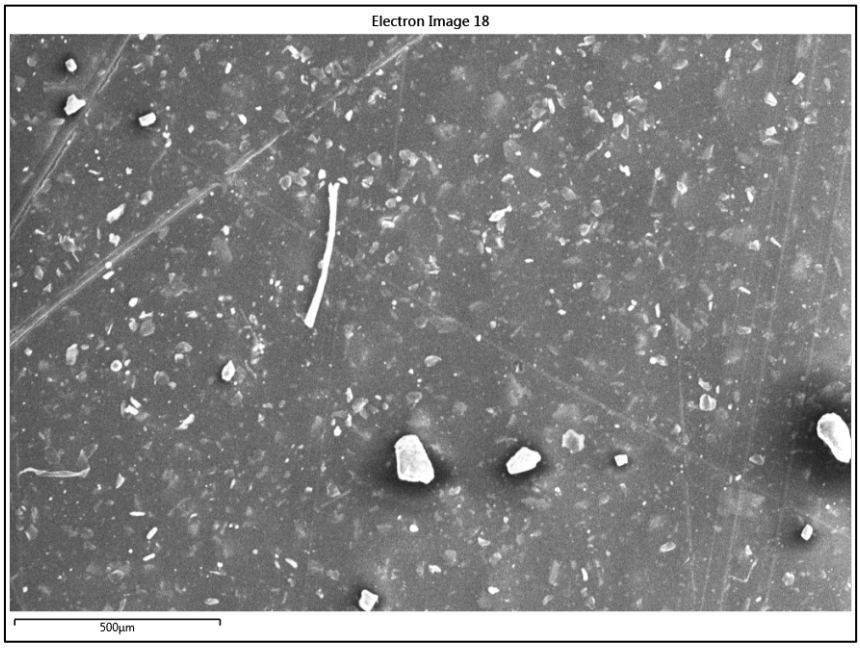

Figure 8.10 The SEM image of one sample of the polyurethane rubber mixed with 2.5g $CaCO_3$ powder.

The study on the linear attenuation coefficients of the eye lens for low energy photon beams (ICRU44) and linear attenuation coefficients of 2.5g $CaCO_3$ mixed with the polyurethane derived from the measurement showed high agreement among them for 140.5 keV, which supports the idea of using this composition as an eye lens mimicking medium (Figure 8.11). This finding is in a good agreement with the CT-scan result, which showed that the CT-number of the polyurethane composition mixed with 2.5g $CaCO_3$ (123 HU) is slightly higher than the average measured CT-number of human's eye lens (102.17 $\pm$ 10.44 HU). This difference can be justified by considering possibility of the CT-number averaging of the eye lens including the adjacent parts, due to the small physical size of the human lens. The evaluation of the maximum eye lens CT-number for each one of the 13 patients showed that the CT-number of the human eye lens using 120kVp scanning photon energy can reach to 117 HU (with average and standard deviation of 105.38 $\pm$ 10.56 HU). Although the physical density of the polyurethane composition mixed with 2.5g $CaCO_3$ (1.098 $g.cm^{-3}$) is higher than physical

density of the lens reported by ICRP44 (1.07 g.cm^{-3}) (Table 8.2), ICRP23 reported that the density of the human eye lens increases with age (from 1.034 g.cm^{-3} at 20 years to 1.113 g.cm^{-3} at 90 years) (Snyder *et al*., 1974).

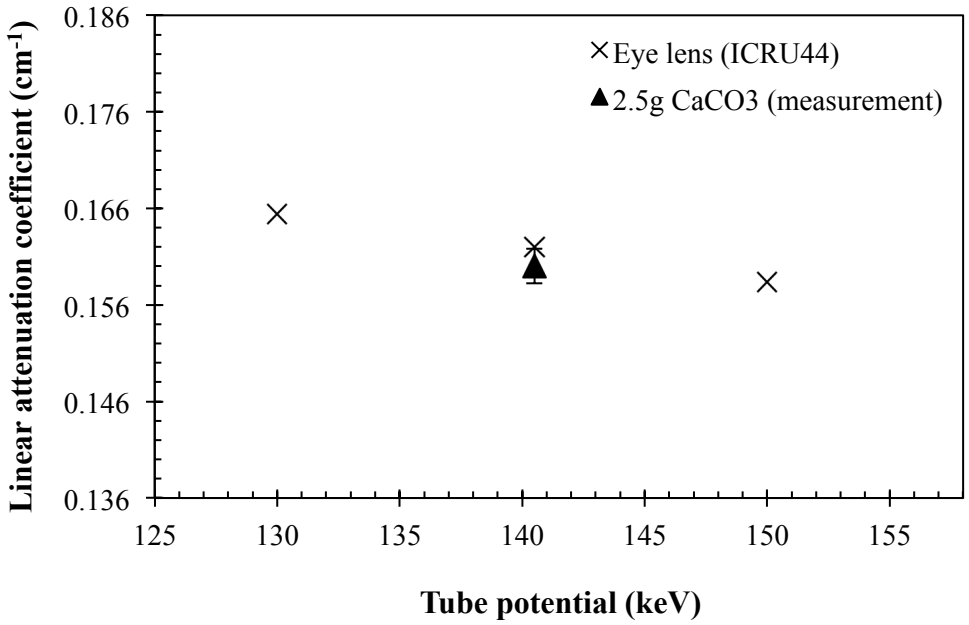

Figure 8.11 Comparison of the measured linear attenuation coefficient of the polyurethane sample (mixed with 2.5g $CaCO_3$) with eye lens linear attenuation coefficient reported by ICRU44 for beam energy of 140.5 keV.

8.4.2. Fabrication of an Anthropomorphic Head Phantom

Study of the attenuation properties of different mixture of the polyurethane and $CaCO_3$ (first part of this chapter) showed that, these compositions could be used as substitute parts of actual human eye. This study revealed that the polyurethane mixed with 2.5g $CaCO_3$ (11.11% $CaCO_3$ in the mixture) has a close attenuation range in compared with eye lens reported by ICRU44. Furthermore, it has been found that mixture of 0.75g $CaCO_3$ (3.61% $CaCO_3$ in the mixture) and 1.5g $CaCO_3$ (6.97% $CaCO_3$ in the mixture) are suitable to mimic the vitreous humor and cornea, respectively. These compositions were selected based on their close CT number with actual organs and

further investigation (comparison their mass attenuation coefficients with actual vitreous humor and cornea) was not possible to consider, due to lack of targeted reference tissue compositions for these organs. In the second part of this chapter segmentation of the 13 cases' eyes were performed using the OsiriX toolkit (Fig. 8.12, Table 8.3).

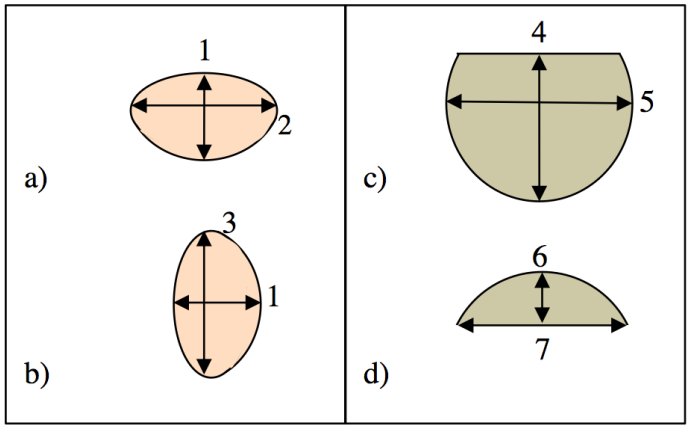

Figure 8.12 a) the segmentation of an eye lens in transverse view and b) sagittal view, c) transverse view of eyeball and d) cornea.

Table 8.3 The average and standard deviation of physical dimensions of the human eye lens, vitreous humor, and cornea. The number 1 to 7 corresponded to the dimensions labeled in Figure 8.12.

Eyeball Diameter (cm)	Eye lens dimension (mm)			Vitreous humor (mm)		Cornea & anterior cavity (mm)	
	1	**2**	**3**	**4**	**5**	**6**	**7**
21.9±1.1	4.4±0.6	8.1±0.6	8.3±0.8	15.8±1.1	22.2±0.9	2.1±0.4	9.2±0.8

Three different types of plastic moulds have been used to fabricate the eyeball, cornea, and lens in their corresponding physical size. The polyurethane mixtures were left to completely set for about 24 hours and later on removed from the moulds and they were fixed together to form the complete eyeball phantom (Figure 8.13a). The calcium sulphate hemihydrate (plaster of Paris; $CaSO_4 \cdot 2H_2O$) was used a bone tissue-equivalent substitute and construction a 60 years old male patient's skull using a three-dimensional (3D) printer (Figure 8.13b). Lastly the brain organ was fabricated using the

polyacrylamide component. The 3D-printed skull was filled by the polyacrylamide composition and left to set for a few minutes and after forming was sealed with a thin plastic sheet to avoid water evaporation (Figure 8.13c).

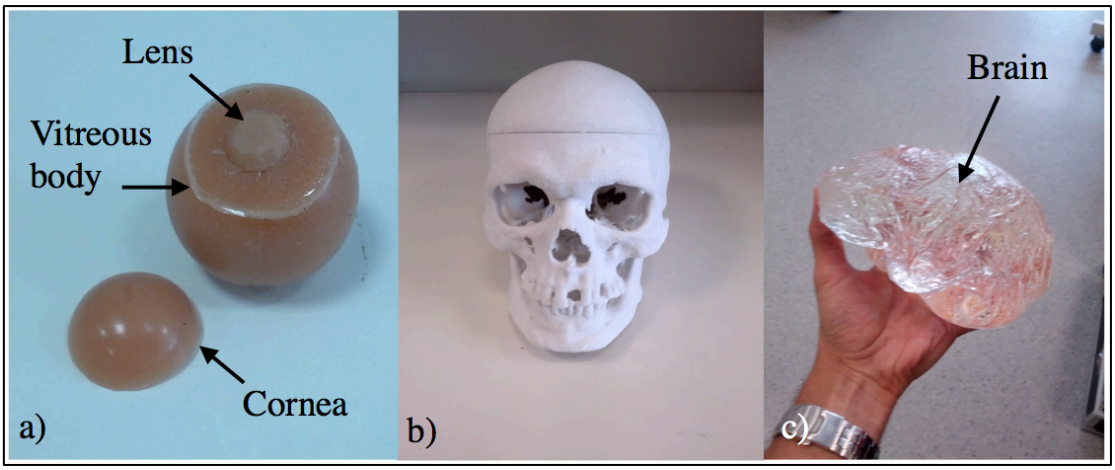

Figure 8.13 Schematic of the fabricated phantom, a) the eyeball (contains lens, cornea, and vitreous humor), b) the 3D printed skull, and c) the brain.

8.4.3. Evaluation of Patient's Dose

As Figure 8.14 shows the fabricated phantom can effectively be used to study the radiation dose distribution over the patient's eyeball, which is an inhomogeneous organ, consist of one of the most radiosensitive organs of the human body: eye lens. This phantom enables us to quantify the radiation dose received by different organs in the patient's head without the limitation of the radiation detector positioning. The radiation detector can be easily inserted at different level of the patient's eyeball, patient's brain and the radiation dose received at different location of the patient's skull is achievable.

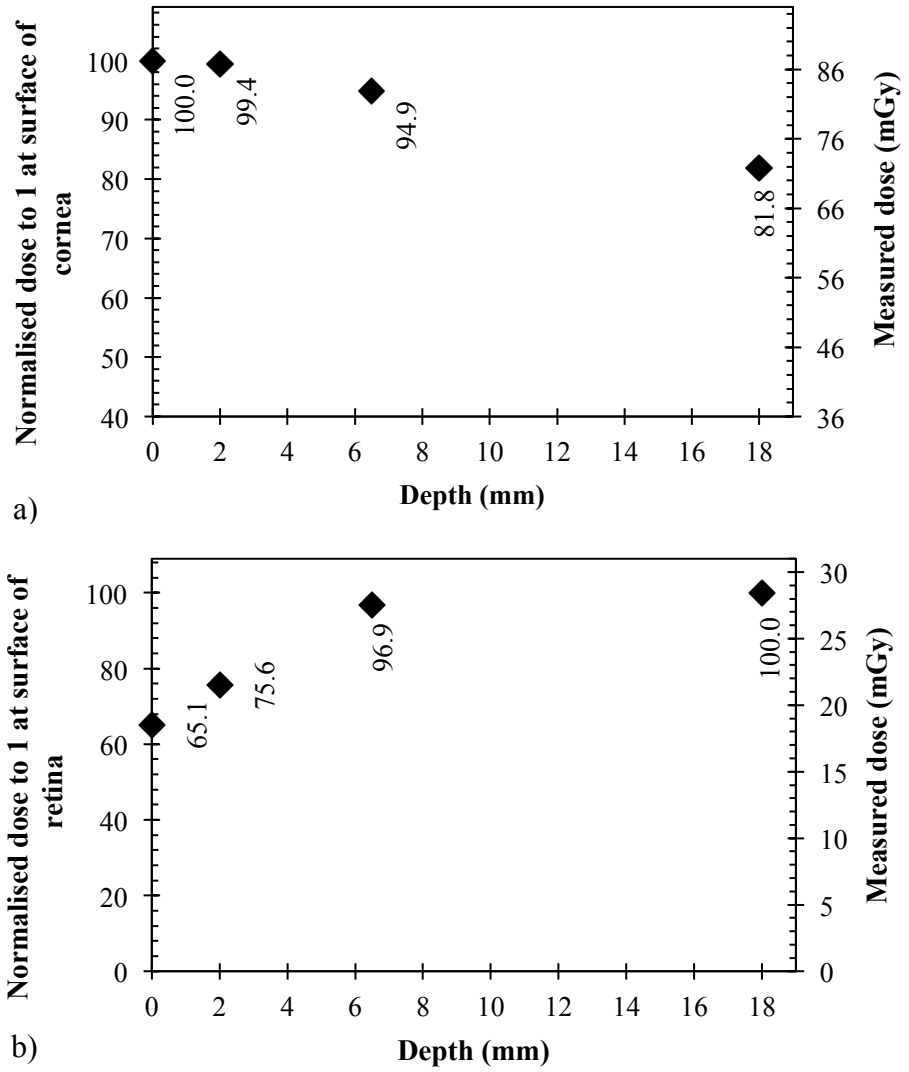

Figure 8.14 Penetration of the (a) anterior- posterior and (b) posterior-anterior radiation beams through the fabricated eyeball were measured using XR-RV3 film. The radiation doses at different level of the eyeball organ were normalised to measured dose at the surface of the cornea, and surface of retina for anterior- posterior and posterior-anterior projections, respectively.

8.5. Chapter Summary

In this chapter a custom-made anthropomorphic phantom was designed and fabricated using suitable tissue-mimicking mediums for evaluation of the radiation dose distribution over the patient's eye during clinical diagnostic procedures (research objective 6). This chapter investigated the radiation properties of the different tissue substitute materials in terms of their elemental compositions, physical density, effective atomic number, and linear attenuation coefficients through calculation and experimental measurement. This study revealed that polyurethane and polyacrylamide are considerably suitable to mimic the human's soft tissue including different part of the eyeball and brain, respectively. Using the polyurethane enabled us to fabricate different parts of the eyeball, such as cornea, vitreous humor, and lens. The polyurethane rubber provides several advantages in fabrication of an anthropomorphic phantom, such as its low viscosity makes it easy to pour this composition into moulds of various shapes, which after curing can easily be removed from the moulds. Furthermore, the polyurethane rubber showed very high homogeneity especially for small size samples and perfectly pliable that makes it unbreakable under stress or applying force. Having a flexible structure provides greater options for dosimeter placement at different regions of the phantom, which enables the phantom users to study the radiation dose received by various organs during a clinical procedure. The use of 3D printing technique in printing the skull of the phantom also demonstrates the great potential of this technique in manufacturing phantoms that are more realistic geometrically.

CHAPTER 9: CONCLUSION AND FUTURE WORK

9.1. Thesis Conclusion

9.1.1. Characterisation and New Application for the MO*Skin* Dosimetry System

In the chapter 4, the characterisation of the MO*Skin* detector in kilovoltage photon beams has been fully investigated. This study found that MO*Skin* detector has good reproducibility (94%) and dose linearity (99%) for the dose range of 2 to 213 cGy. The sensitivity did not significantly change with the variation of SSD (±1%), field size (±1%), frame rate (±3%), or beam energy (±5%). The detector angular dependence was within ±5% over 360◦ and the dose recorded by the MO*Skin* detector in different depths of a Solid Water® phantom was in good agreement with the Markus parallel plate ionisation chamber to within ±3%.

Chapter 5 demonstrated the application of the MO*Skin* dosimetry system in the real-time patient's eye lens dose monitoring during neuro-interventional procedures. The properties of the MO*Skin* dosimetry system for monitoring the patient eye lens dose during interventional radiology procedure include its small physical size, which preserves the image quality, ability to track the dose in real-time, linear response to the wide dose range, low angular and energy dependencies, ease of usage, and shallow effective depth were found to enable the MO*Skin* dosimetry system to be used for monitoring the radiation dose received by the eye lens. A study on 35 patients who underwent neuro-interventional procedures (comprising diagnostic angiographies, treatments of cerebral aneurysms, an embolizations of AVMs) revealed that available dose metrics parameters, such as KAP, FT, and air-kerma, are not accurate indicator of the actual dose received by patient's eye lens undergoing interventional radiology procedures. The MO*Skin* dose monitoring system enables interventional radiologists to have better awareness of the patient's eye lens dose and skin dose during clinical

procedures, which can provide radiologists with information needed to adjust the clinical procedure to control the patient's eye lens dose.

9.1.2. Contribution of the Exposure Parameters on Patient's Dose During Neuro-Interventional Procedures

From the study on the routine exposure parameters during neuro-interventional procedures in Chapter 6, it was found that DSA imaging technique contributed the highest patient dose (80.9%) and in terms of total frame number fluoroscopy imaging contributed the most (86.7%). The frontal tube was used more frequently, contributing to 75.4% of the total kerma-area product (KAP) and was usually placed under couch (73.7%). For this exposure direction, the occipital region received the highest dose. The occipital dose decreased by up to 40% with increasing exposure obliquity (0º to 60º RAO and 0º to 60º LAO) and increased by a factor of 1.94 with increasing magnification (48 to 15 cm). Changing the image to object distance (IOD) from 10 to 40 cm also increased the occipital dose by a factor of 2.0. This study clearly demonstrated that knowledge of the effects of exposure parameters on patient dose is a key factor for improving patient radiation safety, which helps interventional radiologists considerably in keeping the patient dose under the threshold dose levels for tissue reaction effects.

9.1.3. Radiation Protection of the Patient's Eye Lens for Neuro-Interventional Procedures

Complex and prolonged neuro-interventional radiology procedures using the biplane angiography system increase the patient's risk of radiation-induced cataract. Physical collimation is the most effective way of reducing the radiation dose to the patient's eye lens, but in instances where collimation is not possible, an attenuator may be useful in protecting the eyes. Chapter 7 demonstrated the design and fabrication of a new eye lens protector in order to reduce the radiation dose to the patients' eye lens during

neuro-interventional procedures. This study showed that eye protector reduced the radiation dose by up to 62.1% at the eye lens and was faintly visible in the fluoroscopy images and increased the tube current by a maximum of 3.7%. It is completely invisible in the acquisition mode and does not interfere with the clinical procedure.

9.1.4. Fabrication of an Anthropomorphic Phantom to Evaluate Eye Lens Dose

The commercial available anthropomorphic phantoms are generally constructed from three different tissue-equivalent materials for bone, soft tissue, and lung, mainly assembled in certain axial slices thickness (for instance 2.5 cm for RANDO® and ATOM® phantoms), and there is no particular design for phantom eye and it is considered as a homogenous organ with same tissue substitute with soft tissue. Due to these limitations, in this study a custom-made anthropomorphic phantom has been fabricated, which provides greater options for placement of the dosimeters and constructed from more similar tissue substitute materials to human eyeball.

From the results of various tissue substitute materials studies in chapter 8, it was found that the polyurethane based materials are suitable to mimic different parts of the human's eyeball, including cornea, lens, and vitreous humor. The mixture of 20g polyurethane rubber with 3g $CaCO_3$ provides extensively close attenuation range with eye lens. The polyurethane-based materials provides several advantages, like low viscosity, which makes it easy to pour this composition into moulds of various shapes, easily be removed from the moulds, high homogeneity, and perfectly pliable that provides more options for dosimeter placement. In this study the polyacrylamide has been used as a brain substitute material, which offers extremely high homogeneity for fabrication of large organs like brain, low viscosity, and considerably similar attenuation properties to the soft-tissue and brain. As chapter 8 showed, the 3D printing technologies can be used to fabricate anthropomorphic phantoms. This study showed that the calcium sulphate hemihydrate powder (ZP®151) used as one of the raw

materials in common 3D printing process, has quite similar attenuation properties with human bone and can be used to fabricate the bony structures like skull. This method enables us to fabricate the anthropomorphic phantom with extremely high accuracy of the physical shapes based on the patient's CT-images.

9.1.5. Research Contributions

The research has contributed to the field of radiation dosimetry in interventional radiology procedures in the following ways:

1 Characterised the MO*Skin* detector in kilovoltage photon beams and proposed this detector as a suitable dosimetry system for monitoring patient's skin dose during interventional radiology procedures.

2 Tested and demonstrated MO*Skin* dosimetry system as a suitable tool for patient's eye lens dosimetry and for assessment of exposure parameters contribution on patient's eye lens dose.

3 Presented a comprehensive evaluation of the exposure parameters contributions on radiation dose received by the patient's skin and eye lens during neuro-interventional procedures. This can be taken as a general guideline for interventional radiologists and radiographers to improve patient's radiation safety in their daily practice.

4 Introduced and tested a new eye lens protector as an in-field radiation protector. This eye protector helps to considerably reduce the patient's eye lens dose during neuro-interventional procedures with minimal effects on the exposure parameters and image quality.

5 Introduced a custom-made anthropomorphic head phantom using 3D printing technology, constructed from more similar tissue substitute materials to human eyeball. This phantom assists in performing reliable and accurate patient's eye lens dose measurements during a clinical diagnostic procedure.

9.2. Future Work

One of the main purposes of this research was to develop a new *in-vivo* single point dose-monitoring tool in order to evaluate the patient's eye lens dose in real-time for neuro-interventional procedure using the MO*Skin* dosimetry system. To study the maximum dose delivered to the patient's skin during these procedures a further research should be conducted to utilise a two-dimensional arrays of the MO*Skin* detectors, which can provide radiation dose distribution information over the patient's skin. This system would enable interventional radiologists to balance the expected clinical benefits and radiation risks of performing a procedure to the patient's skin.

This study has proposed to use a new type of the eye protector for patients undergoing neuro-interventional procedures to reduce the dose delivered to the eye lens. Future work will comprehensively evaluate the effect of the physical shape, and elemental composition of the eye protector on radiation dose distribution over the patient's head, quality of the image, and change of the exposure parameters. Smaller size of the eye protector with higher atomic density can considerably change the patient's radiation dose and corresponding lessen the protector impact on patient's image and exposure parameters during a clinical procedure.

By performing more research on available raw materials in 3D printing industry and evaluation of radiation properties of a wider range of materials, it is possible to find suitable tissue substitutes for various organs like soft-tissues, eye, brain, and lung, which enable us to print the whole phantom in one run. Application of the 3D-printing technology in fabrication of anthropomorphic phantom for dosimetry purposes has not been developed yet and more works needs to be done in this field.

REFERENCES

3DSystems. 2013a. zp®151 High Performance Composite, User Guide. from https://3dscentral.3dsystems.com/attachments/2238_95034%20zp151%20User%20Guide.pdf

3DSystems. 2013b. Material Safety Data Sheet, Material Name: zp®151 Powder. from http://www.sculpteo.com/static/0.30.049/documents/materials/multicolor/msds_zp151.pdf

Alnawaf, H, Butson, M, & Yu, PK. 2012. Measurement and effects of MO*SKIN* detectors on skin dose during high energy radiotherapy treatment. *Australasian Physical and Engineering Science in Medicine, 35*(3), 321-328.

Alshaikh, S, Carolan, M, Petasecca, M, Lerch, M, Metcalfe, P, & Rosenfeld, A. 2014. Direct and pulsed current annealing of p-MOSFET based dosimeter: the "MO*Skin*". *Australasian Physical and Engineering Science in Medicine, 37*(2), 311-319.

American Cancer Society. 2014. Skin Cancer: Basal and Squamous Cell. from http://www.cancer.org/cancer/skincancer-basalandsquamouscell/detailedguide/skin-cancer-basal-and-squamous-cell-what-is-basal-and-squamous-cell

Asadi-Eydivand, M, Solati-Hashjin, M, Farzad, A, & Osman, NAA. 2016. Effect of technical parameters on porous structure and strength of 3D printed calcium sulfate prototypes. *Robotics and Computer-Integrated Manufacturing, 37*, 57-67.

Attix, FH. 2008. *Introduction to radiological physics and radiation dosimetry*. John Wiley & Sons.

Balter, S. 2006. Methods for measuring fluoroscopic skin dose. *Pediatric Radiology, 36 Suppl 2*, 136-140.

Balter, S, Fletcher, DW, Kuan, HM, Miller, D, Richter, D, Seissl, H, & Shope Jr, TB. 2002. Techniques to estimate radiation dose to skin during fluoroscopically guided procedures. *AAPM Summer School Proceedings, Madison, WI,* 1-10.

Balter, S, Hopewell, JW, Miller, DL, Wagner, LK, & Zelefsky, MJ. 2010. Fluoroscopically guided interventional procedures: a review of radiation effects on patients' skin and hair. *Radiology, 254*(2), 326-341.

Bednarek, DR, Barbarits, J, Rana, VK, Nagaraja, SP, Josan, MS, & Rudin, S. 2011. Verification of the performance accuracy of a real-time skin-dose tracking system for interventional fluoroscopic procedures. *Proceedings of SPIE - The International Society for Optical Engineering, 7961*(796127).

Behrens, R. 2012. Monitoring the eye lens. *International Congress of the International Radiation Protection Association, IRPA13. Braunschweig, Germany*.

Berger, M, & Hubbell, J. 1987. XCOM, Photon cross sections on a personal computer. Report No. NBSIR87–3597. Gaithersburg, MD.

Berthelsen, B, & Cederblad, A. 1991. Radiation doses to patients and personnel involved in embolization of intracerebral arteriovenous malformations. *Acta Radiologica, 32*(6), 492-497.

Bini, MG, Ignesti, A, Millanta, L, Olmi, R, Rubino, N, & Vanni, R. 1984. The polyacrylamide as a phantom material for electromagnetic hyperthermia studies. *IEEE Transaction Biomedical Engineering, 31*(3), 317-322.

Bordier, C, Klausz, R, & Desponds, L. 2015. Patient dose map indications on interventional X-ray systems and validation with Gafchromic XR-RV3 film. *Radiation Protection Dosimetry, 163*(3), 306-318.

Boutillon, M, & Perroche, A. 1985. Effect of a change of stopping-power values on the W value recommended by ICRU for electrons in dry air. *Report CCEMRI (I)*, *Bureau International Bureau of Weights and Measures, France,* 85-88.

Bowmaker, JK, & Dartnall, HJ. 1980. Visual pigments of rods and cones in a human retina. *Journal of Physiology, 298*, 501-511.

Bushberg, JT, Seibert, JA, Leidholdt Jr, EM, Boone, JM, & Goldschmidt Jr, EJ. 2003. The essential physics of medical imaging. *Lippincott Williams & Wilkins. Philadelphia, USA*.

Butson, MJ, Rozenfeld, A, Mathur, JN, Carolan, M, Wong, TP, & Metcalfe, PE. 1996. A new radiotherapy surface dose detector:the MOSFET. *Medical Physics, 23*(5), 655-658.

Casselden, PA. 1988. Ocular lens dose in cerebral vascular imaging. *British Journal of Radiology, 61*(723), 202-204.

Cheung, T, Butson, MJ, & Yu, PK. 2004. Effects of temperature variation on MOSFET dosimetry. *Physics in Medicine and Biology, 49*(13), 191-196.

Cheung, T, Butson, MJ, & Yu, PK. 2009. Energy dependence corrections to MOSFET dosimetric sensitivity. *Australasian Physical and Engineering Science in Medicine, 32*(1), 16-20.

Chida, K, Kato, M, Kagaya, Y, Zuguchi, M, Saito, H, Ishibashi, T, Takahashi, S, Yamada, S, & Takai, Y. 2010. Radiation dose and radiation protection for patients and physicians during interventional procedure. *Journal of Radiation Research, 51*(2), 97-105.

Chodick, G, Bekiroglu, N, Hauptmann, M, Alexander, BH, Freedman, DM, Doody, MM, Cheung, LC, Simon, SL, Weinstock, RM, Bouville, A, & Sigurdson, AJ. 2008. Risk of cataract after exposure to low doses of ionizing radiation: a 20-year prospective cohort study among US radiologic technologists. *American Journal of Epidemiology, 168*(6), 620-631.

Church, CA, Kuhn, FA, Mikhail, J, Vaughan, WC, & Weiss, RL. 2008. Patient and surgeon radiation exposure in balloon catheter sinus ostial dilation. *Otolaryngology - Head and Neck Surgery, 138*(2), 187-191.

Comesana, R, Lusquinos, F, Del Val, J, Malot, T, López-Álvarez, M, Riveiro, A, Quintero, F, Boutinguiza, M, Aubry, P, & De Carlos, A. 2011. Calcium phosphate grafts produced by rapid prototyping based on laser cladding. *Journal of the European Ceramic Society, 31*(1), 29-41.

Consorti, R, Petrucci, A, Fortunato, F, Soriani, A, Marzi, S, Iaccarino, G, Landoni, V, & Benassi, M. 2005. *In vivo* dosimetry with MOSFETs: dosimetric characterization and first clinical results in intraoperative radiotherapy. *International Journal of Radiation Oncology • Biology • Physics, 63*(3), 952-960.

Cui, X, Breitenkamp, K, Finn, MG, Lotz, M, & D'Lima, DD. 2012. Direct human cartilage repair using three-dimensional bioprinting technology. *Tissue Engineering Part A, 18*(11-12), 1304-1312.

D'Alessio, D, Giliberti, C, Soriani, A, Carpanese, L, Pizzi, G, Vallati, G, & Strigari, L. 2013. Dose evaluation for skin and organ in hepatocellular carcinoma during angiographic procedure. *Journal of Experimental & Clinical Cancer Research, 32*, 81.

Dabbagh, A, Abdullah, BJ, Ramasindarum, C, & Abu Kasim, NH. 2014a. Tissue-mimicking gel phantoms for thermal therapy studies. *Ultrasonic Imaging, 36*(4), 291-316.

Dabbagh, A, Abdullah, BJ, Abu Kasim, NH, & Ramasindarum, C. 2014b. Reusable heat-sensitive phantom for precise estimation of thermal profile in hyperthermia application. *International Journal of Hyperthermia, 30*(1), 66-74.

Datla, NV, Konh, B, Koo, JJ, Choi, DJ, Yu, Y, Dicker, AP, Podder, TK, Darvish, K, & Hutapea, P. 2014. Polyacrylamide phantom for self-actuating needle-tissue interaction studies. *Medical Engineering & Physics, 36*(1), 140-145.

D'Ercole, L, Mantovani, L, Thyrion, FZ, Bocchiola, M, Azzaretti, A, Di Maria, F, Saluzzo, CM, Quaretti, P, Rodolico, G, Scagnelli, P, & Andreucci, L. 2007. A study on maximum skin dose in cerebral embolization procedures. *American Journal of Neuroradiology, 28*(3), 503-507.

D'Orazio, J, Jarrett, S, Amaro-Ortiz, A, & Scott, T. 2013. UV Radiation and the Skin. *International Journal of Molecular Sciences, 14*(6), 12222-12248.

Datar, A, Joshi, P, & Lee, MY. 2015. Biocompatible Hydrogels for Microarray Cell Printing and Encapsulation. *Biosensors (Basel), 5*(4), 647-663.

Davson,H. 2016. Human eye anatomy. from http://www.britannica.com/science/human-eye

De Coppi, P, Bartsch, G, Jr., Siddiqui, MM, Xu, T, Santos, CC, Perin, L, Mostoslavsky, G, Serre, AC, Snyder, EY, Yoo, JJ, Furth, ME, Soker, S, & Atala, A. 2007. Isolation of amniotic stem cell lines with potential for therapy. *Nature Biotechnology, 25*(1), 100-106.

Dendy, PP, & Heaton, B. 2011. *Physics for diagnostic radiology*. CRC, Boca Raton, FL

Durchschlag, H, Fochler, C, Abraham, K, & Kulawik, B. 1999. Radiation effects on eye components. *Radiation Physics Chemistry, 55*(5), 691-697.

Efstathopoulos, EP, Karvouni, E, Kottou, S, Tzanalaridou, E, Korovesis, S, Giazitzoglou, E, & Katritsis, DG. 2004. Patient dosimetry during coronary interventions: a comprehensive analysis. *American Heart Journal, 147*(3), 468-475.

Ehringfeld, C, Schmid, S, Poljanc, K, Kirisits, C, Aiginger, H, & Georg, D. 2005. Application of commercial MOSFET detectors for *in vivo* dosimetry in the therapeutic x-ray range from 80 kV to 250 kV. *Physics in Medicine and Biology, 50*(2), 289-303.

Einstein, AJ, Elliston, CD, Arai, AE, Chen, MY, Mather, R, Pearson, GD, Delapaz, RL, Nickoloff, E, Dutta, A, & Brenner, DJ. 2010. Radiation dose from single-heartbeat coronary CT angiography performed with a 320-detector row volume scanner. *Radiology, 254*(3), 698-706.

Ensell, G, Holmes-Siedle, A, & Adams, L. 1988. Thick oxide pMOSFET dosimeters for high energy radiation. *Nuclear Instruments and Methods in Physics Research Section A: Accelerators, Spectrometers, Detectors and Associated Equipment, 269*(3), 655-658.

Faulkner-Jones, A, Fyfe, C, Cornelissen, DJ, Gardner, J, King, J, Courtney, A, & Shu, W. 2015. Bioprinting of human pluripotent stem cells and their directed differentiation into hepatocyte-like cells for the generation of mini-livers in 3D. *Biofabrication, 7*(4), 044102.

Fletcher, DW, Miller, DL, Balter, S, & Taylor, MA. 2002. Comparison of four techniques to estimate radiation dose to skin during angiographic and interventional radiology procedures. *Journal of Vascular Interventinal Radiology, 13*(4), 391-397.

Food and Drug Administration. 1994. Public Health Advisory: avoidance of serious x-ray-induced skin injuries to patients during fluoroscopically-guided procedures. *Rockville, MD: Center for Devices and Radiological Health*.

Food and Drug Administration. 2005. Performance standard for diagnostic x-ray systems and their major components. *Code of Federal Regulations Title 21*. https://www.accessdata.fda.gov/scripts/cdrh/cfdocs/cfCFR/CFRSearch.cfm?CFRPart=1020

Food and Drug Administration. 2005. Electronic products; performance standard for diagnostic x-ray systems and their major components. Final rule. *Federal Register, 70*(111), 33997-34042.

Frazier, TH, Richardson, JB, Fabre, VC, & Callen, JP. 2007. Fluoroscopy-induced chronic radiation skin injury: a disease perhaps often overlooked. *Archives of dermatology, 143*(5), 637-640.

Geise, RA, & O'Dea, TJ. 1999. Radiation dose in interventional fluoroscopic procedures. *Applied Radiation and Isotopes, 50*(1), 173-184.

Giles, ER, & Murphy, PH. 2002. Measuring skin dose with radiochromic dosimetry film in the cardiac catheterization laboratory. *Health Physics, 82*(6), 875-880.

Giordano, C, D'Ercole, L, Gobbi, R, Bocchiola, M, & Passerini, F. 2010. Coronary angiography and percutaneous transluminal coronary angioplasty procedures: Evaluation of patients' maximum skin dose using Gafchromic films and a comparison of local levels with reference levels proposed in the literature. *Physica Medica, 26*(4), 224-232.

Gislason, A, Hoornaert, B, Davies, A, & Cowen, A. 2011. Allura Xper Cardiac System implementation of automatic dose rate control. *Philips Healthcare*.

Glennie, D, Connolly, BL, & Gordon, C. 2008. Entrance skin dose measured with MOSFETs in children undergoing interventional radiology procedures. *Pediatric Radiology, 38*(11), 1180-1187.

Goodhead, DT. 1994. Initial events in the cellular effects of ionizing radiations: clustered damage in DNA. *International Journal of Radiation Biology, 65*(1), 7-17.

Griffith, R, Dean, P, Anderson, A, & Fisher, J. 1979. A tissue-equivalent torso phantom. *For intercalibration of in-vivo, transuranic-nuclide counting facilities. Vienna, Austria: International Atomic Energy Agency*, 493-503.

Griffiths, HJ. 1989. Tissue Substitutes in Radiation Dosimetry and Measurement. No. 4. *Radiology, 173*(1), 202-202.

Gross, H, Blechinger, F, & Achtner, B. 2008. *Handbook of Optical Systems, Survey of Optical Instruments*. *Wiley-VCH, Weinheim, Germany.*

Gupta, AK, Chowdhury, V, & Khandelwal, N. 2013. *Diagnostic Radiology: Recent Advances and Applied Physics in Imaging*. JP Medical Ltd.

Gur, Y. 2014. Additive Manufacturing of Anatomical Models from Computed Tomography Scan Data. *Molecular & Cellular Biomechanics, 11*(4), 249-258.

Hafner, B. 2006. Energy Dispersive Spectroscopy on the SEM: a primer. *Characterization Facility, University of Minnesota*, 1-26.

Halvorsen, PH. 2005. Dosimetric evaluation of a new design MOSFET *in vivo* dosimeter. *Medical Physics, 32*(1), 110-117.

Hardcastle, N, Cutajar, DL, Metcalfe, PE, Lerch, ML, Perevertaylo, VL, Tome, WA, & Rosenfeld, AB. 2010. *In vivo* real-time rectal wall dosimetry for prostate radiotherapy. *Physics in Medicine and Biology, 55*(13), 3859-3871.

Harle-Bachor, C, & Boukamp, P. 1996. Telomerase activity in the regenerative basal layer of the epidermis inhuman skin and in immortal and carcinoma-derived skin keratinocytes. *Proceedings of the National Academy of Sciences of the United States of America, 93*(13), 6476-6481.

Hwang, E, Gaxiola, E, Vlietstra, RE. 1998. Real-time measurement of skin radiation during cardiac catheterization. *Catheterization and Cardiovascular Diagnosis*, 43:367-70.

Hayakawa, M, Moritake, T, Kataoka, F, Takigawa, T, Koguchi, Y, Miyamoto, Y, Akahane, K, & Matsumaru, Y. 2010. Direct measurement of patient's entrance skin dose during neurointerventional procedure to avoid further radiation-induced skin injuries. *Clinical neurology and neurosurgery, 112*(6), 530-536.

Haynes, K, Sherer, MAS, Visconti, PJ, & Ritenour, ER. 2013. *Radiation Protection in Medical Radiography*. Elsevier Health Sciences.

Heaney, DE, & Norvill, CA. 2006. A comparison of reduction in CT dose through the use of gantry angulations or bismuth shields. *Australasian Physical and Engineering Science in Medicine, 29*(2), 172-178.

Hein, E, Rogalla, P, Klingebiel, R, & Hamm, B. 2002. Low-dose CT of the paranasal sinuses with eye lens protection: effect on image quality and radiation dose. *European Radiology, 12*(7), 1693-1696.

Henke, BL, Lee, P, Tanaka, T, Shimabukuro, RL, & Fujikawa, B. 1982. Low-energy X-ray interaction coefficients: photoabsorption, scattering, and reflection: E= 100–2000 eV Z= 1–94. *Atomic data and nuclear data tables, 27*(1), 1-144.

Holmes-Siedle, A. 1974. The space-charge dosimeter: General principles of a new method of radiation detection. *Nuclear Instruments and Methods, 121*(1), 169-179.

Holmes-Siedle, A. 1994. *From space to therapy the radiation sensitive silicon fet (RADFET)*. Paper presented at the Technology Transfer Workshop. European Space Agency, ESA SP-364, ESA/ESTEC, Noordwijk, the Netherlands.

Hopper, KD, Neuman, JD, King, SH, & Kunselman, AR. 2001. Radioprotection to the eye during CT scanning. *American Journal of Neuroradiology, 22*(6), 1194-1198.

Hermann, K-P, Geworski, L, Muth, M, & Harder, D. 1985. Polyethylene-based water-equivalent phantom material for x-ray dosimetry at tube voltages from 10 to 100 kV. *Physics in medicine and biology, 30*(11), 1195.

Hubbell, JH. (1969). Photon cross sections, attenuation coefficients, and energy absorption coefficients from 10 keV to 100 GeV: National Standard Reference Data Series. 29.

Hull, CW. (1986). Apparatus for production of three-dimensional objects by stereolithography: Google Patents. http://www.google.com/patents/US4575330.

Hurwitz, LM, Reiman, RE, Yoshizumi, TT, Goodman, PC, Toncheva, G, Nguyen, G, & Lowry, C. 2007. Radiation dose from contemporary cardiothoracic multidetector CT protocols with an anthropomorphic female phantom: implications for cancer induction. *Radiology, 245*(3), 742-750.

International Atomic Energy Agency. 2010. Patient dose optimization in fluoroscopically guided interventional procedures. *IAEA-TECDOC-1641: IAEA*.

International Electrotechnical Commission. 2000. Particular requirements for the safety of X-ray equipment for interventional procedures. *IEC 60601,* Geneva, Switzerland.

International Electrotechnical Commission. 2005. Radiation conditions for use in the determination of characteristics. *IEC 61267*, Geneva, Switzerland.

ICRP. 1991 The biological basis for dose limitation in the skin. A report of a Task Group of Committee 1 of the International Commission on Radiological Protection. *Ann ICRP, 22*(2), 1-104.

ICRP. 2007. The 2007 Recommendations of the International Commission on Radiological Protection. ICRP publication 103. *Ann ICRP, 37*(2-4), 1-332.

ICRU. 1993. Quantities and units in radiation protection dosimetry.

ICRU. 1980. Report 33. *Int. Comm. Radiation Units and Measurements, Washington DC*.

Ilgit, ET, Meric, N, Bor, D, Öznur, I, Konus, Oz, & Isik, S. 2000. Lens of the Eye: Radiation Dose in Balloon Dacryocystoplasty 1. *Radiology, 217*(1), 54-57.

Jackson, DF, & Hawkes, DJ. 1981. X-ray attenuation coefficients of elements and mixtures. *Physics Reports, 70*(3), 169-233.

Jaco, JW, & Miller, DL. 2010. Measuring and monitoring radiation dose during fluoroscopically guided procedures. *Techniques in Vascular and Interventional Radiology, 13*(3), 188-193.

Johns, H, & Cunningham, J. 1983. The Physics of Radiology 4th edn (Springfield, IL: Thomas).

Johnson, PB, Borrego, D, Balter, S, Johnson, K, Siragusa, D, & Bolch, WE. 2011. Skin dose mapping for fluoroscopically guided interventions. *Medical Physics, 38*(10), 5490-5499.

Jones, AK, Hintenlang, D, Bolch, W. 2003. Tissue-equivalent materials for construction of tomographic dosimetry phantoms in pediatric radiology. *Medical Physics*, 30(8), 2072-2081.

Jones, AK, Simon, TA, Bolch, WE, Holman, MM, & Hintenlang, DE. 2006. Tomographic physical phantom of the newborn child with real-time dosimetry I. Methods and techniques for construction. *Medical Physics, 33*(9), 3274-3282.

Jorge, L. (1968). Lithium drifted semiconductor radiation detector: Google Patents.

Jung, JW, Lee, H, Hong, JM, Park, JH, Shim, JH, Choi, TH, & Cho, DW. 2015. A new method of fabricating a blend scaffold using an indirect three-dimensional printing technique. *Biofabrication, 7*(4), 045003.

Kalra, MK, Dang, P, Singh, S, Saini, S, & Shepard, JA. 2009. In-plane shielding for CT: effect of off-centering, automatic exposure control and shield-to-surface distance. *Korean Journal of Radiology, 10*(2), 156-163.

Khan, FM, & Gibbons, JP. 1994. *The Physics of Radiation Therapy*. Lippincott Williams & Wilkins.

Khodadadegan, Y, Zhang, M, Pavlicek, W, Paden, RG, Chong, B, Schueler, BA, Fetterly, KA, Langer, SG, & Wu, T. 2011. Automatic monitoring of localized skin dose with fluoroscopic and interventional procedures. *Journal of Digital Imaging, 24*(4), 626-639.

Koenig, TR, Wolff, D, Mettler, FA, & Wagner, LK. 2001. Skin injuries from fluoroscopically guided procedures: part 1, characteristics of radiation injury. *American Journal of Roentgenology, 177*(1), 3-11.

Koenig, TR, Mettler, FA, & Wagner, LK. 2001. Skin injuries from fluoroscopically guided procedures: part 2, review of 73 cases and recommendations for minimizing dose delivered to patient. *American Journal of Roentgenology, 177*(1), 13-20.

Kron, T. 1995. Thermoluminescence dosimetry and its applications in medicine--Part 2: History and applications. *Australasian Physical and Engineering Science in Medicine, 18*(1), 1-25.

Kron, T, Duggan, L, Smith, T, Rosenfeld, A, Butson, M, Kaplan, G, Howlett, S, & Hyodo, K. 1998. Dose response of various radiation detectors to synchrotron radiation. *Physics in Medicine and Biology, 43*(11), 3235-3259.

Kwan, IS, Rosenfeld, AB, Qi, ZY, Wilkinson, D, Lerch, ML, Cutajar, DL, Safavi-Naeni, M, Butson, M, Bucci, J, & Chin, Y. 2008. Skin dosimetry with new MOSFET detectors. *Radiation Measurements, 43*(2), 929-932.

Kwan, IS, Wilkinson, D, Cutajar, D, Lerch, M, Rosenfeld, A, Howie, A, Bucci, J, Chin, Y, & Perevertaylo, VL. 2009. The effect of rectal heterogeneity on wall dose in high dose rate brachytherapy. *Medical Physics, 36*(1), 224-232.

Lee, J, Hoss, D, & Phillips, TJ. 2003. Fluoroscopy-induced skin necrosis. *Archives of Dermatology, 139*(2), 140-142.

Lee, K, Lee, W, Lee, J, Lee, B, & Oh, G. 2010. Dose reduction and image quality assessment in MDCT using AEC (D-DOM & Z-DOM) and in-plane bismuth shielding. *Radiation Protection Dosimetry, 141*(2), 162-167.

Liacouras, P, Garnes, J, Roman, N, Petrich, A, & Grant, GT. 2011. Designing and manufacturing an auricular prosthesis using computed tomography, 3-dimensional photographic imaging, and additive manufacturing: a clinical report. *Journal of Prosthetic Dentistry, 105*(2), 78-82.

Lian, CP, Othman, MA, Cutajar, D, Butson, M, Guatelli, S, & Rosenfeld, AB. 2011. Monte Carlo study of the energy response and depth dose water equivalence of the MO*Skin* radiation dosimeter at clinical kilovoltage photon energies. *Australasian Physical and Engineering Science in Medicine, 34*(2), 273-279.

Lian, CPL, Wong, JHD, Young, A, Cutajar, D, Petasecca, M, Lerch, MLF, & Rosenfeld, AB. 2013. Measurement of multi-slice computed tomography dose profile with the Dose Magnifying Glass and the MO*Skin* radiation dosimeter. *Radiation Measurements, 55*, 51-55.

Litovchenko, P, Barabash, L, Rosenfeld, A, Khivrich, V, Zinets, O, Kuts, V, Marusan, I, Petrov, V, Sluchenkov, G, & Koval, G. 1990. MOS structure for emergency gamma and proton dosimetry. *Radiation Protection Dosimetry, 33*(1-4), 179-182.

Ling, T, Jin, Q, Yao, H, & Zheng, H. (2010). *Design and characterization of a tissue-mimicking phantom for ultrasonic elastography*. Paper presented at the Bioinformatics and Biomedical Engineering (iCBBE), 2010 4th International Conference.

Lomax, ME, Folkes, LK, & O'Neill, P. 2013. Biological consequences of radiation-induced DNA damage: relevance to radiotherapy. *Clinical Oncology (R Coll Radiol), 25*(10), 578-585.

Mahesh, M. 2001. Fluoroscopy: Patient Radiation Exposure Issues 1. *Radiographics, 21*(4), 1033-1045.

Manohara, S, Hanagodimath, S, Thind, K, & Gerward, L. 2008. On the effective atomic number and electron density: a comprehensive set of formulas for all types of materials and energies above 1keV. *Nuclear Instruments and Methods in Physics Research Section B: Beam Interactions with Materials and Atoms, 266*(18), 3906-3912.

Massey, J. 1974. Data for Protection against Ionizing Radiation from External Sources: Supplement to ICRP Publication 15. *International journal of radiation biology and related studies in physics, chemistry , and medicine 25*(4), 419-420.

Matsubara, K, Koshida, K, Noto, K, Takata, T, Suzuki, M, Shimono, T, Yamamoto, T, & Matsui, O. 2011. A head phantom study for intraocular dose evaluation of 64-slice multidetector CT examination in patients with suspected cranial trauma. *European Journal of Radiology, 79*(2), 283-287.

McCabe, BP, Speidel, MA, Pike, TL, & Van Lysel, MS. 2011. Calibration of GafChromic XR-RV3 radiochromic film for skin dose measurement using standardized x-ray spectra and a commercial flatbed scanner. *Medical Physics, 38*(4), 1919-1930.

McParland, BJ. 1998. Entrance skin dose estimates derived from dose-area product measurements in interventional radiological procedures. *British Journal of Radiology, 71*(852), 1288-1295.

Meriçı, N, Bor, D, Ilgıt, ET, Öznur, İ, & Büget, N. 1998. Comparison of eye lens dose measurement techniques in imaging and interventions of the lachrymal drainage system. *Physica Medica, 14*(3).

Miller, DL, Balter, S, Cole, PE, Lu, HT, Berenstein, A, Albert, R, Schueler, BA, Georgia, JD, Noonan, PT, Russell, EJ. 2003. Radiation doses in interventional radiology procedures: the RAD-IR study: part II: skin dose. *Journal of Vascular Interventional Radiology, 14*(8), 977-990.

Miller, DL, Balter, S, Schueler, BA, Wagner, LK, Strauss, KJ, & Vano, E. 2010. Clinical radiation management for fluoroscopically guided interventional procedures. *Radiology, 257*(2), 321-332.

Mooney, RB, McKinstry, CS, & Kamel, HA. 2000. Absorbed dose and deterministic effects to patients from interventional neuroradiology. *British Journal of Radiology, 73*(871), 745-751.

Moritake, T, Hayakawa, M, Matsumaru, Y, Takigawa, T, Koguchi, Y, Miyamoto, Y, Mizuno, Y, Chida, K, Akahane, K, & Tsuboi, K. 2011. Precise mapping system of entrance skin dose during endovascular embolization for cerebral aneurysm. *Radiation Measurements, 46*(12), 2103-2106.

Moritake, T, Matsumaru, Y, Takigawa, T, Nishizawa, K, Matsumura, A, & Tsuboi, K. 2008. Dose measurement on both patients and operators during neurointerventional procedures using photoluminescence glass dosimeters. *American Journal of Neuroradiology, 29*(10), 1910-1917.

Moulin, G, Chagnaud, C, Waultier, S, Le Brigand, B, Espagnan, M, Dessi, P, Bartoli, JM, Chatenet, P, & Botti, G. 1996. Radiation dose to the lenses in CT of the paranasal sinuses. *Neuroradiology, 38 Suppl 1*, S127-129.

Mrena, S, Kivela, T, Kurttio, P, & Auvinen, A. 2011. Lens opacities among physicians occupationally exposed to ionizing radiation--a pilot study in Finland. *Scandinavian Journal of Work, Environment & Health, 37*(3), 237-243.

Mukundan, S, Jr., Wang, PI, Frush, DP, Yoshizumi, T, Marcus, J, Kloeblen, E, & Moore, M. 2007. MOSFET dosimetry for radiation dose assessment of bismuth shielding of the eye in children. *American Journal of Roentgenology, 188*(6), 1648-1650.

Murphy, SV, & Atala, A. 2014. 3D bioprinting of tissues and organs. *Nature Biotechnology, 32*(8), 773-785.

Mustafa, AA, & Janeczek, J. 1989. Organ doses from cardiac and carotid digital subtraction angiography. *British Journal of Radiology, 62*(741), 838-842.

Naftulin, JS, Kimchi, EY, & Cash, SS. 2015. Streamlined, Inexpensive 3D Printing of the Brain and Skull. *PLOS One, 10*(8).

Nie, LH, Sanchez, S, Newton, K, Grodzins, L, Cleveland, RO, & Weisskopf, MG. 2011. In vivo quantification of lead in bone with a portable x-ray fluorescence system--methodology and feasibility. *Physics in Medicine and Biology, 56*(3), N39-51.

Nikjoo, H, Uehara, S, Wilson, WE, Hoshi, M, & Goodhead, DT. 1998. Track structure in radiation biology: theory and applications. *International Journal of Radiation Biology, 73*(4), 355-364.

Nishizawa, K, Moritake, T, Matsumaru, Y, Tsuboi, K, & Iwai, K. 2003. Dose measurement for patients and physicians using a glass dosemeter during endovascular treatment for brain disease. *Radiation Protection Dosimetry, 107*(4), 247-252.

National Institute of Standards and Technology. 1999. NIST XCOM: Photon Cross Sections Database. Accessed December 05, 2015, from http://physics.nist.gov/PhysRefData/Xcom/html/xcom1.html

National Institute of Standards and Technology. 2010. X-ray form factor, attenuation, and scattering tables. Accessed January 12, 2015, from http://physics.nist.gov/cgi-bin/ffast/ffast.pl?Z=13&Formula=&gtype=5&range=U&lower=&upper=&density=

Ngo, PD. (1999). Energy dispersive spectroscopy *Failure Analysis of Integrated Circuits* (pp. 205-215): Springer.

Niu, Y, Wang, Z, Liu, Y, Liu, Z, & Yao, V. 2010. Radiation dose to the lens using different temporal bone CT scanning protocols. *American Journal of Neuroradiology, 31*(2), 226-229.

Nowotny, R. 1998. XMuDat: Photon attenuation data on PC. *IAEA Report IAEA-NDS, 195*.

Ouyang, L, Yao, R, Mao, S, Chen, X, Na, J, & Sun, W. 2015. Three-dimensional bioprinting of embryonic stem cells directs highly uniform embryoid body formation. *Biofabrication, 7*(4), 044101.

Peet, DJ, & Pryor, MD. 1999. Evaluation of a MOSFET radiation sensor for the measurement of entrance surface dose in diagnostic radiology. *British Journal of Radiology, 72*(858), 562-568.

Pehl, RH, Cordi, RC, & Goulding, FS. 1972. High-purity germanium: Detector fabrication and performance. *Nuclear Science, IEEE Transactions on, 19*(1), 265-269.

Plechaty, E, Cullen, D, & Howerton, R. 1981. Tables and graphs of photon-interaction cross sections from 0.1 keV to 100 MeV derived from the LLL evaluated-nuclear-data-library (Lawrence Livermore Laboratory) Report No. UCRL-50400, Vol. 6, Rev. 3, 227-244.

Van de Putte, S, Verhaegen, F, Taeymans Y. 2000. Correlation of patient skin doses in cardiac interventional radiology with dosearea product. *British Journal of Radiology*,73:504-13.

Qi, ZY, Deng, XW, Huang, SM, Lu, J, Lerch, M, Cutajar, D, & Rosenfeld, A. 2007. Verification of the plan dosimetry for high dose rate brachytherapy using metal-oxide-semiconductor field effect transistor detectors. *Medical Physics, 34*(6), 2007-2013.

Qi, ZY, Deng, XW, Huang, SM, Shiu, A, Lerch, M, Metcalfe, P, Rosenfeld, A, & Kron, T. 2011. Real-time *in vivo* dosimetry with MOSFET detectors in serial tomotherapy for head and neck cancer patients. *International Journal of Radiation Oncology • Biology • Physics, 80*(5), 1581-1588.

Qi, ZY, Deng, XW, Huang, SM, Zhang, L, He, ZC, Li, XA, Kwan, I, Lerch, M, Cutajar, D, Metcalfe, P, & Rosenfeld, A. 2009. *In vivo* verification of superficial dose for head and neck treatments using intensity-modulated techniques. *Medical Physics, 36*(1), 59-70.

Ramani, R, Russell, S, & O'Brien, P. 1997. Clinical dosimetry using MOSFETs. *International Journal of Radiation Oncology • Biology • Physics, 37*(4), 959-964.

Ramaseshan, R, Kohli, KS, Zhang, TJ, Lam, T, Norlinger, B, Hallil, A, & Islam, M. 2004. Performance characteristics of a microMOSFET as an *in vivo* dosimeter in radiation therapy. *Physics in Medicine and Biology, 49*(17), 4031-4048.

Ravotti, F, Glaser, M, Rosenfeld, AB, Lerch, M, Holmes-Siedle, A, & Sarrabayrous, G. 2007. Radiation monitoring in mixed environments at CERN: From the IRRAD6 facility to the LHC experiments. *Nuclear Science, IEEE Transactions on, 54*(4), 1170-1177.

Ristić, GS. 2009. Thermal and UV annealing of irradiated pMOS dosimetric transistors. *Journal of Physics D: Applied Physics, 42*(13), 135101.

Rosenfeld, AB. 2002. MOSFET dosimetry on modern radiation oncology modalities. *Radiation Protection Dosimetry, 101*(1-4), 393-398.

Rosenfeld, AB. 2006. Electronic dosimetry in radiation therapy. *Radiation Measurements, 41*, 134-153.

Sandborg, M, Rossitti, S, & Pettersson, H. 2010. Local skin and eye lens equivalent doses in interventional neuroradiology. *European Radiology, 20*(3), 725-733.

Schueler, BA, Kallmes, DF, & Cloft, HJ. 2005. 3D cerebral angiography: radiation dose comparison with digital subtraction angiography. *American Journal of Neuroradiology, 26*(8), 1898-1901.

Shigematsu, I, Akiyama, M, Sasaki, H, Ito, C, & Kamada, N. 1991. *Effects of A-bomb radiation on the human body*. Hiroshima International Council for Medical Care of the Radiation-exposed. Tokyo, Japan.

Siddle, KJ, Sim, LH, & Case, CC. 1990. Radiation doses to the lens of the eye during computerised tomography of the orbit; a comparison of four modern computerised tomography units. *Australasian Radiology, 34*(4), 323-325.

Skardal, A, Mack, D, Kapetanovic, E, Atala, A, Jackson, JD, Yoo, J, & Soker, S. 2012. Bioprinted amniotic fluid-derived stem cells accelerate healing of large skin wounds. *Stem Cells Translational Medicine, 1*(11), 792-802.

Snyder, W, Cook, M, Nasset, E, Karhausen, L, Howells, GP, & Tipton, I. 1974. Report of the task group on reference man. *ICRP publicaiton: 23*.

Somervaille, LJ, Chettle, DR, Scott, MC, Tennant, DR, McKiernan, MJ, Skilbeck, A, & Trethowan, WN. 1988. In vivo tibia lead measurements as an index of cumulative exposure in occupationally exposed subjects. *British Journal of Industrial Medicine, 45*(3), 174-181.

Soubra, M, Cygler, J, & Mackay, G. 1994. Evaluation of a dual bias dual metal oxide-silicon semiconductor field effect transistor detector as radiation dosimeter. *Medical Physics, 21*(4), 567-572.

Spiker, A, Zinn, Z, Carter, WH, Powers, R, & Kovach, R. 2012. Fluoroscopy-induced chronic radiation dermatitis. *American Journal of Cardiology, 110*(12), 1861-1863.

Stecker, MS, Balter, S, Towbin, RB, Miller, DL, Vañó, E, Bartal, G, Angle, JF, Chao, CP, Cohen, AM, & Dixon, RG. 2009. Guidelines for patient radiation dose management. Journal of Vascular and Interventional Radiology*, 20*(7), 263-273.

Stewart, FA, Akleyev, AV, Hauer-Jensen, M, Hendry, JH, Kleiman, NJ, Macvittie, TJ, Aleman, BM, Edgar, AB, Mabuchi, K, Muirhead, CR, Shore, RE, & Wallace, WH. 2012. ICRP publication 118: ICRP statement on tissue reactions and early and late effects of radiation in normal tissues and organs--threshold doses for tissue reactions in a radiation protection context. *Ann ICRP, 41*(1-2), 1-322.

Surowiec, A, Shrivastava, PN, Astrahan, M, & Petrovich, Z. 1992. Utilization of a multilayer polyacrylamide phantom for evaluation of hyperthermia applicators. *International Journal of Hyperthermia, 8*(6), 795-807.

Tasman, W, Jaeger, EA. 2001. *The Wills Eye Hospital atlas of clinical ophthalmology*. Lippincott Williams & Wilkins. Baltimore, United States.

Tam, MD, Laycock, SD, Bell, D, & Chojnowski, A. 2012. 3-D printout of a DICOM file to aid surgical planning in a 6 year old patient with a large scapular osteochondroma complicating congenital diaphyseal aclasia. *Journal of Radiology Case Reports, 6*(1), 31-37.

Theodorakou, C, & Horrocks, JA. 2003. A study on radiation doses and irradiated areas in cerebral embolisation. *Bitish Journal of Radiology, 76*(908), 546-552.

Todd, A. 2000. Contamination of in vivo bone-lead measurements. *Physics in medicine and biology, 45*(1), 229.

Tsai, H-Y, Lin, Y-C, & Tyan, Y-S. 2014. Patient-specific organ dose estimation during transcatheter arterial embolization using Monte Carlo method and adaptive organ segmentation. *Radiation Physics and Chemistry, 104*, 376-380.

Uhlhorn, SR, Borja, D, Manns, F, & Parel, JM. 2008. Refractive index measurement of the isolated crystalline lens using optical coherence tomography. *Vision Research, 48*(27), 2732-2738.

United Nations Scientific Committee On The Effects Of Atomic Radiation. 2010. UNSCEAR 2008 report to the General Assembly. *New York: United Nations*.

Valentin, J. 2000. Avoidance of radiation injuries from medical interventional procedures. *Ann ICRP, 30*(2), 7-67.

Valentin, J. 2002. Basic anatomical and physiological data for use in radiological protection: reference values: ICRP Publication 89. *Ann ICRP, 32*(3), 1-277.

Valentin, J. 2007. *The 2007 recommendations of the international commission on radiological protection*. Elsevier Oxford.

Vano, E, Fernandez, JM, Sanchez, RM, Martinez, D, Ibor, LL, Gil, A, & Serna-Candel, C. 2013. Patient radiation dose management in the follow-up of potential skin injuries in neuroradiology. *American Journal of Neuroradiology, 34*(2), 277-282.

Vano, E, Goicolea, J, Galvan, C, Gonzalez, L, Meiggs, L, Ten, JI, & Macaya, C. 2001a. Skin radiation injuries in patients following repeated coronary angioplasty procedures. *British Journal of Radiology, 74*(887), 1023-1031.

Vano, E, Gonzalez, L, Ten, JI, Fernandez, JM, Guibelalde, E, & Macaya, C. 2001b. Skin dose and dose-area product values for interventional cardiology procedures. *British Journal of Radiology, 74*(877), 48-55.

Vano, E, Kleiman, NJ, Duran, A, Rehani, MM, Echeverri, D, & Cabrera, M. 2010. Radiation cataract risk in interventional cardiology personnel. *Radiation Research, 174*(4), 490-495.

Vano, E, Prieto, C, Fernandez, JM, Gonzalez, L, Sabate, M, & Galvan, C. 2003. Skin dose and dose-area product values in patients undergoing intracoronary brachytherapy. *British Journal of Radiology, 76*(901), 32-38.

Veigele, WJ. 1973. Photon cross sections from 0.1 keV to 1 MeV for elements Z= 1 to Z= 94. *Atomic Data and Nuclear Data Tables, 5*(1), 51-111.

Wagner, LK. 1998. Minimizing Risks from Fluoroscopic X Rays: Bioeffects, Instrumentation, and Examination. *Partners in Radiation Management*.

Wagner, LK, Eifel, PJ, & Geise, RA. 1994. Potential biological effects following high X-ray dose interventional procedures. *Journal of Vascular and Interventional Radiology, 5*(1), 71-84.

Wagner, LK, McNeese, MD, Marx, MV, & Siegel, EL. 1999. Severe skin reactions from interventional fluoroscopy: case report and review of the literature. *Radiology, 213*(3), 773-776.

Waran, V, Devaraj, P, Hari Chandran, T, Muthusamy, KA, Rathinam, AK, Balakrishnan, YK, Tung, TS, Raman, R, & Rahman, ZA. 2012. Three-dimensional anatomical accuracy of cranial models created by rapid prototyping techniques validated using a neuronavigation station. *Journal of Clinical Neuroscience, 19*(4), 574-577.

White, D. 1978. The photon attenuation and absorption properties of clear and white polystyrene. *British journal of radiology, 51*(605), 397-398.

White, D. 1993. The design and manufacture of anthropomorphic phantoms. *Radiation Protection Dosimetry, 49*(1-3), 359-369.

White, DR, Martin, RJ, & Darlison, R. 1977. Epoxy resin based tissue substitutes. *The British journal of radiology, 50*(599), 814-821. doi: 10.1259/0007-1285-50-599-814

Winslow, JF, Hyer, DE, Fisher, RF, Tien, CJ, & Hintenlang, DE. 2009. Construction of anthropomorphic phantoms for use in dosimetry studies. *Journal of Applied Clinical Medical Physics, 10*(3), 2986.

Worgul, BV, Kundiyev, YI, Sergiyenko, NM, Chumak, VV, Vitte, PM, Medvedovsky, C, Bakhanova, EV, Junk, AK, Kyrychenko, OY, Musijachenko, NV, Shylo, SA, Vitte, OP, Xu, S, Xue, X, & Shore, RE. 2007. Cataracts among Chernobyl clean-up workers: implications regarding permissible eye exposures. *Radiation Research, 167*(2), 233-243.

World Health Organization and Institut fur Strahlenhygiene des Bundesgesundheitsamtes. 2000. Efficacy and radiation safety in interventional radiology. *World Health Organization*.

Yoshizumi, TT, Goodman, PC, Frush, DP, Nguyen, G, Toncheva, G, Sarder, M, & Barnes, L. 2007. Validation of metal oxide semiconductor field effect transistor technology for organ dose assessment during CT: comparison with thermoluminescent dosimetry. *American Journal of Roentgenology, 188*(5), 1332-1336.

Yuan, H, Zhou, Q, Li, B, Bao, M, Lou, X, & Zhang, Y. 2015. Direct printing of patterned three-dimensional ultrafine fibrous scaffolds by stable jet electrospinning for cellular ingrowth. *Biofabrication, 7*(4), 045004.

Zhang, Y, Xia, L, Zhai, D, Shi, M, Luo, Y, Feng, C, Fang, B, Yin, J, Chang, J, & Wu, C. 2015. Mesoporous bioactive glass nanolayer-functionalized 3D-printed scaffolds for accelerating osteogenesis and angiogenesis. *Nanoscale*.

List of Publications and Papers Presented

Journal Papers:

M.J. Safari, J.H.D. Wong, K.H. Ng, W.L. Jong, D.L. Cutajar & A.B. Rosenfeld. Characterization of MO*Skin* detector for *in-vivo* skin dose measurement during interventional radiology procedures. Medical Physics. 2015. DOI: 10.1118/1.4918576.

M.J. Safari, J.H.D. Wong, K.H. Ng, K.A. Abd Kadir, N. Thorpe, D.L. Cutajar, M. Petasecca, M. Lerch & A.B. Rosenfeld. Real-time patient dose monitoring using MO*Skin* detector for cerebral angiography procedures. European Radiology. 2015. DOI: 10.1007/s00330-015-3818-9.

M.J. Safari, J.H.D. Wong, K.A.A. Kadir, F. A. Sani & K.H. Ng. A method to reduce patient's eye lens dose in neuro-interventional radiology procedures. Radiation Physics and Chemistry. 2016. DOI: 10.1016/j.radphyschem.2016.03.013.

M.J. Safari, W.L. Jong, J.H.D. Wong, K.H. Ng & A.B. Rosenfeld. Investigation of the contribution of commonly used radiological exposure parameters to patient's dose during neuro-interventional radiology procedures: A Phantom Study. (Under review, Physica Medica).

Conferences

Oral presentations

MJ Safari, JHD Wong, KA A Kadir, KH Ng. Assessment of patient's eye lens dose using a custom made anthropomorphic head phantom. 13th South East Asia Congress of Medical Physics (SEACOMP). Yogyakarta, Indonesia, Dec 10-12, 2015.

MJ Safari, WL Jong, JHD Wong, AB Rosenfeld, KH Ng. Investigation of the Radiation Dose Delivery to the Skin and Eye Lens of a Phantom during Interventional Cerebral Angiography Procedures. Micro, Mini and Nano Dosimetry &. International Prostate Cancer Treatment (MMND-IPCT), Port Douglas, Queensland, Australia, Oct 20-25, 2014.

MJ Safari, JHD Wong, KH Ng, D Cutajar, AB Rosenfeld. Characterization of MO*Skin* Detector in Diagnostic Energy Range. 13th Asia-Oceania Congress of Medical Physics (AOCMP) and 11th South-East Asian Congress of Medical Physics (SEACOMP). Singapore, Dec 12-14, 2013.

MJ Safari, JHD Wong, KAA Kadir, KH Ng, DL Cutajar, AB Rosenfeld. A real time dose monitoring system for eye lens during cerebral angiography procedure. 13th Asia-Oceania Congress of Medical Physics (AOCMP) and 11th South-East Asian Congress of Medical Physics (SEACOMP). Singapore, Dec 12-14, 2013.

Poster presentations

MJ Safari, JHD Wong, KA Abd Kadir and KH Ng. A method to reduce the patient's eye lens dose during cerebral angiography procedures. International Union for Physical and Engineering Sciences in Medicine (IUPESM), World Congress on Medical Physics and Biomedical Imaging, Toronto, Canada, Jun 7–12, 2015.

MJ Safari, JHD Wong, KA Abd Kadir and KH Ng. Assessing Patients' Skin and Eye Lens Radiation Doses During Interventional Neuroradiology Procedures using Gafchromic® XR-RV3 Film. 14th Asia-Oceania Congress of Medical Physics (AOCMP) & 12th South East Asia Congress of Medical Physics (SEACOMP), Ho Chi Monh City, Vietnam, Oct 23-25, 2014.

MJ Safari, WL Jong, JHD Wong, KAA Kadir, KH Ng, AB Rosenfeld. Evaluation of eye lens dose during neuro-interventional procedure. 20th International Conference on Medical Physics and Biomedical Engineering (ICMP). Brighton, UK, Sept 1-4, 2013.